# Integration of magnetic resonance spectroscopic imaging into the radiotherapy treatment planning

Andrea Laruelo


# THÈSE

**En vue de l'obtention du**

## DOCTORAT DE L'UNIVERSITÉ DE TOULOUSE

**Délivré par :**

Université Toulouse 3 Paul Sabatier (UT3 Paul Sabatier)

---

**Présentée et soutenue par :**
**Andrea LARUELO FERNÁNDEZ**

le 24 mai 2016

**Titre :**

INTEGRATION OF MAGNETIC RESONANCE SPECTROSCOPIC IMAGING INTO THE RADIOTHERAPY TREATMENT PLANNING

---

**École doctorale et discipline ou spécialité :**
ED GEET : Radio-physique et Imagerie Médicale

**Unité de recherche :**
Laboratoire Imagerie Cérébrale et Handicaps Neurologiques (ICHN), INSERM UMRS 825
Institut de Recherche en Informatique de Toulouse (IRIT) - ENSEEIHT (UMR 5505)

**Directeur/trice(s) de Thèse :**

**Dr. Anne LAPRIE** et **Dr. Lotfi CHAARI**

**Jury :**

| | | |
|---|---|---|
| **M. Philippe CIUCIU** | Directeur de Recherche | Rapporteur |
| **Mme. Margarida JULIÀ-SAPÉ** | Maître de Coonférences | Rapporteur |
| **M. Jean-Yves TOURNERET** | Professeur | Examinateur |
| **M. Frédéric PASCAL** | Professeur | Examinateur |
| **Mme. Anne LAPRIE** | Maître de Coonférences | Co-directrice de thèse |
| **M. Lotfi CHAARI** | Maître de Coonférences | Co-directeur de thèse |
| **M. Aleksandar DOGANDZIC** | Maître de Coonférences | Invité |
| **M. Franck DESMOULIN** | Chargé de Recherche | Invité |

# Abstract

Magnetic resonance spectroscopic imaging (MRSI) is a non-invasive technique able to provide the spatial distribution of relevant biochemical compounds (metabolites) commonly used as biomarkers of disease. Information provided by MRSI can be used as a valuable insight for the diagnosis, treatment and follow-up of several diseases such as cancer or neurological disorders. Obtaining accurate and reliable information from in vivo MRSI signals is a crucial requirement for the clinical utility of this technique. Despite the numerous publications on the topic, the interpretation of MRSI data is still a challenging problem due to different factors such as the low signal-to-noise ratio (SNR) of the signals, the overlap of spectral lines or the presence of nuisance components. In this thesis, we propose novel signal processing algorithms with the aim to alleviate these limitations. Our main goals are the development of processing methods to improve the analysis of MRSI data, and to exploit the potential of MRSI for the development of novel treatment strategies in radiotherapy (RT). To address the SNR limitations of MRSI, we first investigate a new algorithm for denoising MRSI data based on a hybrid spatio-spectral regularization scheme in the wavelet domain. We then integrate this regularization scheme into two different novel methods to interpret MRSI data. More specifically, a quantification and a tissue pattern recognition algorithms are presented as complementary approaches for the interpretation of MRSI data. The proposed methods rely on fast parallel optimization algorithms dealing with convex but non-necessarily differentiable criteria involving, for example, suitable sparsity promoting priors. All the methods are evaluated and compared with other existing techniques using simulated and in vivo data. Results show the ability of these methods to deal with the artifacts usually present in in vivo data, especially in the context of lesions. In addition, in order to show the potential of MRSI to optimize the RT treatment planning, a supervised classification method for the identification of regions at risk of relapse in brain tumor patients is proposed and validated on real data.

# Acknowledgements

This work is part of the SUMMER Marie Curie Research Training Network (PITN-GA-2011- 290148), which is funded by the 7th Framework Programme of the European Commission (FP7-PEOPLE-2011-ITN). The information and views set out in this publication are those of the authors and do not necessarily reflect the official opinion of the European Union. Neither the European Union institutions and bodies nor any person acting on their behalf may be held responsible for the use which may be made of the information contained therein.
Part of this work was supported by the ANR-11-LABX-0040-CIMI in particular during the program ANR-11-IDEX-0002-02 within the thematic trimester on image processing.

# Contents

# Nomenclature

**AMARES** Advanced Method for Accurate Robust and Efficient Spectral fitting

**AQSES** Automated Quantitation of Short Echo time MRS Spectra

**BSS** Blind Source Separation

**CHESS** CHEmical Shift Selective water suppression

**Cho** Choline

**CNI** Choline-N-acetylaspartate index

**CNR2** Choline over N-acetylaspartate ratio higher than 2

**Cr** Creatine

**CRLB** Cramér-Rao Lower Bound

**CSI** Chemical Shift Imaging

**dB** decibel

**FID** Free Induction Decay

**FLAIR** Fluid Attenuated Inversion Recovery

**FOV** Field Of View

**GBM** Glioblastoma multiforme

**Gd** Gadolinium

**GTV** Gross Tumor Volume

**Gy** Gray

**HSVD** Hankel Singular Value Decomposition

**Hz** Hertz

**jMRUI** Java-based graphical user interface for processing MRS

| | |
|---|---|
| **Lac** | Lactate |
| **LCModel** | Linear Combination of Model spectra |
| **Lip** | Lipids |
| **MR** | Magnetic Resonance |
| **MRS** | Magnetic Resonance Spectroscopy |
| **MRSI** | Magnetic Resonance Spectroscopic Imaging |
| **NAA** | N-acetylaspartate |
| **PPM** | Parts Per Million |
| **PRESS** | Point RESolved Spectroscopy |
| **QUEST** | quantitation based on semi-parametric QUantum ESTimation |
| **RMSE** | Root Mean Square Error |
| **ROC** | Receiver Operating Characteristic |
| **SNR** | Signal-to-Noise Ratio |
| **SSIM** | Structural SIMilarity index |
| **STEAM** | STimulated Echo Acquisition Mode |
| **SVM** | Support Vectors Machine |
| **SVS** | Single Voxel Spectroscopy |
| **T** | Tesla |
| **TE** | Echo Time |
| **TR** | Repetition Time |
| **TV** | Total Variation |
| **VOI** | Volume of interest |

# List of Figures

# List of Tables

# Chapter 1

# Introduction

## Contents



## 1.1 Motivation

Magnetic resonance spectroscopic imaging (MRSI) has demonstrated the ability to localise and characterize tumour tissues and to detect abnormal tissue beyond that seen on standard MRI. However, robust data analysis methods are still needed. The aim of this thesis is to propose new algorithms to overcome the current limitations and to address the open challenges in the processing of MRSI data. MRSI is a non-invasive modality able to provide the spatial distribution of relevant biochemical compounds (metabolites) commonly used as biomarkers of disease. Information provided by MRSI can be used as a valuable insight for the diagnosis, treatment and follow-up of several diseases such as cancer or neurological disorders. Obtaining accurate and reliable information from in vivo MRSI signals is a crucial requirement for the clinical utility of this technique. Despite the numerous publications on the topic, the interpretation of MRSI data is still a challenging problem due to different factors such as the low signal-to-noise ratio (SNR) of the signals, the overlap of spectral lines or the presence of nuisance components. Most advanced methods to process MRSI data incorporate spectral knowledge together with spatial smoothness assumptions on some spectral parameters. This thesis addresses the problem of interpreting MRSI data and characterizing tumor recurrence in brain tumor patients. Specifically, four research questions are formulated in this thesis:

- Extracting meaningful signals from noisy measured data
- Quantifying spatially coherent metabolites
- Decomposing MRSI signals in tissue-specific spectral patterns
- Identifying tumor relapse areas using multi-parametric MR data.

These objectives are addressed through a methodological approach based on novel processing methods that incorporate prior knowledge on the MRSI data using spatio-spectral regularization. As an application, the thesis addresses the integration of MRSI into the radiotherapy treatment workflow within the context of the European project SUMMER (Software for the Use of Multi-Modality images in External Radiotherapy) founded by the European Commission (FP7–PEOPLE–ITN framework).
Four main contributions are presented in this work:

- Spatio-spectral regularization to solve the ill-posed inverse problem of MRSI denoising.
- Joint denoising-quantification of MRSI data based on a spatio-spectral regularization and metabolite profiles.
- Spectral unmixing of MRSI spectra for brain tissue classification and visualization of tumor spread (not visible from anatomical MRI modalities).
- Classification of multi-parametric MR data using a supervised method, and experimental correlation with clinical results for the identification of areas with high probability of relapse.

## 1.2 Organization of the manuscript

The thesis is organized as follows:

**- Chapter 2: Magnetic resonance spectroscopic imaging**
This chapter describes the important role of imaging in the evaluation of cancer patients, focusing on brain tumor patients. While morphological imaging is the most commonly used technique, the introduction of new functional

imaging modalities has improved the characterization of tumors. One of such techniques is MRSI. This chapter summarizes the principles and basics of this technique and its role into the radiotherapy context.

**- Chapter 3: MRSI processing**
This chapter summarizes the main conventional techniques to process and interpret MRSI data. The concept of inverse problem is introduced, and it is then exploited to express the processing methods proposed in this thesis. Since the considered inverse problems are ill-posed, the technique of regularization is also introduced. The regularization schemes proposed in this thesis are based on objective functions that are convex but not necessarily differentiable involving, for example, suitable sparsity promoting priors. This makes impossible the use of standard gradient-based algorithms for optimization. We therefore propose to perform the optimization by using the concept of proximity operators which has been successfully used in a number of previous works in convex optimization.

**- Chapter 4: MRSI Denoising**
In vivo MRSI suffers from poor signal-to-noise ratio (SNR) limiting its clinical use for treatment purposes. This is due to the combination of a weak magnetic resonance signal and low metabolite concentrations, in addition to the acquisition noise. We propose a new method that handles this challenge by efficiently denoising MRSI signals without constraining the spectral or spatial profiles. The proposed denoising approach is based on wavelet transforms and exploits the sparsity of the MRSI signals both in the spatial and frequency domains. A fast proximal optimization algorithm is then used to recover the optimal solution. Experiments on synthetic and real MRSI data show that the proposed denoising method provides better noise suppression (SNR increase up to 60%). In addition, this method is computationally efficient and preserves data features better than other existing strategies.

**- Chapter 5: MRSI Quantification**
Obtaining accurate metabolite concentrations from in vivo MRSI signals is a crucial requirement for clinical applications. Despite the numerous publications on the topic, accurate quantification is still a challenging problem due to the low signal-to-noise ratio, the overlap of spectral lines and the presence of nuisance components. We propose a novel quantification method which alleviates these limitations by exploiting a spatial-spectral regulariza-

tion scheme. Spatial and spectral regularization terms are jointly incorporated into the quantification model with the aim of increasing the SNR of the data and exploiting the neighboring information along the spatial and spectral dimensions. Contrary to previous methods, the proposed technique is not restricted to spatially smooth solutions and the regularization terms are not expressed directly on the sought parameters, but on appropriate transformed domains. In order to simultaneously quantify all signals in the MRSI grid by using an appropriate prior information, a fast proximal optimization algorithm is proposed. Experiments on synthetic MRSI data demonstrate that the error in the estimated metabolite concentrations is reduced by a mean of 41% with the proposed scheme. Results on in vivo brain MRSI data show the benefit of the proposed approach which is able to correctly fit overlapping peaks and to capture metabolites that are missed by single voxel methods due to their low concentrations.

**- Chapter 6: MRSI Classification**
Despite post-operative radiotherapy (RT) of glioblastoma (GBM), local tumor regrowth occur in irradiated areas and are responsible for poor outcome. Identification of sites with high probability of recurrence is a promising way to define new target volumes for dose escalation in RT treatments. We show that a supervised learning system based on support vector machines can be trained to generate probability maps of relapse for brain tumor patients. The quantification method proposed in Chapter 4 is used as a feature extraction technique. The estimated metabolite amplitudes in combination with different modalities of anatomical MRI images are used as input features in the classifier. This study outlines the ability of MRSI data, in combination with other MRI modalities, to define new biologically tailored target volumes for dose escalation in radiotherapy treatments.

**- Chapter 7: MRSI Unmixing**
This chapter presents a spectral unmixing algorithm as an alternative approach to interpret MRSI data. Spectral unmixing consists of extracting from a hyperspectral data set (MRSI data set in our case), the spectral patterns of the pure components (tissue types) present in the image and of identifying their abundances. To this aim, we propose a blind source separation (BSS) algorithm for brain tissue classification and visualization of tumor spread using MRSI data. The proposed BSS method jointly incorporates prior knowledge about the spatial and spectral dimensions of MRSI

data. It aims at increasing the signal-to-noise ratio of the data and to favor solutions with few irregularities in the spatial and the spectral dimensions. Contrary to previous methods, it is able to extract more than two physically meaningful tissue patterns and it is not restricted to non-negative sources. In addition, the results do not depend on the initialization strategy since this algorithm relies on the optimization of convex functions. Different experiments with in-vivo MRSI data show that the method is robust to noise and to the presence of low quality spectra.

**- Chapter 8: Conclusions and perspectives**
New algorithms combining spatial and spectral regularizations in the wavelet domain to improve MRSI data processing have been presented. Contrary to previous approaches, the suggested methods combine two regularization terms to favour solutions with specific properties in both the spatial and the spectral dimensions. Experiments on synthetic and in-vivo data show the benefit of using this type of regularization in different applications: preprocessing (denoising), quantification and spectral unmixing. The dependency on only two hyperparameters and the use of fast proximal algorithms that allow parallel computations facilitate the automation of the presented methods, which is crucial for the acceptance of the MRSI technique into the clinical routine.

## 1.3 Publications

### Journal papers

- **Laruelo A**, Chaari L, Tourneret JY, Batatia H, Ken S, Rowland B, Ferrand R and Laprie A, "Spatio-spectral regularization to improve MRSI quantification", NMR in Biomedicine, 2016. In Press.

### International conference papers

- **Laruelo A**, Chaari L, Batatia H, Ken S, Rowland B, Laprie A and Tourneret JY, "Hybrid sparse regularization for magnetic resonance spectroscopy", Annual International Conference of the IEEE Engineering in Medicine and Biology Society (EMBC'13), Osaka, Japan, pp.

6768–6771, July 2013.

- Nunes M, **Laruelo A**, Ken S, Laprie A, Bühler K, "A survey on visualizing magnetic resonance spectroscopy data", Eurographics Workshop on Visual Computing for Biology and Medicine (EGVCMB'14), Vienna, Austria, September 2014.

- **Laruelo A**, Chaari L, Ken S, Tourneret JY, Batatia H and Laprie A, "MRSI data unmixing using spatial and spectral priors in transformed domains", IEEE International Symposium on Biomedical Imaging (ISBI), Prague, Czech Republic, April 2016.

- Nunes M, **Laruelo A**, Schlachter M, Ken S, Matkovic K, Laprie A, Bühler K, "Analysis and Visualization of Longitudinal MR Spectroscopy Data", IEEE Conference on Visual Analytics Science and Technology (VAST), 2016 (submitted).

## International conference abstracts

- **Laruelo A**, Chaari L, Rowland B, Ken S, Batatia H, Ferrand R, Tourneret JY, Laprie A, "MRSI data denoising to improve metabolite quantification", Annual Scientific Meeting of the European Society for Magnetic Resonance in Medicine and Biology (ESMRMB'13), Toulouse, France, October 2013.

- **Laruelo A**, Chaari L, Ken S, Rowland B, Batatia H, Ferrand R, Simon L, Tourneret J, Laprie A, "Towards accurate and robust MRSI quantification to improve the radiotherapy treatment of GBM", Annual Meeting of the American Society for Radiation Oncology (ASTRO), September 2014.

- Rowland B, **Laruelo A**, Lin AP and Ken S, "MRS Choline/NAA enhancement is a predictor of post-RT disease-free survival time in glioblastoma multiforme", European Society for Therapeutic Radiology and Oncology Congress (ESTRO), Barcelona, Spain, 2015.

- **Laruelo A**, Chaari L, Tourneret JY, Batatia H, Ken S, Rowland B, Ferrand R and Laprie A, "Segmentation of radiotherapy target volumes based on magnetic resonance spectroscopic imaging", 3rd International MR in RT Symposium (MRinRT), 2015.

- **Laruelo A**, Dolz J, Ken S, Chaari L, Vermandel M, Massoptier L and Laprie A, "Probability map prediction of relapse areas in glioblastoma patients using multi-parametric MR", European Society for Therapeutic Radiology and Oncology Congress (ESTRO), Turin, Italy 2016. Nominated for the ESTRO Best Poster Award.

### Book chapters

- **Laruelo A**, Chaari L, Batatia H, Rowland B, Ken S, Ferrand R, Tourneret JY, Laprie A, "Magnetic resonance spectroscopic data processing", *Innovative imaging to improve radiotherapy treatments*, Lulu Enterprises Inc Ed (ISBN: 978-1-291-60417-7), 1:91-96, 2013.

- Rowland B, **Laruelo A**, Ken S, Ferrand R, Laprie A, "Water suppression in post-processing of MRSI signals", *Innovative imaging to improve radiotherapy treatments*, Lulu Enterprises Inc Ed (ISBN: 978-1-291-60417-7), 1:63-70, 2013.

- **Laruelo A**, Chaari L, Batatia H, Rowland B, Ken S, Ferrand R, Tourneret JY, Laprie A, "Exploiting MRSI data properties to improve quantification". *Multimodal imaging towards individualized radiotherapy treatments*, Editors: Massoptier and Song, pp. 63-68, 2014.

## 1.4 SUMMER Project

This PhD has be developed under the SUMMER project (Software for the Use of Multi-Modality images in External Radiotherapy, PITN-GA-2011-290148, a Initial Training Network (ITN) granted by Marie Curie Actions in the 7th Framework Program (FP7–PEOPLE–ITN framework), http://summer-project.eu/). The corner stone objective of this project is to develop a unique tool that radiation oncologists, physicians, physicists and radiologists can share to analyze images in the radiotherapy work-flow. "SUMMER" aims to improve the precision of clinical target volume by the definition of a biological target volume, leading to define optimal radiotherapy planning and to follow patient treatment response in order to perform on-line treatment changes. The partners' expertise ranged from oncology to computer engineering, including ergonomics, signal processing and informatics, together in

a consortium composed by five academic partners and two industrial partners. As a fellow of this project, my work was focused on the development of processing techniques for MRSI data to facilitate the integration of this technique into the radiotherapy work-flow.

## Software

This PhD work has led to the design of an MRSI processing plugin integrated within the SUMMER project prototype. Note that this software is not freely available online for confidentiality reasons.

# Chapter 2

# Magnetic resonance spectroscopic imaging

## Contents



## 2.1 Introduction

Imaging in oncology has been traditionally based on morphological criteria. Magnetic resonance imaging (MRI) is widely used for the diagnosis and follow-up of brain tumors due to its high soft-tissue contrast. Advanced functional MRI techniques can characterize physiological changes in tissues before they become visible in conventional morphological images [Laprie et al., 2008; Deviers et al., 2014]. The early assessment of biochemical and functional properties of lesions can be used to guide and personalize oncological treatments. The goal of this chapter is to provide an overview of MRI techniques typically used in oncology. The development of new therapeutic strategies based on advanced functional imaging techniques is discussed. More specifically, the integration magnetic resonance spectroscopy imaging (MRSI) into the radiotherapy (RT) treatment planning is motivated.

## 2.2 Imaging in oncology

### 2.2.1 Conventional morphological imaging

Non-invasive imaging plays a crucial role in cancer diagnosis and management. Anatomical features are routinely assessed through morphological imaging techniques. For example, tumour response to treatment is typically assessed from measurements of tumour size, using techniques such as X-ray computed tomography (CT) and MRI [Organization, 1979; Therasse et al., 2000; Eisenhauer et al., 2009]. However, morphological assessment is not suitable for diffuse and/or multiple tumor lesions and changes in tumor size do not always accurately reflect response to treatment [Wahl et al., 2009]. Indeed the limitations of morphological assessment are well documented, and it has already been shown that changes in metabolism and perfusion occur before morphological changes [Evelhoch, 1999; Tofts et al., 1999; Carmeliet and Jain, 2000]. Conventional anatomical imaging often allows only vague identification and localization of tumors, and biopsies are routinely required to appropriately diagnose and treat tumors. Unfortunately, the location of many brain tumors prevents biopsies from being performed, and detailed knowledge of the nature of the tumor is missing in these cases.
Significant effort is put into the development and validation of new non-invasive imaging techniques able to provide information about metabolic processes as well as cellular and molecular interactions [Schober and Riemann, 2013]. Early and reliable assessment of functional properties of lesions has become a necessity to correctly diagnose, differentiate, and guide therapy. MRI has introduced many tools to improve morphological evaluation and added capabilities for functional characterization of lesions. Implementing different imaging sequences, MRI allows a considerable tissue characterization regarding its proton/water or fatty tissue content. In addition, no health risks are known to be caused by the main magnetic field of clinical MR systems. Whereas continuous improvements in image quality have been achieved in MRI in the recent years, the major advance for oncologic applications is the clinical implementation of functional assessment techniques that provide additional information on top of morphology.

### 2.2.2 Functional MRI techniques

Currently, MRI is well established in the clinical practice, even if it is in continuous development [Hernando et al., 2010]. For more than 30 years this method has presented significant progress in different fields of medicine, particularly in cancer patients, including different steps of oncologic management, such as detection, characterization, staging, response evaluation and post-therapeutic follow-up [Higgins and Pomper, 2011]. MRI has become a powerful clinical tool for evaluation of brain anatomy able to provide morphological information, such as size, contours, number of lesions and relationship with adjacent structures [Hernando et al., 2010]. However, functional and metabolic alterations which normally precede morphological alterations are not usually recognized by traditional imaging techniques. Advanced MRI techniques provide physiologic, metabolic and functional information about tumor biology beyond standard MRI and CT evaluations [Higgins and Pomper, 2011; Histed et al., 2012]. The development of new MRI techniques has enabled the functional assessment of the structures in order to obtain information on the different physiological processes of the tumor micro-environment, such as oxygenation levels, cellularity and vascularity. Functional MRI includes perfusion MRI, diffusion imaging, brain functional MRI (fMRI) and magnetic resonance spectroscopy (MRS(I)). These functional MRI modalities can provide unique pathological, physiological and metabolic information that are not available in anatomic MR. MR perfusion characterizes brain tumor biology through the underlaying pathological and physiological changes that occur with tumor vasculature [Maeda et al., 1993; Aronen et al., 1994; Gillard et al., 2009]. MR diffusion exploits the translational mobility of water molecules to provide information on cellular density and the nature of local edema [Tien et al., 1994; Krabbe et al., 1997]. Functional MRI (fMRI) is based on the changes in blood oxygenation and flow that occur in response to neural activity [Ogawa et al., 1990; Logothetis et al., 2001]. It is commonly performed using the Blood Oxygenation Level Dependent signal (BOLD). The BOLD effect is based on the fact that when neuronal activity is increased in one part of the brain, there is also an increased amount of cerebral blood flow to that area. The ability to accurately model the evoked hemodynamic response to a neural event also plays an important role in the analysis of fMRI data. Therefore, there is a significant interest for estimating the hemodynamic response function (HRF) [Ciuciu et al., 2003; Vincent et al., 2010] in order to better understand the mecha-

nisms of cerebral activations. fMRI can be used to produce activation maps showing which parts of the brain are involved in a particular mental process or tasks. In addition, in recent years, there has been an increasing interest in the application of the technique at rest, termed resting-state fMRI, in order to investigate the functional architecture of the brain [Lee et al., 2013].
In this thesis we will focus on MRS (more specifically MRS imaging (MRSI)) which provides the metabolism characterization of the sampled tissue. The next sections describe the principles and basics of this technique, and introduce its role into the radiotherapy context.
The great flexibility of MRI systems allow the combined analysis of anatomical and functional findings allows a more comprehensive evaluation of the extension and activity of the lesions, including the phases of diagnosis, staging, response evaluation and follow-up. This opens the possibility of developing more individualized therapeutic strategies, with a favorable impact on the quality of life and survival of the patients [Higgins and Pomper, 2011; Padhani, 2011; Histed et al., 2012; Guimaraes et al., 2014]. In addition, unlike other imaging modalities like Positron Emission Tomography (PET) or CT, MR techniques do not involve exposure to ionizing radiation.

### 2.2.3 Quantitative MRI

Recently, there has been an increased interest in developing pulse sequences which allow the estimation of quantitative MR parameters. In contrast to conventional MRI, quantitative MRI (qMRI) is aimed at the direct measurement of the physical tissue properties, such as the relaxation times, T1 and T2, as well as the proton density (PD). Quantitative MRI offers several advantages including higher sensitivity, better accuracy and higher reproducibility since these properties are, in theory, independent of acquisition method. Whereas in conventional weighted MRI images the signal intensity is in arbitrary units and cannot be compared across sites or even scanning sessions, quantitative imaging can provide biomarkers that are absolute measures comparable across imaging sites and time points. However, qMRI is not commonly used in the routine clinical practice due to the significant longer acquisition times that are needed to obtain quantitative parameter maps. Parameter mapping requires multiple MRI images acquired with different timings usually resulting in long acquisition times. As an alternative to the acquisition of multiple images with varying parameters, model-based approaches have also been proposed for both T1 and T2 mapping [Block

et al., 2009; Velikina et al., 2010; Huang et al., 2012]. More recently, new approaches allowing the simultaneous quantification of multiple physiological parameters of interest in a reasonable scanning time have been proposed [Ma et al., 2013; De Rochefort, 2010].

## 2.3 Magnetic resonance spectroscopic imaging

Whereas conventional MRI determines the spatial distribution of water (and lipid) protons across a region of interest, MR spectroscopy measures the chemical content of MR-visible nuclei which include the metabolically relevant elements of proton ($^{1}$H) , carbon ($^{13}$C), and phosphorus ($^{31}$P). In clinical MRS, proton MRS, referred to as $^{1}$H MRS, is the most commonly used due to its high natural abundance (hydrogen is the most abundant atom in the body, representing about 63% of the total atoms), and high sensitivity over the other nuclei (proton has the highest gyromagnetic ratio of non-radioactive nuclei). Sensitivity is also enhanced compared to other nuclei due to favorable metabolite relaxation times, and also because several important (brain) metabolites have resonances resulting from functional groups with multiple protons. In addition, proton MRS relies on the same physical phenomenon as MRI, the nuclear magnetic resonance. Proton MRS data can therefore be acquired using the same scanner as conventional MRI. Nowadays most clinical MRI scanners (1.5-3 Tesla) have routine sequences for $^{1}$H-MRS measurements, providing a wide range of metabolic information integrated with complementary anatomical or other functional MRI sequences.
MRS provides relevant information on tumour characteristics, progression and response to treatment not available from conventional MRI [Laprie et al., 2008; Deviers et al., 2014]. Historically, $^{1}$H MRS has been focused on studying neurological disorders since the use of the technique in the brain imposes fewer technical challenges that in other organs: motion artifacts are minor, shimming (making magnetic field as homogeneous as possible) is easier to perform, and lipids are generally absent in normal brain tissue [Oya et al., 1999]. Nowadays MRS has become a valuable tool for the examination of human brain tumours, neurological disorders and also prostate and breast cancers [Kwock et al., 2006; Posse et al., 2013]. Spectroscopy of the prostate can pinpoint the location of cancer. Breast MRS can dramatically reduce the need for needle biopsy. Brain spectra can help to differentiate different tissue types in heterogeneous brain tumors or to detect tumor infiltration

onto healthy tissue.
Early MRS studies used single-voxel spectroscopy (SVS) (i.e., spectra recorded from a single , typically $8cm^3$ cube of tissue), for several reasons: they are widely available in clinical scanners, have short scan times (around 5 minutes), usually a good field homogeneity, and are relatively easy to process and interpret. However, SVS lacks spatial resolution and cannot be used to map regional metabolic variations. Since tumors are commonly heterogenous, the MR signal may greatly vary depending on the region that is sampled by SVS (see Figure 2.1) [Ricci et al., 2000]. Hence, the region-of-interest chosen for analysis will have a large influence on the results. Multi-voxel methods (known as chemical shift imaging (CSI) or magnetic resonance spectroscopic imaging (MRSI)) allow the analysis of the metabolic heterogeneity of tumors since they are able to map the spatial distribution of the lesion and the surrounding areas. In this thesis we focus on proton MRSI data from brain tumor patients.

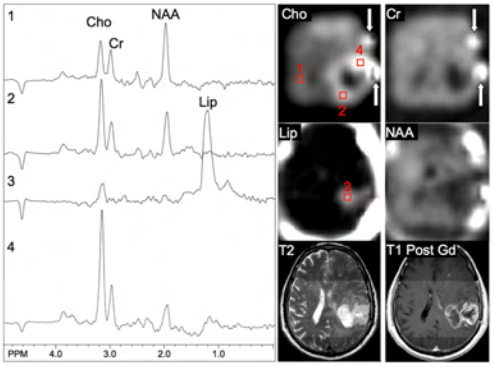


Figure 2.1: MRSI (TR/TE=1200/135 ms) and conventional MRI in a 56-year-old man who had chemotherapy after partial surgical resection of a GBM in the left temporal and inferior parietal lobe. The enhancing rim of the lesion is characterized by a high Choline signal (regions 2 and 4), while the central necrotic core (region 3) has elevated lipids and reduced levels of other metabolites. Region 1 shows the normal spectrum from the right hemisphere. Arrows in the Creatine and Choline images point to field-inhomogeneity artifacts due to surgical staples. Edited from [Horská and Barker, 2010].

### 2.3.1 Basics of magnetic resonance spectroscopy

#### 2.3.1.1 Nuclear Magnetic Resonance

MR spectroscopy relies on the same physical phenomenon as conventional MRI, the nuclear magnetic resonance (NMR), first described in 1946 simultaneously by the Nobel Prize winners Edward Purcell, from Harvard University, and Felix Bloch, from Standford University [Purcell et al., 1946; Bloch, 1946]. The use of NMR to study the the structure of biological molecules was significantly improved in the late 1960s with the development of superconducting magnets and the implementation of Fourier transform NMR. It was in the mid-1970s when NMR started to be used for the study of living biological systems, after the use of magnetic field gradients to encode NMR signals spatially was introduced [Lauterbur et al., 1973], and thus the concept of magnetic resonance imaging (MRI) was born. When an NMR technique is used in vivo and in particular in the clinic, the convention is to avoid the term "nuclear" as it may erroneously lead to associations with nuclear medicine, radioactive materials, and ionizing radiation. For this reason, in vivo NMR spectroscopy is referred to as magnetic resonance spectroscopy (MRS).
Subatomic particles like electrons, protons and neutrons are associated with "spin", a fundamental property like charge or mass. In the case of atomic nuclei with even number of protons and neutrons, individual spins are paired and the overall spin becomes zero. However, any atomic nucleus that has an odd number of protons and/or neutrons possess a net spin, called "nuclear spin". Spin can be visualised as a rotating motion of the nucleus about its own axis. Each nucleus has a unique nuclear spin, which is described by the spin quantum number $I$. Each nuclear spin also has a magnetic moment $\mu$. The nuclear spin and the magnetic moment are related by the following equation:

$$\mu = \gamma I, \qquad [2.1]$$

where the constant $\gamma$ is known as the gyromagnetic ratio and it is unique for each NMR-active nucleus. The combination of spin and charge makes that such nuclei behave like small magnets (Figure 2.2), and when a nucleus with a nuclear spin $I$ is placed in an external magnetic field, it may assume one of $2I + 1$ orientations relative to the direction of the external field.
Nuclei with this property can be observed by nuclear magnetic resonance (NMR) spectroscopy. The main nuclei used in clinical MRS are proton ($^1$H),

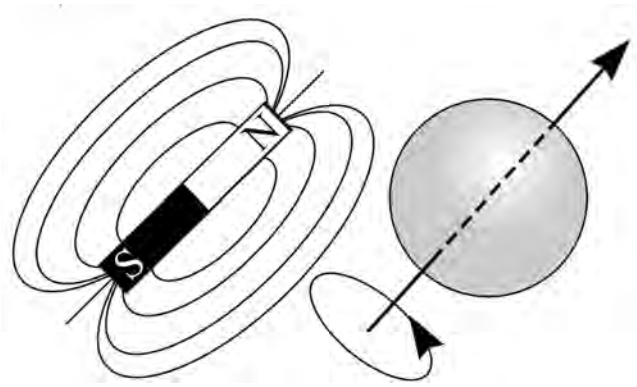


Figure 2.2: A charged, spinning nucleus creates a magnetic moment which acts like a bar magnet. Edited from http://www.voxelcube.com.

phosphorous-31 ($^{31}$P), carbon-13 ($^{13}$C) and fluorine-19 ($^{19}$F), all of which have nuclear spin $I = 1/2$. Due to its abundance in the human body, the most common nucleus used in MR is $^{1}$H. The following description of the NMR experiment will be limited to proton spectroscopy (analogous for any other nuclei with $I = 1/2$).

An NMR experiment consists of embedding a sample into a static external field $\boldsymbol{B}_0$ to align the angular momentum of the nuclei, applying a radio frequency (RF) pulse with a bandwidth chosen to excite all the nuclei within the required frequency range and acquiring the emitted response signal. In the absence of an external magnetic field, each nucleus (magnet) is randomly oriented. In the presence of an static external magnetic field, $\boldsymbol{B}_0$, the $I = 1/2$ nuclei adopt two possible orientations: either parallel (low energy) or antiparallel (high energy) to the external magnetic field (Figure 2.3). The difference in energy ($\Delta E$) between the two spin states is proportional to the strength of the applied magnetic field ($\boldsymbol{B}_0$) according to the following equation:

$$\Delta E = \frac{h\gamma \boldsymbol{B}_0}{2\pi}, \qquad [2.2]$$

where $h$ is the Planck constant ($6.626 \times 10^{-34}$ Js).

The following diagram illustrates that the two spin states have the same energy when the external field is zero, but diverge as the field increases. Nuclei in the lower energy orientation (parallel to the field) can be excited to the higher energy orientation (antiparallel to the field) by a radiofrequency

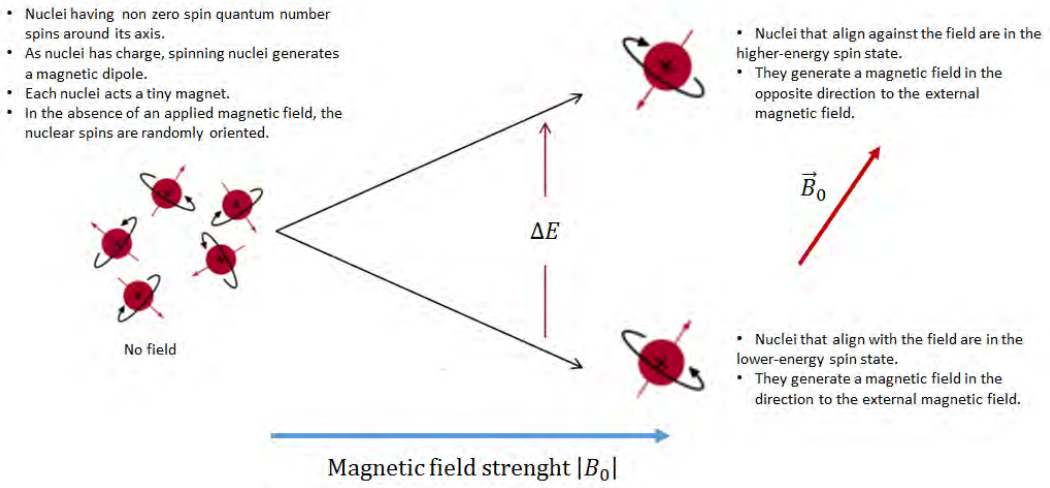


Figure 2.3: NMR-active nucleus behaves like a small magnet when it is placed in an external magnetic field.
Edited from http://chem.ch.huji.ac.il/nmr/whatisnmr/whatisnmr.html.

(RF) pulse of the correct frequency ($\nu$) according to:

$$\nu = \frac{\Delta E}{h} \qquad [2.3]$$

It follows from equations [2.2] and [2.3] that the frequency $\nu$ is related with the strength of the external magnetic field $\boldsymbol{B}_0$ by the following equation which is known as the Larmor equation:

$$\nu = \frac{\gamma \boldsymbol{B}_0}{2\pi} \qquad [2.4]$$

The Larmor equation shows that the frequency required to excite the nucleus is proportional to the strength of the external magnetic field and to the gyromagnetic ratio of the nucleus observed.
To induce transitions between both energy states, a RF pulse is applied by a coil in a plane perpendicular to the direction of the static external field $\boldsymbol{B}_0$. The frequency of the RF pulse has to correspond with the energy difference between the two states and matches to the Larmor frequency (Equation [2.4]). The RF pulse will excite simultaneously all the nuclei whose resonance frequencies are close to the frequency of the pulse. When the RF pulse is turned off, the excited nuclei quickly return to their original state (i.e., align with

$\boldsymbol{B}_0$) generating the signal that is acquired by a detector coil. The MR signal originates from the process of energy absorption by spins making a transition from the lower energy state to the higher energy state, and energy emission by spins making a transition from the higher energy state to the lower energy state. The intensity of the signal emitted by the nuclei (amount of energy) depends on the population difference between the two energy states. In thermal equilibrium, the relative amount of nuclei in the highest $n$ and the lowest $n_+$ energy state is given by:

$$\frac{n_-}{n_+} = e^{-\frac{\Delta E}{kT}}, \qquad [2.5]$$

where $k$ is the Boltzman constant ($1.381 \times 10^{-23}$ J/K) and $T$ the temperature in Kelvin.

The ratio $\frac{n_-}{n_+}$ is very close to unity because the number of spins in the low energy level is slightly higher than the number of spins in the high energy level, causing a weak net magnetic field. For example, at room temperature in a 1.5 Tesla magnetic field, there will typically be a population ratio $\frac{n_-}{n_+}$ equal to 100.000:100.006. This explains the inherently low signal-to-noise ratio (SNR) of the signal emitted when the spin system returns to equilibrium after excitation. The emitted signal is called a free induction decay (FID) signal and corresponds to an exponentially decaying sinusoid in the time domain. The FID is typically transformed to the frequency domain via Fourier transform in order to obtain a frequency spectrum. The intensity of the signal is proportional to the number of nuclei that contribute to it (i.e., the area under each peak in the spectrum is proportional to the number of nuclei generating that peak (Figure 2.4)). In order to increase the SNR, several data acquisitions are performed consecutively and the final signal is the average of all measured signals.

#### 2.3.1.2 Chemical Shift

MRS is based on the chemical shift properties of the atoms. As described above, the nuclei of a tissue exposed to an external magnetic field will resonate at a frequency ($\nu$) given by the Larmor equation [2.4]. Since the gyromagnetic ratio ($\gamma$) is a constant that is characteristic for each nuclear species, the Larmor equation [2.4] shows that the resonance frequency of the

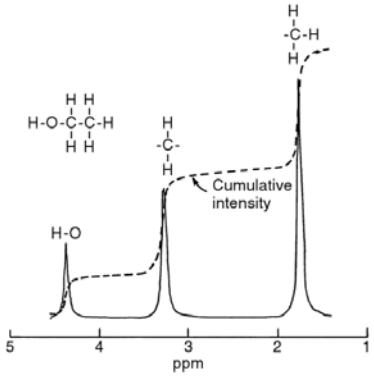


Figure 2.4: The (low resolution) proton MRS spectrum of ethanol contains three peaks. Distinct chemical groups emit signals at different frequencies. The area under each peak in the spectrum is proportional to the number of nuclei (protons) generating that peak. Edited from [Bushong, 2013].

nuclei ($\nu$) depends on the external magnetic field strength and, that nuclei of different elements have different resonance frequencies. The principle that allows the discrimination of different chemical compounds using the same isotope ($^1$H for example) is the chemical shielding effect. The electronic interactions of the nuclei with the surrounding molecules cause a change in the local magnetic field leading to a change on the spin frequency of the atom. This results in slightly different resonance frequencies for the same isotope in different molecules and even for isotopes in the same molecule but at different positions. Since the chemical structure of molecules determines the electronic environment, this shift in the frequency has been named chemical shift.

In MRS, the chemical shift of a peak in the spectrum is often expressed in terms of the dimensionless unit parts per million (ppm), which is independent of the spectrometer frequency. A metabolite that resonates at a specific ppm value for a spectrometer frequency of 63.8 MHz, also resonates at the same ppm value for a spectrometer frequency of 500 MHz. The ppm value of a resonance is the observed chemical shift in Hz from a reference frequency, often set to the frequency resonance of the Tetramethylsilane (TMS), divided by the spectrometer frequency in MHz:

$$ppm = \frac{f - f_{ref}}{f_S}, \qquad [2.6]$$

where $f$ denotes the resonance frequency in Hz, $f_{ref}$ the reference frequency also in Hz and $f_S$ is the spectrometer frequency in MHz.
For example, at 1.5 T, NAA (methyl group) has a resonance shift of 129 Hz from TMS and the Larmor frequency of protons is 63.8 MHz. Thus, the ppm frequency for NAA is:

$$ppm_{NAA} = \frac{129}{63.8} = 2.02. \quad [2.7]$$

#### 2.3.1.3 J-coupling

In addition to chemical shifts, MR spectra are also modulated by J-coupling (or scalar coupling) [Govindaraju et al., 2000]. J-coupling is the result of an internal indirect interaction of two spins via the intervening electron structure of the molecule. The coupling strength is measured in Hertz (Hz) and is independent of the external field strength. J-coupling between the same species of spins, e.g., proton and proton is termed homo-nuclear J-coupling whereas J-coupling between different species of spins, e.g., proton and phosphorous is referred to as heteronuclear J-coupling. J-coupling results in a modulation of the signal intensity depending on sequence type and acquisition parameters, particularly the echo time. The most prominent example in proton spectroscopy is lactate where there is a 7 Hz strong coupling between the two MR-detectable proton groups. Other molecules with more complex J-coupling patterns are glutamate and glutamine with three J-coupled proton groups. A spectrum of N -acetylaspartate(NAA) is shown in Figure 2.5. NAA has both uncoupled and J-coupled protons.

#### 2.3.1.4 Water suppression

$^1$H MRS spectra are dominated by the water signal. The water peak is several orders of magnitude larger than the metabolite peaks of interest. This greatly impedes the ability of the spectrometer to accurately record the metabolite signals. To avoid this high peak from water to superimpose on the signal of other metabolites, water suppression techniques are applied during the acquisition of the data. The most commonly used technique is chemical shift selective water suppression (CHESS) [Haase et al., 1985] (Figure 2.6) which uses frequency selective pulses to exclusively excite the water molecules and then a magnetic gradient to destroy their phase coherence. Other techniques sometimes used are Water suppression Enhanced Through

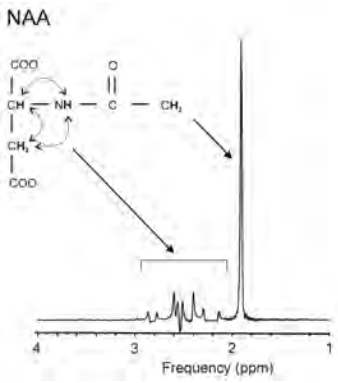


Figure 2.5: The spectrum of the N -acetyl-aspartate (NAA) molecule is shown (PRESS, echo time (TE) 35 ms, 1.5 Tesla). The NAA molecule has protons at different positions. The three protons of the -$CH_3$ group are equivalent and their individual signals add-up and give the prominent peak at 2.0 ppm. The other protons attached to carbons of NAA molecule also provide a signal. The protons of the –NH, –CH, and –$CH_2$ are in close proximity in the molecule and do interact via J-coupling (indicated by dashed arrows in above fi gure). J-couplings split peaks and modulate the phase of a signal. The result is a more complex pattern of multiple peaks, which can be asymmetric or point downwards. The signal from proton next to the nitrogen atom (amide proton) resonates at approx. 8 ppm. Due to rapid exchange with protons from surrounding water molecules, the magnetization disappears quickly and the signal from this proton is very weak. Edited from [Blüml, 2013].

T1 effects (WET) [Ogg et al., 1994] and VAriable Pulse power and Optimized Relaxation Delays (VAPOR) [Tkáć and Gruetter, 2005].

#### 2.3.1.5 Sequences and Spatial encoding

Spatial localization allows signals to be recorded from well-defined structures or lesions within the body. It is worth noting that by recording signals from smaller volumes, improved field homogeneity can be obtained [Bax and Freeman, 1980].
Spatial localization techniques for proton brain spectroscopy fall into two general categories: single-voxel techniques where a spectrum is recorded from a single volume element (voxel), and multi-voxel techniques (also called MR spectroscopic imaging (MRSI) or chemical shift imaging (CSI)) where spec-

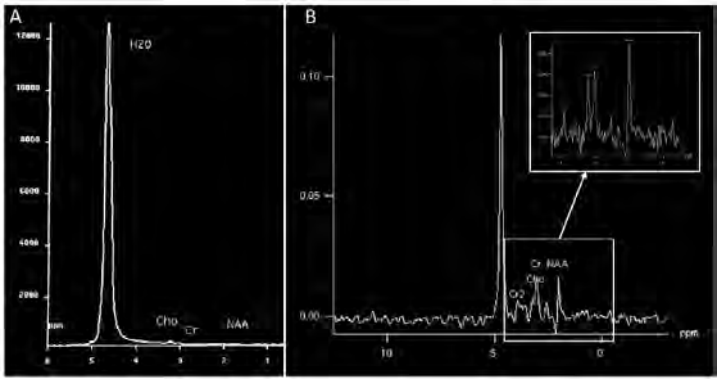


Figure 2.6: Water signal suppressing with CHESS. Brain MR spectrum before CHESS (A) and after CHESS (B). CHESS reduces the signal from water allowing brain metabolites to be depicted on the spectrum. Edited from [Bertholdo et al., 2013].

tra from multiple regions are acquired simultaneously.
The two most commonly used single voxel sequences are STEAM (stimulated echo acquisition mode) [Frahm et al., 1987] and PRESS (point resolved spectroscopy sequence) [Bottomley, 1987]. Both methods are based on three slice selective RF pulses applied in orthogonal directions (Figure 2.7 A). The STEAM sequence uses three 90° pulses and detects the resulting stimulated echo from the volume intersected by all three pulses. All other signals should be dephased by a large crusher gradient during the so-called "mixing time" (TM) between the second and third pulses (Figure 2.7 B). The PRESS sequence uses one 90° pulse and two 180° pulses to detect a spin echo from the localized volume. The second and third pulses are refocusing pulses, and crusher gradients are applied around these pulses to select the desired spin echo signal arising from all three RF pulses, and dephasing unwanted signals (Figure 2.7 C). A detailed comparison of both sequences can be found in [Moonen et al., 1989].
While single-voxel MR spectroscopy provides a signal from a certain volume, MRSI allows the simultaneous acquisition of spatially localized MR signals from a two- or three-dimensional grid of voxels. The concept of MRSI was first demonstrated on phantoms by Brown et al. in 1982 [Brown et al., 1982]. The authors showed that an array of spatially localized spectra could be reconstructed using phase encoding applied in that direction. For MRSI, a variety of different spatial encoding approaches are used, but most com-

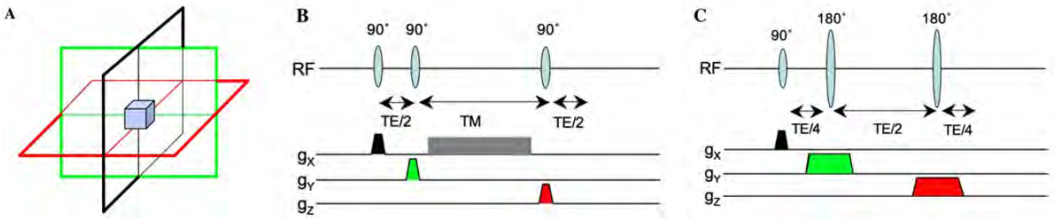


Figure 2.7: **Single-voxel localization techniques**. Spatial localization is achieved by collecting signals from the intersection of three slice-selective RF pulses applied in orthogonal directions (A). The STEAM sequence, consisting of three 90° slice selective pulses (B). The PRESS sequence, consisting of a slice selective 90° excitation pulse and two 180° slice selective refocusing pulses (C). For simplicity, only slice selection gradients are shown (except for the mixing time (TM) crusher gradient in the STEAM sequence depicted in B). Edited from [Barker and Lin, 2006].

monly the collection of spectroscopic data from multiple adjacent voxels is accomplished by the introduction of phase encoding gradients (field gradients) in the spatial directions of the grid, resulting in phase encoded FIDs. In addition to the main magnet to create a strong static magnetic field ($\boldsymbol{B}_0$), after the RF excitation pulse, gradient coils are used to generate magnetic field gradients in one, two or three dimensions. These field gradients are in the range of 10–50 mT/m with a switching time on the order of a millisecond. Spins are encoded as to position by the amount of phase encoding imparted to them based on their distance form the isocenter in the encoding gradient dimension.

In MRSI of the brain, it is is typically necessary to restrict the acquisition to a fairly small region to avoid strong lipid signals from the scalp and to reduce potential magnetic field inhomogeneities. In this case, it is typical to combine a volume selective sequence (PRESS or STEAM) with linear phase encoding along two or three directions [Brown et al., 1982] (Figure 2.8). The idea of volume pre-selected MRSI sequences is to incorporate the volume selection used in PRESS or STEAM single voxel spectroscopy into an MRSI sequence. In contrast to SVS, the PRESS excitation in MRSI is additionally combined with two- or three phase-encoding gradients. An example of reconstructed MRSI grid and selected rectangular volume of interest (VOI) is shown in Figure 2.9.

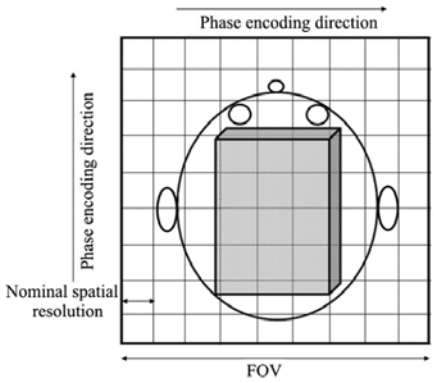


Figure 2.8: 2D spectroscopic imaging with volume pre-selection. Only the region in the rectangle is excited to eliminate spurious signals. Edited from [Skoch et al., 2008].

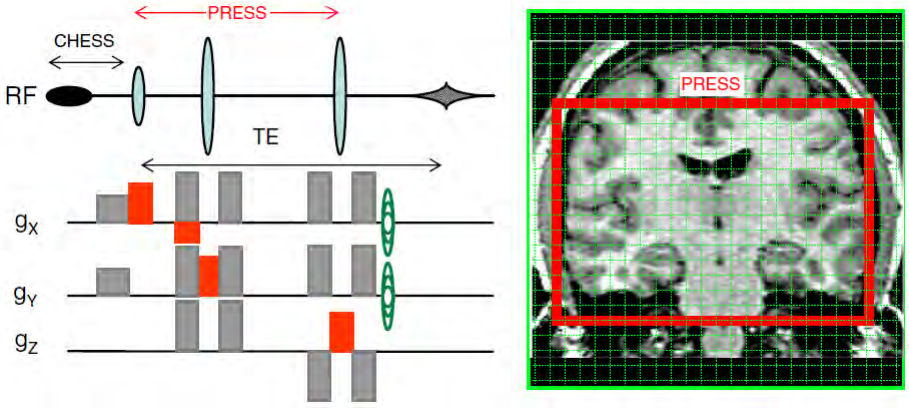


Figure 2.9: **2D-PRESS-MRSI pulse sequence**; a PRESS sequence is used to excite a large volume of brain tissue while excluding signal from lipid in the scalp and/or regions of poor field homogeneity, and then phase-encoding gradients ($g_X$ and $g_Y$) are used to localize spectra from regions within the excited region. A CHESS pulse and crusher gradient is applied prior to the PRESS sequence for water suppression. Crusher gradients applied around the 180° refocusing pulses are also shown. Edited from [Barker and Lin, 2006].

More recently, fast MRSI techniques have been developed like the parallel spectroscopic imaging techniques [Dydak et al., 2001] or the compressed sens-

ing accelerations [Hu et al., 2008; Geethanath et al., 2012; Askin et al., 2012; Shankar et al., 2015; Worthington, 2015]. The use of prospective compressed sensing approaches allows the improvement of the spatial resolution by at least a two-fold factor in each dimension at high magnetic fields (e.g., 3T). High spatial resolution MRSI and 3D MRSI techniques may especially benefit from these accelerating methods [Van der Graaf, 2010].
The resolution of the MRSI data is limited due to the intrinsic low SNR of the signals, requiring adequately large voxel volumes. The spatial resolution of MRSI is lower than the one of conventional MRI (Figure 2.10).

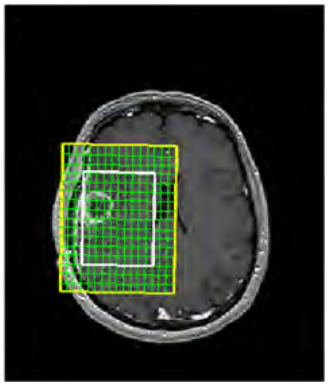

Figure 2.10: T1-weighted MRI with a grid overlay indicating the spatial resolution of the MRSI data. MRI has a spatial resolution of about 1 millimeter, while MRSI is in the range of several millimeters to a centimeter.

#### 2.3.1.6 Acquisition parameters in MRS

In addition to the actual concentration of the metabolites, the MR signal will be influenced by many parameters, such as the strength of the magnetic field, echo time, repetition time, localization technique, as well as the longitudinal (T1) and transverse (T2) relaxation times of the metabolites. With the exception of the relaxation times, these parameters can be controlled.
As previously described (Equation [2.5]), there are only few more protons that adopt the parallel (low energy) position than in the antiparallel (high energy) position. However, this is sufficient to generate a net magnetisation ($\boldsymbol{M}$) aligning with the main magnetic field $\boldsymbol{B}_0$ (conventionally direction of the z-axis) (Figure 2.11).

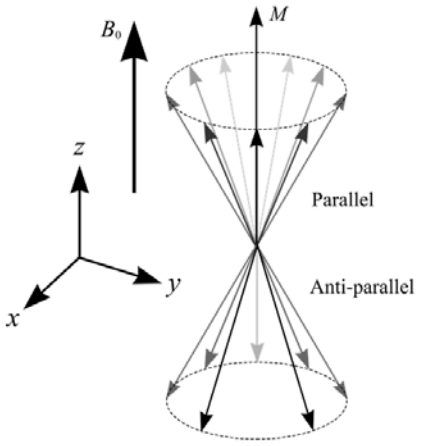


Figure 2.11: The number of spins in the low energy level (parallel to $\boldsymbol{B}_0$) is slightly higher than the number of spins in the high energy level (anti-parallel to $\boldsymbol{B}_0$), causing a weak net magnetic field $\boldsymbol{M}$. At equilibrium, the net magnetization $\boldsymbol{M}$ is aligned with the external static magnetic field $\boldsymbol{B}_0$. Edited from http://www.voxelcube.com.

The application of a RF pulse alters the population ratios, and creates a transverse magnetic field component ($M_{xy}$). The greater the amount of energy applied by the RF pulse, the greater the angle that the net magnetisation makes with the $\boldsymbol{B}_0$ field (the z axis). This depends on both the amplitude and duration of the pulse. The RF pulse is switched off once the angle of the RF pulse has reached a prescribed value. This is known as the flip angle of the RF pulse (Figure 2.12).
When the RF pulse stops, the magnetization vector $\boldsymbol{M}$ recovers until it reaches its equilibrium value $\boldsymbol{M}_0$. The return of $\boldsymbol{M}$ to its equilibrium state (the direction of the z-axis) is known as **relaxation**. This relaxation process is characterized by two independent factors: the **T1 relaxation**, characterizing the return of the original magnetization along the main magnetic field, and the **T2 relaxation**, characterizing the exponential decay of magnetization in a plane perpendicular to this field. T1 relaxation also referred to as spin-lattice relaxation or longitudinal relaxation, describes the return of the excited magnetization vector $\boldsymbol{M}$ to equilibrium in the direction of the magnetic field (conventionally shown along the z-axis) (Figure 2.13). Following termination of an RF pulse, nuclei will dissipate their excess energy as heat to the surrounding environment (or lattice) and revert to their equilibrium

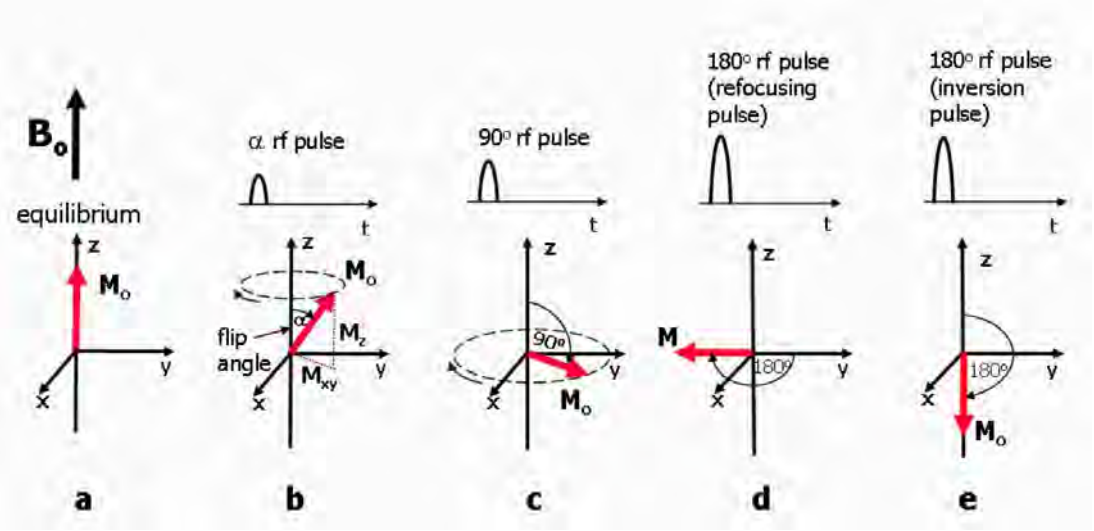


Figure 2.12: At equilibrium, the net magnetisation, $\boldsymbol{M}$, is aligned along the z axis (a). When an RF pulse is applied, $\boldsymbol{M}$ makes an angle with the z-axis, known as the flip angle, and rotates around the axis (b). At any instant the magnetisation can be split into two components, $\boldsymbol{M}_z$ and $\boldsymbol{M}_{xy}$. The rotating $\boldsymbol{M}_{xy}$ component generates the detectable MR signal. This pulse has a 90° flip angle (c). A 180° RF refocusing pulse (d). A 180° inversion pulse (e). Edited from [Ridgway, 2010].

position. The recovery of $\boldsymbol{M}_z$ is an exponential process with a time constant T1:

$$\boldsymbol{M}_z = \boldsymbol{M}_0(1 - e^{-t/T1}), \qquad [2.8]$$

where T1 is the time taken for approximately 63% of the longitudinal magnetisation to be restored following a 90° pulse.

T2 relaxation is also referred to as spin-spin relaxation or transverse relaxation and describes the decay of the excited magnetization vector perpendicular to the applied magnetic field (conventionally in the xy plane). The observed spectral line-width is related to the T2. T2 relaxation is affected by magnetic inhomogeneity and the overall term for the observed loss of phase coherence is called T2* relaxation. T2* relaxation accounts for the more rapid decay of the FID signal due to the additional de-phasing caused by local inhomogeneities in the magnetic field. Both T2 and T2* are exponential processes with times constants T2 and T2*, respectively. This is the time at

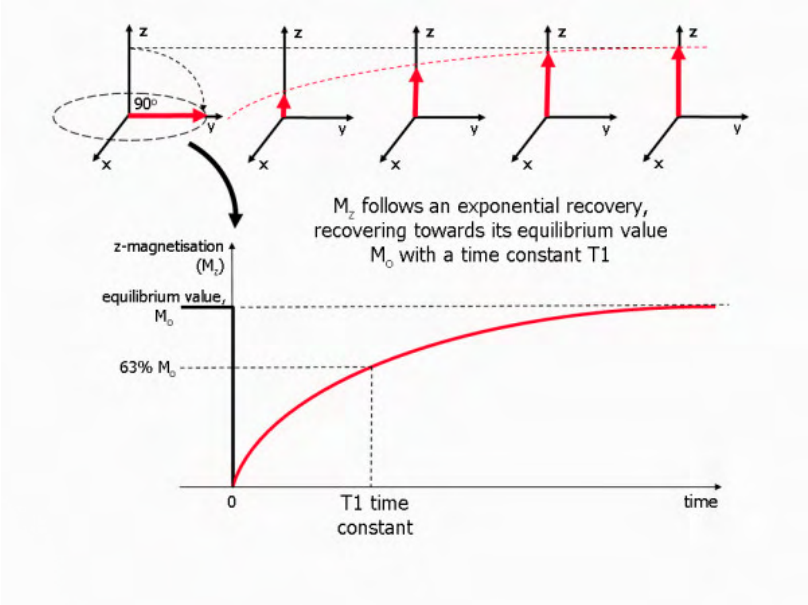


Figure 2.13: Process of T1 relaxation after a 90° RF pulse is applied at equilibrium. The z component of the net magnetisation, $\boldsymbol{M}_z$ is reduced to zero, but then recovers gradually back to its equilibrium value if no further RF pulses are applied. Edited from [Ridgway, 2010].

which the magnetization has decayed to 37% of its initial value immediately after the 90° RF pulse.
Various tissues and substances have particular T1 and T2 values. The most important determinant is the size and motion of the molecule on which the hydrogen nucleus is embedded. Small and rapidly rotating molecules (like water) have long T1 and T2 times. As molecular motion slows (as in proteins), T2 shortens and T1 again increases.
By adjusting scanning parameters (e.g. repetition time and echo time described below), differences in T1 and T2 relaxation characteristics among tissues can be highlighted to emphasize certain MR image contrast properties. The relaxation properties and the acquisition parameters also affect the appearance of MR spectra. Each metabolite in a MR spectrum has its own longitudinal and transversal relaxation characteristics and the signal strength of the spectral peaks vary depending on the acquisition parameters.

**Echo time (TE)** is the time from the application of an excitation RF pulse

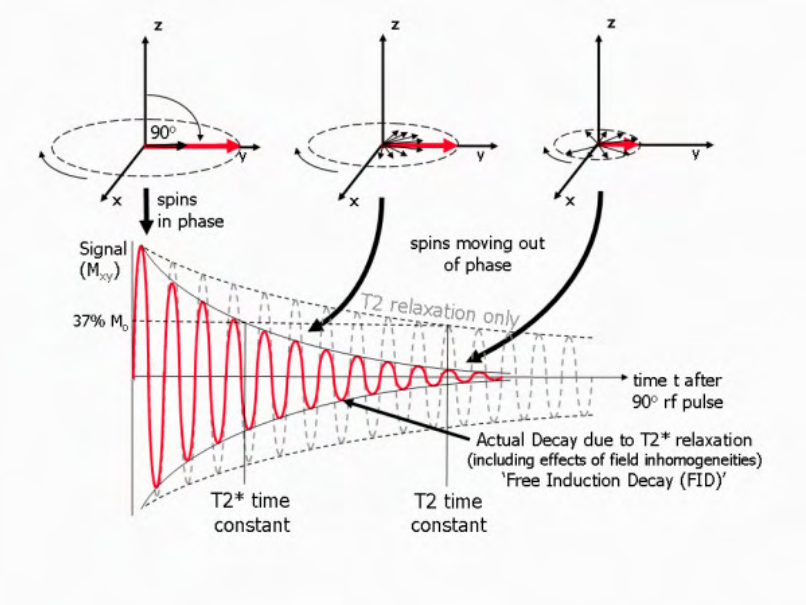


Figure 2.14: Process of transverse (T2) relaxation after a 90° RF pulse is applied at equilibrium. Initially the transverse magnetisation (red arrow) has a maximum amplitude as the population of proton magnetic moments(spins) rotate in phase. The amplitude of the net transverse magnetisation (and therefore the detected signal) decays as the proton magnetic moments move out of phase with one another (shown by the small black arrows). Edited from [Ridgway, 2010].

to the measurement of the MR signal. During this time, the signal from each metabolite relaxes with its own characteristic T2-relaxation time. TE determines how much decay of the transverse magnetisation is allowed to occur before the signal is measured. It therefore controls the amount of T2 relaxation.

Choosing long echo times simplifies spectra because the number of detectable metabolites is reduced. Long TE (TE $>$ 135 ms) is typically used in clinical practice because of a flat baseline (no macromolecular contribution) and because the three main metabolites detected at these echo times (NAA, Creatine, Choline) can be easily identified. Short TE (TE $\leq$ 35 ms) allows the detection of an increased number of metabolites and has an SNR advantage over long TE. However, short TE spectra suffer from severe baseline (short T2 signals of macromolecules) and lineshape (stronger gradients are required

for shorter duration) distortions which makes spectra analysis more difficult (Figure 2.15).

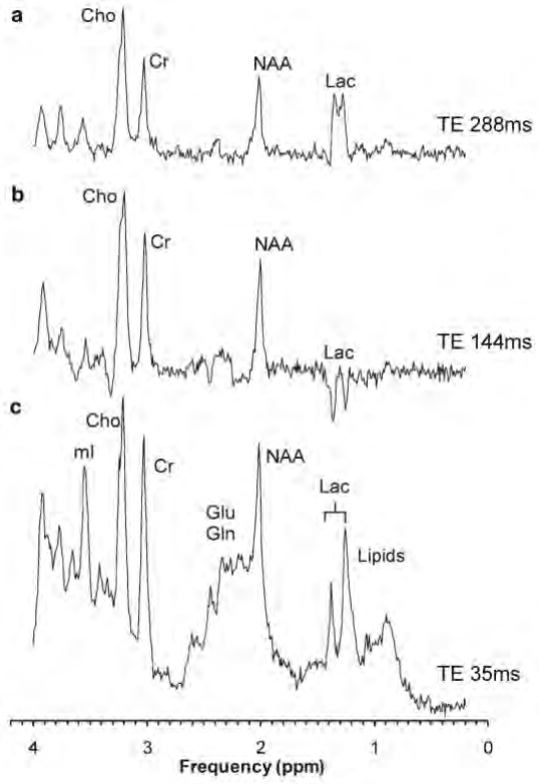


Figure 2.15: Three MR spectra of the same voxel acquired with echo times of TE = 288 ms ( top ), TE = 144 ms (center), and TE = 35 ms (bottom). Edited from [Blüml, 2013].

**Repetition time (TR)** is the time interval between two consecutive RF pulse sequences measured in milliseconds. For a given type of nucleus in a given environment, TR determines the amount of T1 relaxation. The longer the TR, the more the longitudinal magnetisation is recovered. Tissues with short T1 have greater signal intensity than tissues with a longer T1 at a given TR. A long TR allows more magnetisation to recover and thus reduces differences in the T1 contribution. Spectra acquired with repetition times that are substantially longer than the T1-relaxation times are compromised by lower signal-to-noise ratio. For that reason, repetition times are generally

set to approximately 1–1.5 times the T1-relaxation times of metabolites. In contrast to TE, the repetition time does not influence significatively the appearance of MR spectra. It only causes different scaling of the peaks [Blüml, 2013].

**Mixing time (TM)** The mixing time (TM) is the time delay between the second and the third 90° RF pulse in a STEAM sequence.

### 2.3.2 $^{1}$H MRSI-visible metabolites

Depending on the clinical question, many major metabolites can be measured with MR spectroscopy. Spectra from human brain (TE 135ms) are shown in Figure 2.16.

**N-acetylaspartate (NAA)**, which resonates at 2.01 ppm, is the most abundant metabolite visible on MRS (after the water) in healthy human brain. NAA is considered a neuronal marker and is present only in neurons, axons, and dendrites. It is found to be decreased in most brain tumors [Stadlbauer et al., 2007]. A decrease in NAA level is usually associated with neuronal loss or damage.

**Choline (Cho)** (3.22 ppm) represents the constituents of cell membranes. Increased Cho is associated with increased concentration of cells and/or cell membrane synthesis such as cancer.

**Creatine (Cr)** (3.02 and 3.8 ppm) is a marker for cell energy metabolism. Decreased in Cr is associated with tissue death or necrosis.

**Lactate (Lac)** is not seen or is hardly visualized in the normal brain. The doublet signal of lactate at 1.33 ppm appears in phase (short/long TE) or in opposed phase (TE of 135-144 ms) to other signals. Lac is a product of anaerobic glycolysis so its concentration increases under anaerobic metabolism such as cerebral hypoxia, ischemia, seizures and metabolic disorders (especially mitochondrial ones).

**Mobil lipids (Lip)** (1.3 and 0.9 ppm) Mobil lipids are absent in normal brain, unless the volume of interest is placed too close to the skull (allowing extracranial lipid signals to contaminate the spectrum). Increased lipids

concentration is observed when there is cellular membrane breakdown, and have been associated with the degree of malignancy, with metastases and the presence of necrosis [Kuesel et al., 1994; Negendank et al., 1996; Murphy et al., 2003].
Table 2.17 summarizes the main metabolites from in vivo $^{1}$H-MRS brain and their biological significance.

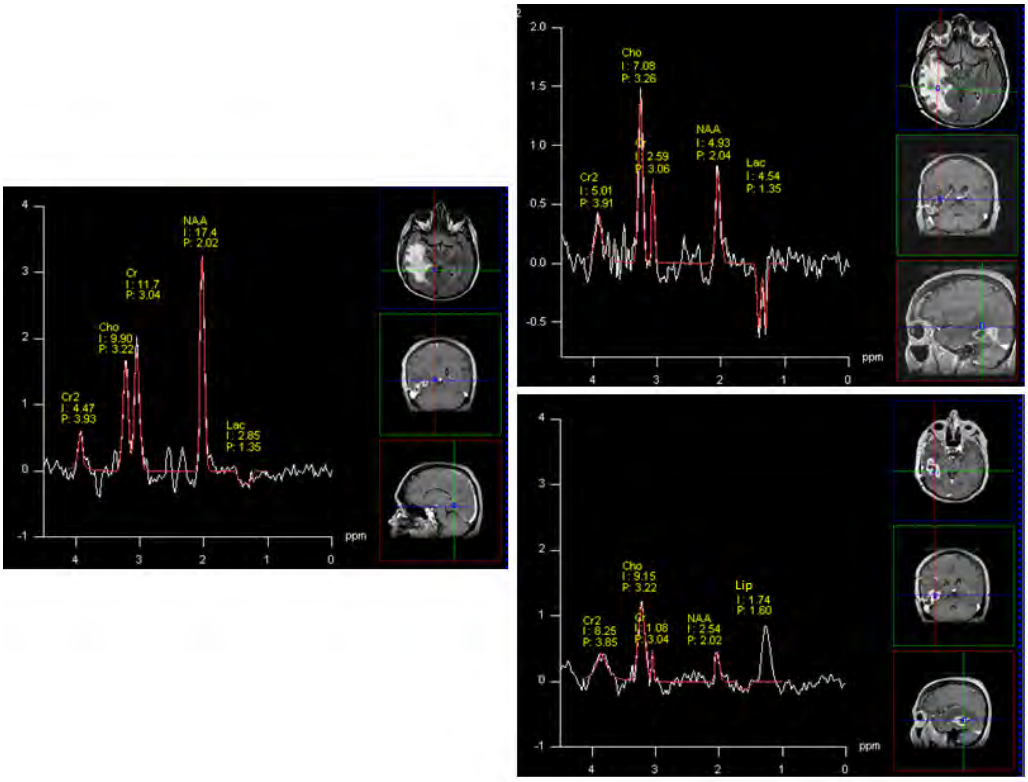


Figure 2.16: Examples of normal spectrum (left) and abnormal spectra (middle and right). Compared to the normal spectrum, the abnormal spectra show increased Choline, decreased levels of Creatine and NAA and the presence of Lactate (middle) and Lipids (right).

The principal metabolites in $^{1}$H-MRS and their biological significance

| Metabolite | Description | ppm | Decreased | Increased | TE |
|---|---|---|---|---|---|
| NAA | A neuronal marker of density and viability<br><br>An axonal marker | 2.02 | Decreased in absence of neurons and axons in most tumors or white matter disease such as multiple sclerosis | Canavan's leukodystrophy | Short/long |
| Choline | A metabolic marker of cell density and membrane integrity | 3.22 | | It is increased due to cell proliferation and breakdown of cell membranes<br><br>Higher choline levels are shown in higher grade tumors compared with lower grade tumors | Short/long |
| Creatine | A marker of energy metabolism | 3.02 | Decreased phosphocreatine is an inconstant finding in tumors | | Short/long |
| Lactate | Under normal circumstances, lactate is present only in minimum amounts in the brain and is not resolved using the normal spectroscopic techniques<br><br>Glycolysis | Doublet (twin peak) at 1.33 ppm | | Increased lactate is the effect of the high rate of glycolysis<br><br>It accumulates in cystic or necrotic areas<br><br>Variable projection of the peak at different TEs | Short/long<br><br>Using intermediate TEs (135/144 ms), the doublet peak is inverted below the baseline<br><br>Using very short or very long TE (30 or 288 ms), the doublet peak projects above the baseline |
| Myoinositol | Most important osmolyte<br><br>Glial marker: located exclusively in astrocytes | 3.56 | | It is a marker for low-grade gliomas; it is only seen at short acquisition times | Short |
| Glutamine and glutamate | Glutamate is an excitatory neurotransmitter | 2.05–2.5 Complex peak | | Glutamate is viewed as an important neurotoxin when its concentration exceeds that needed for neurotransmission<br><br>It is also a participant in the redox cycle | Short |
| Lipids | May indicate tumor necrosis or voxel contamination by diploic space fat, scalp, and subcutaneous tissue | 0.9 and 1.3 ppm usually large broad peaks | | Tumor necrosis | Short<br><br>Membrane lipids have very short relaxation times and are not usually visualized on intermediate or long TE |

ppm, parts per million; TE, echo time; NAA, N-acetylaspartate.

Figure 2.17: Main metabolites from in vivo $^{1}$H-MRS brain and their biological significance. Edited from [García-Figueiras et al., 2016].

## 2.4 Radiotherapy guided by MRSI

Radiotherapy (RT) is a local cancer treatment that uses ionizing radiation to destroy tumor cells. It has become the standard post-surgical treatment

modality for glioblastoma (GBM), the most common and deadliest of malignant primary brain tumors in adults [Stupp et al., 2005]. In fact, it has demonstrated a dose-dependent antitumoral efficiency (up to 60 Gy) for this type of tumor, and it has also allowed a significant increase of the patient median survival compared to surgery alone or followed by chemotherapy [Walker et al., 1978; Kristiansen et al., 1981].

The field of radiation oncology relies heavily on imaging modalities. From initial consultation to treatment completion, images are used to guide nearly every step of the patient. The standards in radiotherapy of brain tumors are currently based on anatomic imaging techniques, usually CT and MRI.

Despite the survival benefit associated with adjuvant radiation, more than 90% of the GBM patients develop local tumor recurrence within the irradiated areas [Minniti et al., 2010; McDonald et al., 2011]. Therefore, there is interest in increasing the dose to specific and more aggressive parts of the tumor while sparing normal tissue, using new technologies such as intensity-modulated radiation therapy (IMRT). Conventional imaging modalities may not reliably identify regions of active tumor or tumor infiltration [Payne and Leach, 2014], and they are insufficient to determine the potential target for a dose escalation. Therefore, there is a need of incorporating other modalities into the RT planning process, which may provide more specific information about the lesions.

MRSI is an interesting modality in RT planning due to its ability to provide valuable information on tumor biology not available from conventional imaging modalities [Laprie et al., 2008; Deviers et al., 2014]. The additional biological information provided by this technique can be used for the development of more targeted therapies, for example, to define new target volumes for dose escalation in RT treatments. The ability of MRSI to detect areas of high metabolic activity linked to tumor cell proliferation is particularly useful for radiotherapy treatment planning because the most aggressive areas of the tumor may be targeted with higher radiation dose, potentially improving local control without excessive irradiation to the normal adjacent tissues. The potential of MRSI to define new biologically tailored target volumes for dose escalation in radiotherapy treatments is shown in Chapter 6.

There are two main difficulties slowing the integration of MRSI into the RT workflow. First, there is no standardized treatment of MRS(I) signal analysis, and second, the metabolic maps obtained after post treatment are not delivered in a DICOM standard format compatible with the treatment planning system (TPS). A reliable and reproducible integration technique of

MRSI metabolic maps is needed [Ken et al., 2013]. These limitations are addressed throughout the different chapters of this thesis.

## 2.5 MRSI data

As described in Section 2.3.1.5, MRSI provides MR signals from a two- or three dimensional grid of multiple adjacent volume elements, called voxels, within a body volume. In this thesis we focus on the processing of MRSI data. Synthetic and in vivo MRSI datasets are used in the different experiments described throughout the manuscript.

### 2.5.1 Synthetic data

Simulated MRSI datasets used in this thesis were generated by combining profiles from the principal metabolites observed in long echo time brain MR spectroscopy: choline (Cho), creatine (Cr), N-acetyl-aspartate (NAA) and lactate (Lac). Metabolite profiles were obtained from quantum mechanical simulations of a spin-echo MR experiment using the jMRUI software package [Stefan et al., 2009] (Figure 2.18).

### 2.5.2 In vivo data

In vivo data were acquired from healthy volunteers as well as from patients with diagnosed glioblastoma (GBM) included in a prospective clinical trial.

#### 2.5.2.1 Healthy volunteers

In vivo MRSI data from healthy volunteers were acquired at Institut Claudius Regaud using a 1.5T clinical MR scanner (Siemens Magnetom Avanto) using a 3D CSI sequence with water suppression, TE=135 ms, TR =1500 ms, 512 FID data points, 4 averages, slice thickness: 15mm, matrix size: $16 \times 16$, FOV: $160 \times 160$ mm yielding a voxel size of 10 mm $\times$ 10 mm $\times$ 15 mm.

#### 2.5.2.2 Patients

Data were acquired from patients with diagnosed GBM included in a phase III prospective clinical trial named Spectro-Glio. The use of this data has

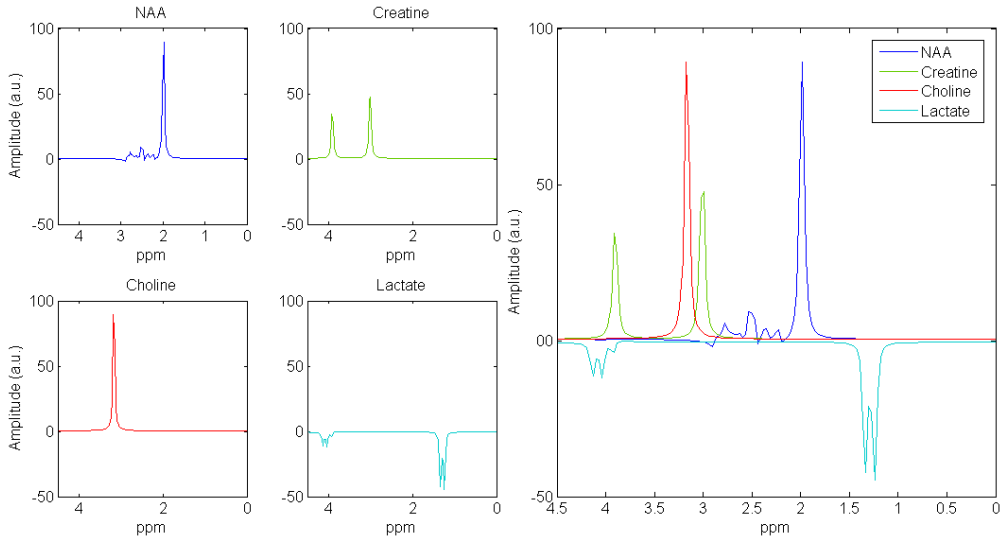


Figure 2.18: Simulated metabolite profiles.

been approved by ethics committees. GBM is the most common and deadliest of malignant primary brain tumors in adults. Preliminary studies suggest that the integration of MRSI into radiotherapy planning for these type of tumor is feasible and safe[Laprie et al., 2008; Deviers et al., 2014].

**Spectro-Glio** is a French multi-institutional phase-III clinical trial promoted and coordinated by the Institut Claudius Regaud. This ongoing trial, started on March 2011, plans to include 220 patients with GBM. It has been designed to compare two radiotherapy treatments for GBM: the "standard treatment" for which patients are treated according to the protocol Stupp (i.e., 60Gy to the planning target volume (PTV) with concomitant Temozolomide) and the "experimental treatment" in which patients receive an additional boost of 12 Gy into the gross tumor volume (GTV) and metabolically abnormal CNR2 areas (Choline-over-NAA ratio higher than 2) with intensity-modulated radiotherapy (Figure 2.19). Patients are stratified according to the main prognostic factors recognized in this disease. More information about the trial and the participant centers can be found here: https://clinicaltrials.gov/ct2/show/NCT01507506.

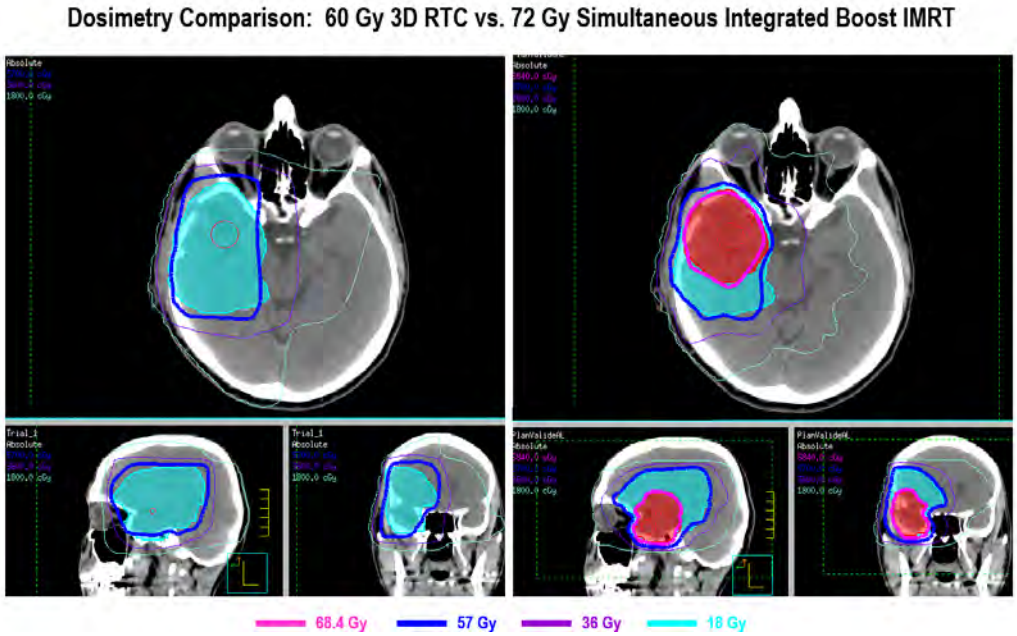


Figure 2.19: Patients in the experimental arm receive a boost of 72 Gy (instead of conventional 60 Gy) into the GTV and the CNR2 areas. Edited from [Ken et al., 2013].

## 2.6 Conclusion

This chapter presented the important role of imaging in the evaluation of brain tumor patients. While morphological imaging is the most commonly used technique, the introduction of new functional MRI modalities has improved the characterization of tumors. One of such techniques is MRSI, which provides the metabolism characterization of the sampled tissue. This chapter described the principles and basics of MRSI, and introduced its role into the RT context. Due to its ability to provide information on tumor biology, MRSI is an interesting modality in radiotherapeutic management of brain tumors. Its integration into the RT treatment planning, allows the development of more targeted therapies, for example, by the definition of biologically tailored target volumes for dose escalation.

# Chapter 3

# MRSI processing

## Contents



## 3.1 Introduction

An MRSI acquisition is basically very similar to that of MRI. However, in addition to an adequate spectral acquisition technique, advanced methods of analysis are needed for obtaining a clinically useful spectrum with an optimal signal-to-noise ratio (SNR) that allows the separation of the most significant metabolites. MRS(I) data analysis is usually divided into two stages. Firstly, preprocessing methods are applied in order to improve the quality of experimental MRSI data. Preprocessing of the MRS(I) data is a crucial step due to the low SNR of in vivo MRS(I) signals and the experimental conditions decreasing the quality o the data. In a second step, methods to interpret and/or to extract useful information from the data are performed.

## 3.2 Pre-processing

In vivo MRSI signals are affected by a number of limitations resulting in a decreased quality of the data. Some of such limitations are the following:
- presence of residual water signal (proton MRS),
- low concentrations of the observed metabolites,
- restricted measurement time,
- inhomogeneity of magnetic fields,
- fast decaying signals from immobile components,

- overlapping signals from relatively mobile components,
- physiologic motion.

Therefore, the quality of experimental MRSI data is often insufficient to extract reliable information directly after the acquisition. It is then necessary to perform a preprocessing step to remove or reduce the irrelevant information, while enhancing the key features of the data. There are a variety of preprocessing methods that considerably improve the quality of the signals by appropriate manipulation of the data. Due to the correspondence of FID and spectrum, pre-processing steps are performed either in the time or frequency domain. Typical preprocessing methods applied to MRSI data are briefly described below.

### 3.2.1 Water suppression

In vivo $^{1}$H MRSI signals are dominated by the signal from water. Even using frequency selective pulse sequences such as CHESS to reduce the strength of the acquired water signal, it remains significantly larger than any of the metabolites of interest. Such a large signal has a considerable overlap with the metabolite peaks, and a corresponding negative impact on their quantification. An effective technique used for residual water suppression is the Hankel singular value decomposition (HSVD) algorithm [Laudadio et al., 2002]. This method decomposes the MR signal into a set of exponential decays, then identifies which ones belong to the water peak and selectively subtracts those from the input signal (Figure 3.1).

### 3.2.2 Zero padding

Adding zeros to the acquired FID does not bring any additional information, but it increases the digital resolution of the signal in the frequency domain. A better digital spectral resolution helps with the characterization of the line shapes in the spectrum when, for example, frequency domain quantification methods are used.

### 3.2.3 Baseline correction

MR spectra are affected by the presence of residual water and/or strong signals arising from lipids and macromolecules that is referred to as the

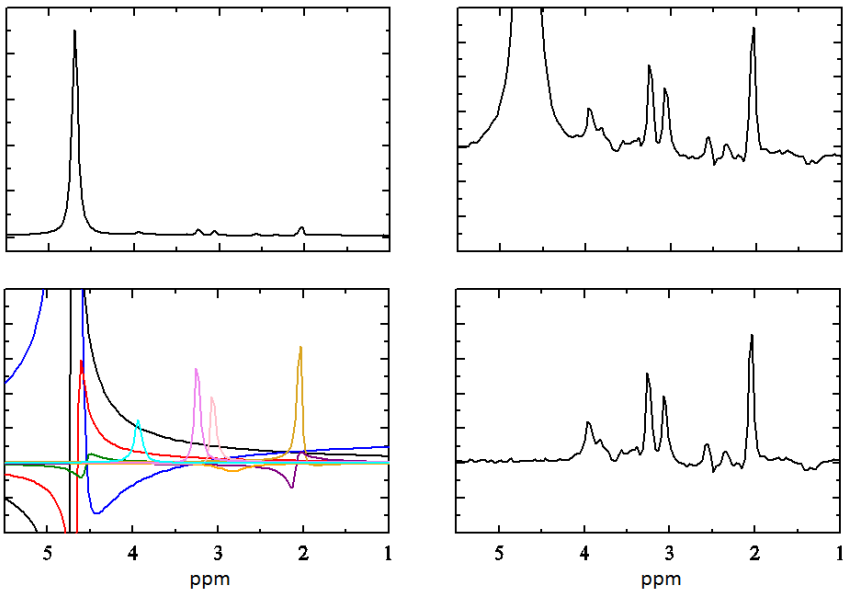


Figure 3.1: Example of water suppression with HSVD. Top row: spectrum from normal brain tissue. Small metabolite peaks are not visible in the presence of a large water peak. On the top right and on the bottom row the y-axis is scaled to show the metabolites more clearly. In the bottom left we see the set of Lorentzians fitted by the HSVD algorithm, while on the right the spectrum is shown after the subtraction of the water signal. Edited from [Rowland et al., 2013].

baseline. The baseline usually overlap with the metabolite signals which complicates the assessment of the intensity of the metabolites. The macromolecular contributions may provide relevant clinical information, if properly evaluated [Hofmann et al., 2001]. However, in order to facilitate the quantification of the metabolite signals, the baseline is usually removed. The baseline can be suppressed during the acquisition using specific sequences based on T1 relaxation such as the inversion-recovery [Knight-Scott, 1999] or the saturation-recovery sequences [Hofmann et al., 2001]. Baseline removal can also be based on T2 relaxation by increasing the echo time [Kreis et al., 1993]. Alternatively, the baseline can be corrected in a preprocessing step. A straightforward approach is the truncation of the initial points of the FID [Ratiney et al., 2005]. The baseline signal decays very rapidly, thus removing the initial part of the FID results in a suppression of the baseline

components. However, this procedure may also suppress part of the metabolite contributions and may lead to reduced accuracy of the estimates due to a decreased SNR. Numerical methods based on polynomials and splines to fit a smooth function below the actual spectrum are widely used [Güntert and Wüthrich, 1992; Cobas et al., 2006; Xi and Rocke, 2008; De Sanctis et al., 2011].

### 3.2.4 Frequency alignment

The chemical shifts of in vivo metabolites can vary due to variations in the physiological and experimental conditions (tissue, temperature and pH). The resonance frequency of the observable metabolites is known and can be used for shifting the full spectra such that the recognizable peaks reach the desired frequency locations.

### 3.2.5 Phase correction

The usual phase correction term consists of two components, one frequency-dependent (first order phase) and one frequency-independent (zero order phase). Normally, zero-order and first-order phase corrections are required for NMR spectra in order to restore pure absorption and dispersion shapes. The zero-order phase misadjustment arises from the phase difference between the reference phase and the receiver detector phase. The first-order phase mismatch can be a result of the time delay between excitation and detection, flip-angle variation across the spectrum, and phase shifts from the filter employed to reduce noise outside the spectral bandwidth [Chen et al., 2002]. Phase correction can be performed manually or using automatic algorithms like the Ernst's method [Ernst, 1969], Dispa [Craig and Marshall, 1998] and eDispa [Cobas and Sykora, 2007], Shanon's entropy minimization [Chen et al., 2002] and Automics [Wang et al., 2009].

### 3.2.6 Denoising

The SNR of MRSI data is intrinsically low due to the low concentration of the metabolites of interest (around 3 orders of magnitude below that of water [Van den Boogaart et al., 1994]). In addition, there are various sources of noise affecting the quality of the data, such as the thermal motion of the

charged particles in the sample, or the thermal motion of the electrons in the coil and reception paths. Under normal circumstances the latter is the major source of noise in the MR signal. The noise in an MRS(I) acquisition is typically characterized as being additive Gaussian with zero mean and constant standard deviation in time. The SNR can be improved by increasing the signal using higher magnetic field strength. However, the implementation of MRSI at high fields (7 Tesla and beyond) is still challenging due to technical limitations that may reduce the expected SNR, such as increased field inhomogeneity [Boer et al., 2012]. In fact, currently, clinical manufacturers do not support field strength higher than 3 Tesla. Signal averaging is a widely used technique to improve SNR at acquisition time. However, this approach is not feasible because of the lengthening of the already long acquisition times (around 20 minutes for a standard PRESS 3D-MRSI at 1.5 Tesla with a quadrature head coil and spatial resolution of $1cm^3$). Moreover, physiological motion may lead to destructive averaging due to variations in signal phase and frequency. Therefore, methods enabling the improvement of the SNR after the acquisition are of great interest. The post acquisition noise reduction by means of signal processing is called denoising. A popular method in MR spectroscopy is to apply apodizing filters. The FID is multiplied pointwise by some appropriate function/filter in order to force the signal to decay. This technique is tipically used for MR signals to avoid the spurious peaks that are present in the spectrum when the FID has not decayed completely by the end of the acquisition. Apodization techniques often compromises the spectral resolution of the data [Bartha et al., 1999]. For a better trade-off between SNR and resolution, many advanced denoising methods specifically designed for MRSI data have also been proposed [Diop et al., 1994; Cancino-De-Greiff et al., 2002; Ahmed, 2005; Bao and Maudsley, 2007; Eslami and Jacob, 2009a; Nguyen et al., 2010]. These methods can be categorized into two classes:

1. methods without exploiting spectral models and
2. methods explicitly using spectral models.

In the first case, a popular method to denoise MRS signals is to apply wavelet shrinkage [Cancino-De-Greiff et al., 2002]. In [Ahmed, 2005], MRS signals are consecutively projected and filtered in different domains using time-frequency (SLTF) transforms. This method provides some improvement compared with the single-voxel wavelet shrinkage, but at the cost of an increased computational time. These methods process each MR spectrum independently and do not explore the spatial context of MRSI data.

The methods in the second class make use of spectral models for denoising MRSI data either prior to or during metabolite quantitation [Diop et al., 1994; Bao and Maudsley, 2007; Eslami and Jacob, 2009a; Nguyen et al., 2010]. Most of these methods incorporate constraints on the spectral profile, either by using explicit parametric models or by assuming particular line-shape characteristics. Consequently, they tend to bias the interpretation of the measured signal towards the prior assumptions. In addition, these methods are often dependent of several parameters. For example, a popular denoising method described in [Diop et al., 1994] makes strict use of the Lorentzian lineshape of the spectral peaks and is very sensitive to noise. In [Nguyen et al., 2010], an autoregressive spectral constraint is used to describe the spectral structure. This approach imposes a weaker spectral constraint than explicit parametric modeling methods. However, it incorporates a spatial smoothness constraint limiting its ability to capture the spatial variations exhibited by in vivo scans, especially in the context of lesions. A less-constrained approach was proposed in [Eslami and Jacob, 2009a], where spatial piecewise smoothness is combined with a sparse spectral model. This method makes use of a spatial total variation (TV) regularization that is known to lead to an increase of the reconstruction noise under certain experimental conditions [Liu et al., 2009].
In Chapter 4, a novel denoising method using an hybrid spatio-spectral regularization is proposed. Unlike previous denoising methods, the proposed approach does not use constraints on the spectral profile, and it explores both the spectral and the spatial dimensions of the data.
In Chapters 5 and 7, novel processing methods to interpret MRSI data integrating this denoising scheme are proposed.

## 3.3 Processing

Two basic approaches for the evaluation of MRSI data can be distinguished: quantification-based methods and pattern recognition (PR) techniques.

### 3.3.1 Quantification

The peaks in the MR spectra correspond to observable metabolites which can be used as biomarkers of diseases. Quantification consists on the estimation of spectral parameters from measured data. Signal amplitude (in the

time-domain) is the main parameter of interest since it is proportional to the metabolite concentration. Quantification is the most extended approach to extract information from MRSI data and it is usually performed by fitting mathematical models to the resonance signals. Quantification is typically expressed as a nonlinear least squares (NLS) problem. In the presence of artifacts and/or severe noise, the NLS problem can have many local optima and the result becomes very sensitive to the choice of initial values. Prior knowledge about the sought signal is used in some quantification methods to alleviate these problems, but it can lead to an estimation bias in cases where the employed prior knowledge is inadequate.
A brief description of the existing methods and a novel quantification technique are described in Chapter 5.

#### 3.3.1.1 Absolute quantification

The area of a resonance peak in a phased MR spectrum is proportional to the absolute concentration of the corresponding metabolite, but it also depends on the relaxation times, T1 and T2 (which differ between different body regions) and on instrumental factors. This makes absolute quantification of metabolite concentrations difficult. A careful calibration is needed to convert peak areas to metabolite concentrations to which the metabolite signals are referenced. Absolute concentrations are expressed in biochemical units such as molarity (number of moles of metabolite per liter of tissue water) and molality (number of moles of metabolite per kilogram of tissue water). There are different absolute quantification strategies:
**External reference:** A sample with a known reference solution and relaxation properties is positioned near or inside the RF coil. Immediately after the acquisition of the in vivo spectrum, a reference spectrum from the calibration sample is obtained.
**Water signal reference:** Tissue water is used as an internal standard. The in vivo measurement is performed first. Then, from the same voxel, the signal from unsuppressed tissue water is recorded, which serves as an endogenous concentration reference. Alternatively, the water content can be derived from proton-density–weighted images.
**Replace-and-match:** The basic principle of this strategy is to replace the human subject with a phantom that simulates (human) tissue as closely as possible and to match the coil load to the load obtained previously in vivo. Then, a calibration measurement is performed, which is identical with respect

to all image settings (eg, pulse sequence and size and position of the VOI). The phantom usually contains a solution that mimics the electric conductivity of human tissue. A more detailed description of the existing absolute quantification methods and references to the main publications can be found in [Jansen et al., 2006].

#### 3.3.1.2 Metabolite ratios

Because of the difficulties in calibrating in vivo spectra to obtain absolute metabolite concentrations, quantification results are usually expressed as ratios, e.g., the widely used Choline-over-NAA ratio in brain tumor analysis. Metabolite levels are expressed relative to a "reference metabolite" from the same spectrum. Metabolite ratios are expressed in arbitrary units. The use of metabolite ratios has the great advantage that it is very easy to implement because it does not require extra imaging time and time-consuming postprocessing. Furthermore, a number of problems—for example, partial volume effects arising from different amounts of cerebrospinal fluid in the selected volumes—can be largely avoided. However, metabolite ratios have a significant limitation: it is not possible to determine whether an abnormal ratio is due to a change in the numerator, in the denominator or both. In addition, ratios may not reflect a change in the concentrations of the metabolites in the case of a comparable reduction (or increase) of both metabolites.

#### 3.3.1.3 Metabolite ratio index

In 2001, McKnight et al. [McKnight et al., 2001] described a new and automated method to find abnormal voxels within an MRSI examination. This method assumes a normally linear relationship between Cho and NAA and that the ratio Cho/NAA is increased with malignancy. Choline is plotted versus NAA for all spectra available in the MRSI dataset and a linear regression line is calculated. The perpendicular distance of a data point to the regression line is then used as a measure of abnormality. Assuming a normal data distribution, 95% of the data points lie within two standard deviations of all perpendicular distances either side of the regression line and are considered to be normal, whereas data points outside two standard deviations are defined as abnormal. Abnormal points are excluded and a new regression line is calculated through the remaining points. This process is repeated until no abnormal points are detected. That is, when all of the re-

maining points meet the criterion for normality (laying within two standard deviations of all perpendicular distances either side of the regression line). These normal points are used as the control population to estimate the normal ratios of Cho/NAA. A Choline-N-acetylaspartate index (CNI) value is assigned to each spectra indicating the number of standard deviations of difference between the amount of Cho and NAA and the mean values of the control spectra. In the preliminary studies [McKnight et al., 2001], a CNI value of 2 was used as the threshold for distinguishing tumor from control tissue. The choice of this threshold was based on results from previous studies as well as on general statistical criteria that assume a Gaussian distribution of variations in the CNI within normal tissue.
This approach can be extended to derive abnormality indices for the relative levels of other metabolites, for example Cr to NAA, or Cho to Cr (CrNI, and CCrI, respectively).
A clear advantage of the CNI method compared to the use of the Cho/NAA ratio is to avoid considering necrotic spectra (whose Cho/NAA ratio can be high because of the reduction of the NAA signal) as areas of cell proliferation while the signal of Choline is not increased compared to a normal spectrum. However, voxels with the same metabolite ratio, can be erroneously identified by this method as belonging to different regions (voxel with higher absolute NAA and Cho intensities is regarded as abnormal, whereas the voxel with lower intensities is regarded as a non-tumour region) (Figure 3.2).
This limitation may reduce the sensitivity in the CNI method. To avoid this behaviour, a novel method called radial CNI (rCNI) has been recently proposed in [Raschke et al., 2014]. This method works in a similar manner to the original CNI method, but instead of using the perpendicular distance from a regression line, the Cho-to-NAA ratio is used as the abnormality measure. Cho-to-NAA distribution is not used directly for tissue characterisation, but the arctan(Cho/NAA) transformation is performed in order to avoid problems in voxels with very low NAA.

### 3.3.2 Pattern Recognition

As mentioned above (Section 3.3.1), quantification is very sensitive to the presence of artifacts in the data and heavily relies on the choice of prior knowledge. Therefore, statistical analysis relying on quantification results inherits all problems associated with the quantification technique considered. In addition, as it has been shown in [Mosconi et al., 2014a], different

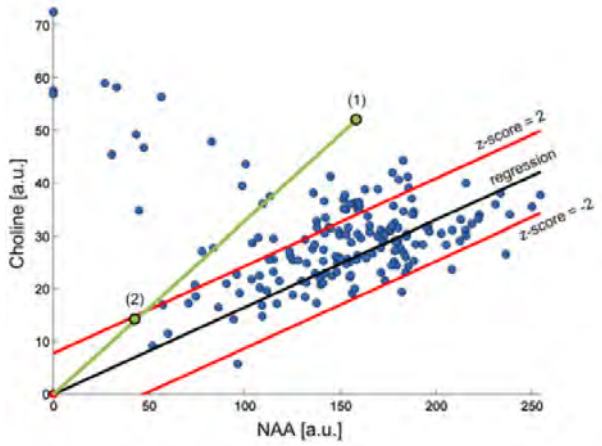


Figure 3.2: The two data points highlighted in green have approximately the same Cho-to-NAA ratio, yet the point with higher metabolite intensities (1) is considered to be abnormal, whereas the other (2) is not. Edited from [Raschke et al., 2014].

quantification algorithms may lead to different results. Therefore, the choice of the quantification method can influence the final result and thus its statistical significance.
Alternatively, pattern recognition (PR) techniques can be used to analyze and simplify the interpretation of MRSI data. PR methods can be differentiated into supervised and unsupervised. Supervised PR methods learn patterns from labelled training data. Unsupervised PR methods discover previously unknown patterns/structures in the data. From the PR point of view, quantification can be used as a feature extraction and dimension reduction technique. However, it is worth mentioning that recent studies [Kelm et al., 2006] show that pattern recognition methods which do not rely on an explicit quantification step can be superior for a given diagnostic problem. In this thesis we explore two different pattern recognition approaches to interpret in vivo MRSI data. Chapter 6 introduces a supervised learning system based on support vector machines (SVM) identify tumor relapse areas using multi-parametric MR data. On the other hand, in Chapter 7, a novel blind source separation method to decompose MRSI signals in tissue-specific spectral patterns is proposed.

## 3.4 Inverse problems and regularization

In this thesis we propose to express different MRSI preprocessing and processing methods as inverse problems and to solve them using regularization techniques.

### 3.4.1 Inverse problems

As in many other real world problems, the MRSI signal is not directly available, but only measured through some physical laws relating the sought signal to the measurements. Let $\boldsymbol{S}$ and $\boldsymbol{Y}$ be the target and observed MRSI signals, respectively. We can express the denoising of MRSI data as the following inverse problem:

$$\boldsymbol{Y} = \boldsymbol{S} + \boldsymbol{N}, \tag{3.1}$$

where $\boldsymbol{Y} \in \mathbb{R}^{M \times R}$ is the data matrix in which each column is a measurement involving $M$ spectral points and $R$ spatial positions, $\boldsymbol{S}$ is the target solution, and $\boldsymbol{N}$ is an additive complex-valued Gaussian noise of covariance matrix $\boldsymbol{\Psi}$ which has to be estimated.

The inverse problem [3.1] can be solved using conventional estimators by minimizing some distance $D$ between the solution and the observation. In this case, the estimation procedure relies on the optimization of the following criterion:

$$\hat{\boldsymbol{S}} = \arg\min_{\boldsymbol{S}} D(\boldsymbol{S}, \boldsymbol{Y}). \tag{3.2}$$

In the case of Gaussian noise, the considered distance is quadratic and the Weighted Least Squares (WLS) estimator is often used in signal/image recovery literature. However, the WLS estimation lacks stability with respect to imprecise or noisy measurements. To alleviate this problem and to find a suitable solution, methods incorporating prior knowledge about the sought solution have been proposed [Eslami and Jacob, 2009a; Nguyen et al., 2010]. In this thesis we propose to exploit prior knowledge about MRSI data using regularization techniques. The additional information is modelled by regularization terms added to the criterion measuring the closeness of the solution to the data [3.2].
In Chapter 4, the inverse problem [3.1] is solved in order to estimate $\boldsymbol{S}$ from

the noisy measurement $\boldsymbol{Y}$, keeping specific features of the data which might be distorted by noise or other experimental conditions.
In Chapter 5, the target solution $\boldsymbol{S}$ is expressed as $\boldsymbol{S} = \boldsymbol{B}\boldsymbol{A}$, where $\boldsymbol{B} \in \mathbb{R}^{M\times K}$ is a matrix in which each column is a metabolite profile, and $\boldsymbol{A} \in \mathbb{R}^{K\times R}$ is the unknown mixing matrix which defines the contribution (abundance) of each metabolite in each spatial position (voxel). Assuming that the matrix $\boldsymbol{B}$ is known, we can estimate $\boldsymbol{A}$ by solving the inverse problem [3.1]. This approach allows us to integrate the denoising strategy proposed in Chapter 4 into a novel quantification procedure.
If both matrices, $\boldsymbol{B}$ and $\boldsymbol{A}$, are assumed to be unknown, the inverse problem [3.1] becomes a blind source separation (BSS) problem. Using this approach, a novel tissue pattern recognition method is proposed in Chapter 7.

### 3.4.2 Regularization in MRI

Different regularization techniques have been proposed in the MRI literature. Prior information about the expected characteristics of the imaged object is introduced in order to preserve the spatial resolution and improve the signal-to-noise ratio of the reconstructed image. Many commonly-used algorithms make use of a quadratic regularization term like the standard Tikhonov regularization [Liang et al., 2002; Ying et al., 2004a; Lin et al., 2004]. This kind of quadratic regularizations improve the reconstructed image quality when the experimental conditions are not too degraded (high magnetic field intensity such as 3T, low noise level,...). However, when it is not the case, these methods can suffer from noise propagation, blurring, ringing or aliasing errors. The research focus during the last years has shifted towards the use of non-quadratic regularization terms in order to maintain edge sharpness such as the total variation (TV) [Liu et al., 2007; Block et al., 2007; Liu et al., 2009]. TV regularization has shown to be well adapted to piecewise smooth images [Liu et al., 2007], but this is not necessarily the case in most of the real MRI images. In addition, it has been shown that use of the TV norm may result in images exhibiting staircase-like artifacts, which are physically implausible in the case of MRI [Chambolle and Pock, 2011]. The connection between $\ell_1$ regularization and sparsity has been found to outperform traditional algorithms and it is recently attracting a lot of attention in MRI [Lustig et al., 2007; Gamper et al., 2008]. However, the great majority of reconstruction algorithms consider a finite-difference sparsifying transform which is formally equivalent to TV regularization and, therefore suffer from

the same limitations. Since 2008, $\ell_1$ wavelet-based regularizations have been introduced in the MRI literature to alleviate this problem [Chaari et al., 2008b; Liu et al., 2008; Guerquin-Kern et al., 2009a].

### 3.4.3 Regularization in MRSI

The role of regularization is to incorporate prior knowledge about the target solution into the problem to be solved. The aim is to constrain the space of possible solutions to stabilize the problem. This is done by prioritizing certain features in the sought solution.
The incorporation of prior knowledge has been exploited by several MRS(I) methods in order to simplify the computational procedure and derive more reliable results. The prior knowledge typically considered is the definition of bounds for some spectral parameters [Vanhamme et al., 1997], the use of parametric spectral models [Diop et al., 1994; Bao and Maudsley, 2007; Nguyen et al., 2010] or the introduction of experimentally measured or simulated spectral profiles [Provencher, 2001; Ratiney et al., 2005; Poullet et al., 2006]. These methods process the signals separately and ignore the spatial context of the MRSI data. More advanced methods exploit not only the spectral but also the spatial context of MRSI signals by incorporating spatial priors [Sava et al., 2011; Kelm et al., 2012].
Regularization techniques promoting spatial smoothness have been used in previous approaches. Spatial smoothness priors are used in [Sava et al., 2011; Kelm et al., 2012] to improve the fitting of MRSI spectra. Both methods encourage spatially smooth variations for some selected spectral parameters. Methods incorporating more than one regularization term to combine both, spatial and spectral priors, are less common. In [Nguyen et al., 2010], a method to denoise MRSI data assuming a particular spectral line-shape and weighted spatial-smoothness is proposed. All these methods incorporating spatial priors rely on spatial smoothness constraints limiting their ability to capture the spatial variations exhibited by in vivo scans, especially in the context of lesions. A less-constrained approach was proposed in [Eslami and Jacob, 2009a], where spatial piecewise smoothness imposed by the spatial total variation (TV) norm is combined with a sparse spectral model. In Kasten et al. [2013], a reconstruction method for MRSI data based on an extension of the TV norm is proposed. Instead of the conventional form of the TV, a method considering higher-order derivatives [Knoll et al., 2011] is considered in order to alleviate the eventual staircase-like artifacts related to the TV.

However, the use of TV-based approaches typically leads to high computational cost due mainly to the estimation of the gradient. Moreover, other limitations of the TV norm in the context of proximal optimization will be described in the next chapter of this manuscript.
In this thesis we propose the use a hybrid regularization scheme to introduce prior knowledge about the different dimension of the MRSI data. Contrary to previous regularization proposed in the context of MRSI, the proposed regularization scheme is based on less restricted assumptions and relies on efficient optimization algorithms.

#### 3.4.3.1 Hybrid regularization

The different processing methods proposed in this thesis are formulated as optimization problems which explore the different dimensions of the data. The prior knowledge on each dimension is expressed as a regularization term introduced in the objective function:

$$\mathcal{J}(\boldsymbol{S}) = \mathcal{D}(\boldsymbol{S}) + \sum_{n=1}^{N} \lambda_n \mathcal{R}^n(\boldsymbol{S}^n), \qquad [3.3]$$

where $\mathcal{J}$ is the objective function to be minimized, $\mathcal{D}(\boldsymbol{S})$ is the data fidelity term which measures the closeness of the target solution $\boldsymbol{S}$ to the measured data, $\mathcal{R}^n$ $(n = 1, ..., N)$ are the regularization terms describing the prior knowledge of each of the dimensions $\boldsymbol{S}^n$ of the data, respectively, and $\lambda_n$ are the regularization parameters which balance the sought solution between the data fidelity term and the constraints imposed by the regularization terms.

#### 3.4.3.2 Regularization in transformed domains

Prior knowledge that might be used to constraint or regularize the sought solution of the problem [3.3] is sometimes better expressed in a transformed domain. For example, it may be desirable to use a data representation where the artifacts decreasing the quality of the signal can be easily detected and hence attenuated. In this respect, the wavelet transform has been shown as a powerful tool that enables a good representation of useful information [Serrai et al., 1997, 2000; Cancino-De-Greiff et al., 2002; Mahmoodabadi et al., 2008].
In this thesis, we propose to express the regularization terms in the wavelet

domain by employing spatial (2D or 3D) and spectral (1D) wavelet decompositions. The optimization problem to be solved can be then be formulated as follows:

$$\mathcal{J}(\boldsymbol{S}) = \mathcal{D}(\boldsymbol{S}) + \sum_{n=1}^{N} \lambda_n \mathcal{R}^n(W_n(\boldsymbol{S}^n)), \qquad [3.4]$$

where $W_n$ is a wavelet operator.

### 3.4.4 Convex Optimization

The regularization schemes proposed in this thesis are based on objective functions that are convex but not necessarily differentiable, which makes impossible the use of standard gradient-based algorithms for minimization. We therefore propose to perform the optimization by using the concept of proximity operators [Moreau, 1962] which was found to be fruitful in a number of recent works in convex optimization [Combettes and Pesquet, 2008; Chaari et al., 2011].
The concept of proximity operator was introduced by Moreau in 1962 [Moreau, 1962] as a generalization of a convex projection operator. In what follows, we recall the definition of a proximity operator.

**Definition 3.4.1.** [Moreau, 1962] *Let $\Gamma_0(\chi)$ be the class of proper lower semicontinous convex functions from a separable real Hilbert space $\chi$ to $]-\infty, +\infty]$ and let $\varphi \in \Gamma_0(\chi)$. For every $x \in \chi$, the function $\varphi + \|\cdot - x\|^2/2$ achieves its infimum at a unique point denoted by $\text{prox}_\varphi x$. The operator $\text{prox}_\varphi : \chi \to \chi$ is the proximity operator of $\varphi$.*

**Example 3.4.1.** When $\varphi$ is the indicator function of a closed convex set $C$, i.e., $\forall x \in \mathbb{R}$,

$$i_C(x) = \begin{cases} 0, & \text{if } x \in C \\ +\infty, & \text{otherwise} \end{cases}$$

$\text{prox}_\varphi$ is the orthogonal projector onto the set.

**Example 3.4.2.** Another example of proximity operator that is extensively used in the signal processing literature is the one associated with the absolute value function $\varphi = \frac{1}{\lambda}|.|^p$, where $p = 1$ and $\lambda > 0$. In this case, the

proximity operator is the well-known soft thresholding operator with $\frac{1}{\lambda}$ as threshold [Donoho and Johnstone, 1994]:

$$\text{prox}_{\frac{1}{\lambda}|.|}x = \text{sign}(x)\max\big(|x| - \frac{1}{\lambda}, 0\big). \qquad [3.5]$$

In the case $p > 1$, the proximity operator of $\varphi = \frac{1}{\lambda}|.|^p$ is given by $\text{prox}_{\frac{1}{\lambda}|.|^p}x = \text{sign}(x)\eta$, where $\eta = \eta^{\text{Re}} + \imath\, \eta^{\text{Im}}$ is the unique solution in $[0, +\infty[$ to $\eta + p\eta^{p-1}\frac{1}{\lambda} = |x|$.
Fig. 3.3 illustrates the curve of the function $\varphi = \frac{1}{\lambda}|.|^p$ for different values of $\lambda$ and $p$. Fig. 3.4 shows the corresponding proximity operators for the same values of $\lambda$ and $p$.

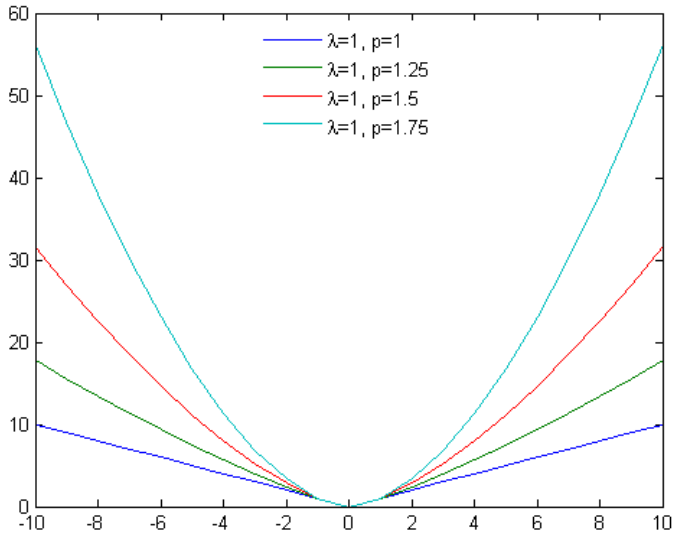


Figure 3.3: Curves of the convex function $\frac{1}{\lambda}|.|^p$ for different values of $\lambda$ and $p$.

Proximity operators have very attractive properties that make them particularly well suited for iterative minimization algorithms [Combettes and Pesquet, 2008]. For instance, $\text{prox}_\varphi$ is firmly non-expansive, i.e.,

$$\forall \boldsymbol{x}, \boldsymbol{y} \in \mathbb{R}^N, \|\text{prox}_\varphi \boldsymbol{x} - \text{prox}_\varphi \boldsymbol{y}\|^2 + \|(\boldsymbol{x} - \text{prox}_\varphi \boldsymbol{x}) - (\boldsymbol{y} - \text{prox}_\varphi \boldsymbol{y})\|^2 \leq \|\boldsymbol{x} - \boldsymbol{y}\|, \qquad [3.6]$$

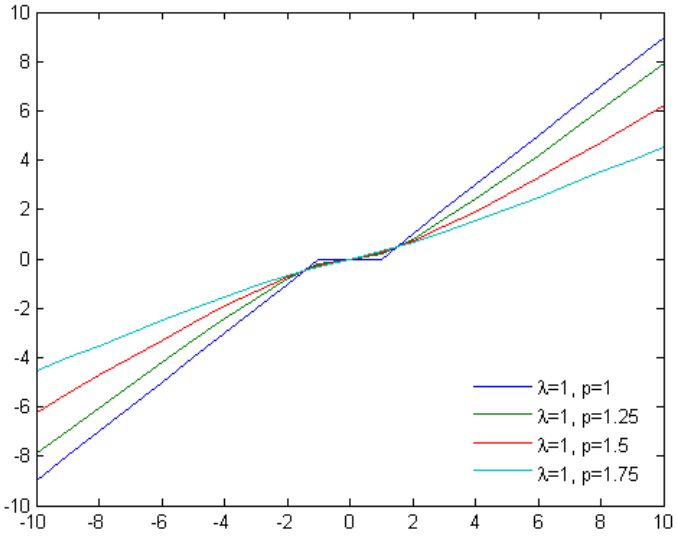


Figure 3.4: Curves of the proximity operators (Eq. [3.5]) associated with the functions shown in Fig. 3.3 for different values of $\lambda$ and $p$.

and its fixed point set is precisely the set of minimizers of $\varphi$. Another interesting property of proximity operators is the separability [Moreau, 1965; Starck et al., 2010]: Let $\{F_i\}_{1\leq i\leq n}$ a family of functions in $\Gamma_0(\chi)$ and $F$ defined on $\chi^n$ with $F(\boldsymbol{x}) = \sum_{f=1}^{N} F_i(\boldsymbol{x}_i)$. Then $\text{prox}_F = \left\{\text{prox}_{F_i}\right\}_{1\leq i\leq n}$. This property implies that the proximal operator of $\frac{1}{\lambda}\|\boldsymbol{x}\|_1$, $\boldsymbol{x} \in \mathbb{R}^N$ , is the soft thresholding operator applied coordinate-wise to each coefficient $\boldsymbol{x}_i$, i.e.,

$$\text{prox}_{\frac{1}{\lambda}\|.\|_1}\boldsymbol{x} = \left[\text{prox}_{\frac{1}{\lambda}|.|}\boldsymbol{x}_1, \text{prox}_{\frac{1}{\lambda}|.|}\boldsymbol{x}_2, ..., \text{prox}_{\frac{1}{\lambda}|.|}\boldsymbol{x}_N\right]^t. \qquad [3.7]$$

The separability of the terms gives us the ability to evaluate the proximal operator in parallel. The interested reader can find many other useful properties and closed-form expressions of the proximity operators of various functions in [Combettes and Pesquet, 2008].

## 3.5 Conclusion

This chapter described the main techniques to process MRSI data. The concept of inverse problem is introduced and exploited to express different MRSI

processing methods. Since the proposed inverse problems are ill-posed, we propose to exploit prior knowledge about the sought solutions using regularization techniques. The regularization schemes used are based on objective functions that are convex but not necessarily differentiable, which makes impossible the use of standard gradient-based algorithms for optimization. The concept of proximity operators is therefore introduced to solve the inherent optimization problem.

# Chapter 4

# MRSI denoising

## Contents



## 4.1 Introduction

Single Voxel Spectroscopy (SVS) techniques identifying abnormal levels of various metabolites have been used for diagnosis purposes for many years and in a variety of illnesses. More recently, much more interest has been developed to acquire multi-voxel spectroscopic images (MRSI) which allow the generation of "metabolic maps" showing the variation in metabolite concentrations over a body volume [Kounelakis et al., 2009]. Unfortunately, this spatial information comes at the cost of a reduced SNR, due to a reduced scan time for each voxel. For typical MRSI acquisition conditions, the noise level is often similar in magnitude to some metabolite signal levels as shown in Fig. 4.1. Noise is thereby a limiting factor in determining metabolite signal amplitude and makes accurate quantification of metabolite signals extremely challenging. Therefore, improving the SNR is a key factor in achieving clinical utility for the MRSI technique.
The SNR can be increased using higher magnetic field strengths. However, the implementation of MRSI at high fields (7 Tesla and beyond) is still challenging due to technical limitations that may reduce the expected SNR, such as increased field inhomogeneity [Boer et al., 2012]. In fact, currently, clinical manufacturers do not support field strength higher than 3 Tesla. Signal averaging is a widely used technique to improve SNR at acquisition time. However, this approach is not feasible because of long acquisition times.

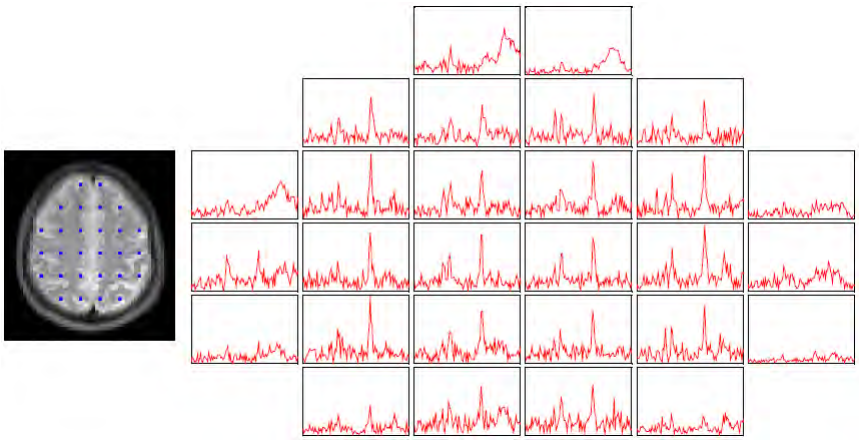

Figure 4.1: Water-suppressed MRSI spectra acquired in a 2D MRSI acquisition from the brain of a healthy human. Edited from [Eslami and Jacob, 2009b]

Moreover, physiological motion may lead to destructive averaging due to variations in signal phase and frequency.
Methods to increase the SNR at the processing level (after acquisition) have also been proposed. A popular method to improve SNR by noise suppression is to apply apodizing filters, but this approach always compromises the spectral resolution of the data [Kim et al., 2012]. Another popular method to denoise MRS signals is to apply wavelet shrinkage [Cancino-De-Greiff et al., 2002]. In another work proposed in [Ahmed, 2005], MRS signals are denoised by consecutive projection onto different domains, represented by a set of linear time-frequency transforms. However, none of these methods explore the spatial properties of the MRSI signals that are processed separately (voxel-wise).
Methods incorporating constraints on the spectral profile, either by using explicit parametric models or by assuming particular line-shape characteristics have also been used for denoising MRSI data [Diop et al., 1994; Bao and Maudsley, 2007; Nguyen et al., 2010]. These approaches tend to bias the interpretation of the measured signal towards the prior assumptions. For example, the method described in [Diop et al., 1994] makes strict use of the Lorentzian lineshape of the spectral peaks which might be too limited to describe the disturbed lineshapes, often presented by in vivo MRSI signals, due to magnetic field inhomogeneities or tissue heterogeneities. In addition,

most of these methods rely heavily on spatial smoothness constraints limiting their ability to capture the spatial variations exhibited by in vivo scans, especially in the context of lesions. As a consequence, they are often ineffective in practical applications [Laruelo et al., 2013a].
A less-constrained approach was proposed in [Eslami and Jacob, 2009a], where spatial piecewise smoothness imposed by the spatial TV norm is combined with a sparse spectral model. In order to alleviate the staircase effect related to the conventional TV, a reconstruction method for MRSI data based on an extension of the TV norm is proposed in Kasten et al. [2013]. In this work, a method considering higher-order derivatives, referred to as the total generalized variation of second order [Knoll et al., 2011] is adopted. However, the use of TV-based methods leads to high computational cost due to the estimation of the gradient. Moreover, it prevents the use of the efficient proximal optimization algorithms, due to the lack of a closed form for the proximity operator of the TV (except if TV is combined with some suitable linear operator to decompose it [Chaari, 2010; Combettes and Pesquet, 2011]). In such context, the TV norm would need an additional inner optimization step to evaluate its proximal operator [Boyer et al., 2012]. A detailed review of regularized reconstruction approaches for MRSI is provided in [Kasten et al., 2015].
It is then desirable to have a method able to suppress noise in MRSI signals in a non-constrained way while preserving the spectral and the spatial features. Since there might be applications where prior information can be reliably incorporated, such a method should also allow natural extensions that preserve this possibility.
In this chapter, we investigate a spatio-spectral sparse regularization to address the limitations mentioned above. We propose a novel method for MRSI denoising, which accounts for signal regularity across the spectral dimension without altering the spectral resolution, but also across the spatial dimension. The proposed approach relies on sparsity promoting priors using wavelet transforms, a key tool that has been successfully used in a wide spectrum of image processing applications, especially in the biomedical field [Pizurica et al., 2006; Chaari et al., 2011]. MRSI data might not be strictly sparse with respect to the $\ell_0$ pseudo-norm due to the typically low spatial resolution of these type of data. In fact, most commonly encountered signals are not strictly sparse in any domain, so that the notion of real sparsity is hard to find in practice. However, we aim to exploit the fact that MRSI data can be represented using only a few dominating coefficients in the wavelet

domain leading to a low $\ell_1$ norm. This is true for both, the spectral and the spatial dimensions of the data. Indeed, the spatio-spectral sparsity of MRSI data have already been successfully used in compressed sensing imaging approaches [Hu et al., 2008; Geethanath et al., 2012].
We use a fast optimization algorithm to deal with the convex optimality criterion which is not differentiable. For doing so, proximal algorithms have been investigated, a family of fast convex optimization algorithms that have also been widely used in signal/image processing [Combettes and Pesquet, 2008; Chaari et al., 2011].

## 4.2 Problem statement

As in many other real world problems, the MRSI signal is not directly available, but only measured through some physical laws relating the sought signal to the measurements. Let $\boldsymbol{S}$ and $\boldsymbol{Y}$ be the target and observed MRSI signals, respectively. We can express the denoising problem as the following inverse problem:

$$\boldsymbol{Y} = \boldsymbol{S} + \boldsymbol{N}, \qquad [4.1]$$

where $\boldsymbol{N}$ is an additive complex-valued Gaussian noise of covariance matrix $\boldsymbol{\Psi}$ which has to be estimated.
The goal is to compute $\boldsymbol{S}$ from the inverse problem [4.1] keeping specific features of the data which might be distorted by the noise.

## 4.3 Spatio-spectral denoising

### 4.3.1 Motivation

Existing methods recover $\boldsymbol{S}$ from the inverse problem [4.1] either by using general schemes where the inherent spectro-spatial dimensions of the MRSI data are not explored, or by assuming restrictive models that are not able to deal with the variability of in vivo data. These are some of the drawbacks of the current methods, like the widely used linear-shift invariant filters, the standard wavelet shrinkage or the method presented in [Nguyen et al., 2010].
We propose to estimate $\boldsymbol{S}$ from Eq. [4.1] by adopting a sparse spatio-spectral regularization scheme that is less constrained than the previous approaches.

The proposed scheme is able to capture the spatio-spectral nature of MRSI data and keeps opened the feasibility of incorporating prior knowledge into the model. The presented method overcomes the limitations of the previous methods by removing the spurious spatio-spectral irregularities while preserving the spatial and spectral resolutions. In addition, unlike the existing regularization schemes, this method relies on an efficient fast optimization algorithm and it is not subject to local optima. The proposed algorithm also presents interesting parallelization properties that could be exploited for big data processing problems.

### 4.3.2 Regularization

#### 4.3.2.1 Spatio-spectral representation of an MRSI dataset

A 3D MRSI dataset (see Fig. 4.2) can be represented as a multidimensional matrix of size $N_r \times N_c \times N_s \times M$, where $N_r$, $N_c$ and $N_s$ are the spatial dimensions and $M$ is the number of spectral points (typically 512 or 1024). Let $\boldsymbol{S}$ be the MRSI signals corresponding to a 2D slice involving $R = N_r \times N_c$ spatial positions and $M$ spectral points. Denoting the 2D spatial position by $r$, $\boldsymbol{S}$ can be written as $\boldsymbol{S} = (\boldsymbol{s}^r)_{r=1,\dots,R} = (\boldsymbol{s}^f)_{1\leq f\leq M}$, where the $M \times 1$ vector $\boldsymbol{s}^r$ denotes the spectrum at voxel $r$, and $\boldsymbol{s}^f$ the 2D image of size $N_r \times N_c$ related to frequency $f$.
At a given spectral frequency $f$, the 2D complex-valued image $\boldsymbol{s}^f$ of size $N_r \times N_c$ can be seen as an element of the Euclidean space $\mathbb{C}^K$ with $K = N_r \times N_c$ endowed with the standard inner product $\langle \cdot \,|\, \cdot \rangle$ and norm $\|\cdot\|$. On the other hand, the spectrum $\boldsymbol{s}^r$ of size $M$ at spatial position $r$ can be seen as an element of the Euclidean space $\mathbb{C}^M$ endowed with the standard inner product and norm.

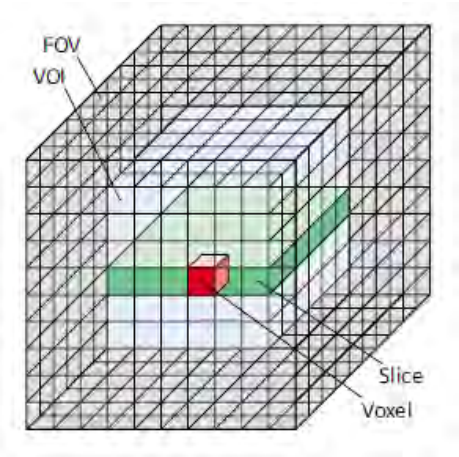


Figure 4.2: Schematic representation of an MRSI dataset. Edited from [Siemens, 2005].

#### 4.3.2.2 Spatio-spectral representation of an MRSI dataset in the wavelet domain

We employ a dyadic 2D orthonormal wavelet decomposition operator $T$ over $j^1_{\max}$ resolution levels. The coefficient field resulting from the wavelet decomposition of an image $\boldsymbol{s}^f$ is defined as $\zeta^f = \left(\boldsymbol{\zeta}^f_a, (\boldsymbol{\zeta}^f_{o,j})_{o\in\mathbb{O},1\leq j\leq j^1_{\max}}\right)$ with $o \in \mathbb{O} = \{0,1\}^2\backslash\{(0,0)\}$, $\boldsymbol{\zeta}^f_a = (\zeta^f_{a,k})_{1\leq k\leq K_{j_{\max}}}$ and $\boldsymbol{\zeta}^f_{o,j} = (\zeta^f_{o,j,k})_{1\leq k\leq K_j}$ where $K_j = K2^{-2j}$ is the number of wavelet coefficients in a given subband at resolution $j$ (by assuming that $N_r$ and $N_c$ are multiples of $2^{j_{\max}}$). Adopting such a notation, the wavelet coefficients have been reindexed so that $\boldsymbol{\zeta}^f_a$ denotes the approximation coefficient vector at the resolution level $j_{\max}$, while $\boldsymbol{\zeta}^f_{o,j}$ denotes the detail coefficient vector at the orientation $o$ and resolution level $j$.
Let be $F$ a dyadic 1D orthonormal wavelet decomposition operator over $j^2_{\max}$ resolution levels. The coefficient field corresponding to the spectrum $\boldsymbol{s}^r$ is then denoted by $\zeta^r = \left(\boldsymbol{\zeta}^r_a, (\boldsymbol{\zeta}^r_{d,j})_{1\leq j\leq j^2_{\max}}\right)$, where the subscripts $a$ and $d$ denote approximation and detail subbands, respectively.

#### 4.3.2.3 Regularization terms

In order to reduce the search space of $\boldsymbol{S}$ to solutions having fewer irregularities both in the spatial and spectral dimensions, we propose here to introduce two regularization terms. The first one describes the 2D spatial prior knowledge about the wavelet coefficients of the target solution. This first regularization term is defined as:

$$R^{spat}(\boldsymbol{S}) = \sum_{f=1}^{M} \Bigg[ \sum_{k=1}^{K_{j^1_{\max}}} \Phi^p_{\mu_a,\alpha_a}\Big((T\boldsymbol{s}^f)_{a,k}\Big) + \sum_{o\in\mathbb{O}} \sum_{j=1}^{j^1_{\max}} \sum_{k=1}^{K_j} \Phi^p_{\mu^j_o,\alpha^j_o}\Big((T\boldsymbol{s}^f)_{o,j,k}\Big)\Bigg], \quad [4.2]$$

where $\forall \xi \in \mathbb{C}$, $\Phi^p_{\mu,\alpha}(\xi) = \alpha|\xi-\mu|^p_p$, $\mu^j_o \in \mathbb{C}$, $\alpha^j_o \in \mathbb{R}_+$ and $p \geq 1$ (similarly $\mu_a$ and $\alpha_a$). Due to the shape parameter $p$, this regularization term keeps a compromise between sparsity ($p \sim 1$) and smoothness ($p \sim 2$) of the wavelet coefficients.

The spectral regularization term allows us to reduce high spectral discontinuities (especially close to the metabolite peaks) between adjacent frequency bands at a voxel $r$. This regularization is made through the penalization of the wavelet coefficients of the 1D spectra $\boldsymbol{s}^r$:

$$R^{spect}(\boldsymbol{S}) = \sum_{r\in R} \Bigg[ \sum_{k=1}^{K_{j^2_{\max}}} \Phi^\beta_{\eta_a,\lambda_a}\Big((F\boldsymbol{s}^r)_{a,k}\Big) + \sum_{j=1}^{j^2_{\max}} \sum_{k=1}^{K_j} \Phi^\beta_{\eta^j_d,\lambda^j_d}\Big((F\boldsymbol{s}^r)_{d,j,k}\Big)\Bigg], \quad [4.3]$$

where $\eta^j_d \in \mathbb{C}$, $\lambda^j_d \in \mathbb{R}_+$ and $\beta \geq 1$ (similarly for $\eta_a$ and $\lambda_a$).

Note that this kind of $\ell_\beta$ with $\beta \geq 1$ regularization has already been successfully used in sparse MRI reconstruction [Chaari et al., 2008a].

### 4.3.3 Optimization procedure

Based on the formulation above, the criterion to be minimized can be written as follows:

$$\mathcal{J}(\boldsymbol{S}) = \mathcal{D}(\boldsymbol{S}) + R^{spat}(\boldsymbol{S}) + R^{spect}(\boldsymbol{S}), \quad [4.4]$$

where $\mathcal{D}(\boldsymbol{S}) = \|\boldsymbol{Y} - \boldsymbol{S}\|^2_{\boldsymbol{\Psi}^{-1}}$ represents the data fidelity term. Since $\mathcal{J}$ is convex, the convergency to a global optimum is guaranteed. However, $\mathcal{J}$ is not necessarily differentiable, which makes impossible the use of gradient-based algorithms for minimization. We therefore propose to perform the minimization of Eq. [4.4] by using the concept of proximity operators [Moreau, 1962] introduced in Chapter 3 (see Definition 3.4.1) which has been used in a number of recent works in convex optimization [Combettes and Pesquet, 2008; Chaari et al., 2011].

In this work, as the observed data are complex-valued, the definition of proximity operator is extended to a class of convex functions defined for complex-valued variables. For the function

$$\begin{aligned} \Phi : \mathbb{C}^R &\rightarrow ]-\infty, +\infty] \\ x &\mapsto \phi^{\mathrm{Re}}[\mathrm{Re}(x)] + \phi^{\mathrm{Im}}[\mathrm{Im}(x)], \end{aligned} \quad [4.5]$$

where $\phi^{\mathrm{Re}}$ and $\phi^{\mathrm{Im}}$ are functions in $\Gamma_0(\mathbb{R}^R)$ and $\mathrm{Re}(x)$ (respectively $\mathrm{Im}(x)$) is the vector of the real parts (respectively imaginary parts) of the component of $x \in \mathbb{C}^R$, the proximity operator is defined as

$$\begin{aligned} \mathrm{prox}_{\Phi} : \mathbb{C}^R &\rightarrow \mathbb{C}^R \\ x &\mapsto \mathrm{prox}_{\Phi^{\mathrm{Re}}}[\mathrm{Re}(x)] + \mathrm{prox}_{\Phi^{\mathrm{Im}}}[\mathrm{Im}(x)]. \end{aligned} \quad [4.6]$$

An example of proximity operator for a function of a complex-valued variable is given below.

**Example 4.3.1.** As shown in Chapter 3 (see Example 3.4.2), the proximity operator of the absolute value function $\Phi = \frac{1}{\lambda}|x|$, where $x, \lambda \in \mathbb{R}$ and $\lambda > 0$ is the well-known soft thresholding operator with $\frac{1}{\lambda}$ as threshold [Donoho and Johnstone, 1994]:

$$\mathrm{prox}_{\frac{1}{\lambda}|.|}x = \mathrm{sign}(x)\max\big(|x| - \frac{1}{\lambda}, 0\big). \quad [4.7]$$

In the case of convex functions defined for complex-valued variables, $x, \lambda \in \mathbb{C}$, the proximity operator is expressed as follows:

$$\begin{aligned}\text{prox}_{\frac{1}{\lambda}|.|}x = \text{sign}(\text{Re}\Big(x\Big)\Big) \max\{|\text{Re}(x)| - \text{Re}(\lambda), 0\} \\ + \imath \, \text{sign}\Big(\text{Im}(x)\Big)\Big) \max\{|\text{Im}(x)| - \text{Im}(\lambda), 0\}. \quad [4.8]\end{aligned}$$

Since the cost function in Eq. [4.4] is made up of more than two non-necessarily differentiable terms, an appropriate solution for its minimization is the Parallel Proximal Algorithm [Combettes and Pesquet, 2008] which is designed to minimize the sum of a finite number of convex functions. This algorithm requires the knowledge of the proximity operators of the functions involved in the optimization criterion. In our case, we have a sum of three convex functions: the data fidelity term, $\mathcal{D}$, and the two penalizations, $R^{spat}$ and $R^{spect}$. The expressions of the proximity operators of these functions and the details of the minimization algorithm are described below.

#### 4.3.3.1 Proximity operator of the data fidelity term

According to standard rules about the calculation of proximity operators [Combettes and Pesquet, 2008, Table 1.1], the proximity operator of the data fidelity term $\mathcal{D}$ is given by:

$$\text{prox}_{\mathcal{D}}\boldsymbol{S} = \left(\boldsymbol{I}_d + 2\boldsymbol{\Psi}^{-1}\right)^{-1}\left(\boldsymbol{S} + 2\boldsymbol{\Psi}^{-1}\boldsymbol{Y}\right), \quad [4.9]$$

where $\boldsymbol{I}_d$ is the identity operator.

#### 4.3.3.2 Proximity operator for the regularization terms

Using the same rules as in Section 4.3.3.1, the proximity operator of $\Phi^p_{\mu,\alpha}$ for every $\xi \in \mathbb{C}$ is given by $\text{prox}_{\Phi^p_{\mu,\alpha}}\xi = \text{sign}(\xi)\eta$, where $\eta = \eta^{\text{Re}} + \imath\, \eta^{\text{Im}}$ is the unique solution in $\mathbb{C}_+$ to $\eta + p\eta^{p-1}\alpha = |\xi - \mu|$. If $p = 1$, this proximity operator simplifies as follows:

$$\begin{aligned}\text{prox}_{\Phi^p_{\mu,\alpha}}\xi = \text{sign}(\text{Re}\Big(\xi - \mu\Big)\Big) \max\{|\text{Re}(\xi - \mu)| - \text{Re}(\alpha), 0\} \\ + \imath \, \text{sign}\Big(\text{Im}(\xi - \mu)\Big)\Big) \max\{|\text{Im}(\xi - \mu)| - \text{Im}(\alpha), 0\}. \quad [4.10]\end{aligned}$$

However, due to the presence of the wavelet operators in both the spatial and the spectral regularization terms (Eqs. [4.2] and [4.3]), we need to calculate the proximity operators of $\Phi^p_{\mu,\alpha} \circ T$ and $\Phi^\beta_{\eta,\lambda} \circ F$, respectively. Since $T$ and $F$ are both orthonormal wavelet decomposition operators, we have $TT^* = \mathrm{Id}$ and $FF^* = \mathrm{Id}$, where $T^*$ and $F^*$ are the adjoint wavelet operators of $T$ and $F$, respectively, and Id is the identity operator. Therefore the proximity operators of the regularization terms can be calculated based on [Combettes and Pesquet, 2008, Lemma 2.4], leading to $\mathrm{prox}_{\Phi^p_{\mu,\alpha} \circ T} = \mathrm{Id} + T^* \circ (\mathrm{prox}_{\Phi^p_{\mu,\alpha}} - \mathrm{Id}) \circ T$ (similarly for $\mathrm{prox}_{\Phi^\beta_{\eta,\lambda} \circ F}$).

#### 4.3.3.3 Optimization algorithm

A minimizer of the criterion [4.4] can be iteratively computed according to Algorithm 1. This algorithm is based on the extension to the complex case of the Parallel Proximal Algorithm (PPXA) [Combettes and Pesquet, 2008] which is designed to minimize the sum of a finite number of convex functions $f_1, ..., f_m$. At each iteration $n$, this algorithm requires the knowledge of $(\mathrm{prox}_{\frac{\gamma}{\omega_i} f_i})_{i=1,...,m}$, where $\gamma$ corresponds to a step-size parameter and the weights $\omega_i$ measure the contribution of each function in the criterion [4.4]. The fact that the algorithm involves several parameters ($\gamma$, $(\omega_i)_{1 \leq i \leq m}$, and relaxation parameter $\lambda$) should not be viewed as a weakness since the convergence is guaranteed for any choice of these parameters under some assumptions [Combettes and Pesquet, 2008]. In fact, these parameters bring flexibility to PPXA in the sense that an appropriate choice of them may be beneficial to the convergence speed [Pustelnik et al., 2011]. Typical values for these parameters are indicated in [Pustelnik et al., 2011] in Section 5.2. In our case, Algorithm 1 is implemented by setting $\gamma = 10$, $\omega_i = 1/3$ (equal contributions to the three functions in [4.4]) and $\lambda = 1.6$. A key advantage of PPXA is its parallel structure which makes it easily implementable on multicore architecture while preserving the convergence to the global minimum. The resulting algorithm for the minimization of the optimality criterion in Eq. [4.4] is described below.

**Algorithm 1 Hybrid MRSI denoising**

Set $\gamma > 0$, $\lambda \in ]0, 2[$, $n = 0$, $(\omega_i)_{1 \leq i \leq 3} \in [0,1]^3$ s. t. $\sum_{i=0}^{3} \omega_i = 1$, $\boldsymbol{S}^{(n)} = \sum_{i=1}^{3} \omega_i \boldsymbol{U}_i^{(n)}$, $\boldsymbol{U}_i^{(n)} = (\boldsymbol{s}^r)_{r \in R} = (\boldsymbol{s}^f)_{1 \leq f \leq M} \in (\mathbb{C}^{K \times M})^3$.

1: **repeat**
2: Calculate $p_1^{(n)} = \text{prox}_{\frac{\gamma}{\omega_1} \mathcal{D}} \boldsymbol{S}^{(n)}$.
3: Calculate $p_2^{(n)} = \text{prox}_{\frac{\gamma}{\omega_2} R^{spat}} \boldsymbol{S}^{(n)}$.
4: Calculate $p_3^{(n)} = \text{prox}_{\frac{\gamma}{\omega_3} R^{spect}} \boldsymbol{S}^{(n)}$.
5: Set $P^{(n)} = \sum_{i=1}^{3} \omega_i p_i^{(n)}$.
6: **for** $i = 1$ to $3$ **do**
7: $\boldsymbol{U}_i^{(n)} = \boldsymbol{U}_i^{(n)} + \lambda(2P^{(n)} - \boldsymbol{S}^{(n)} - p_i^{(n)})$ .
8: **end for**
9: $\boldsymbol{S}^{(n+1)} = \boldsymbol{S}^{(n)} + \lambda(P^{(n)} - \boldsymbol{S}^{(n)})$.
10: Set $n \leftarrow n + 1$.
11: **until** Convergence.
12: **return** $\hat{\boldsymbol{S}} = \boldsymbol{S}^{(n)}$.

## 4.4 Results

In order to validate the performance of the proposed algorithm, we carried out a set of experiments on both synthetic and real data. The main goal of this validation is to show the ability of the algorithm to increase the SNR of MRSI data while preserving spatial and spectral features. Another important objective is to demonstrate the flexibility of the algorithm to deal with the variations exhibited by in vivo data.

### 4.4.1 Synthetic Data

To show the performance of the proposed method, we carried out a set of experiments on synthetic data. We simulate $^1$H MRSI data based on values commonly reported in the literature [Govindaraju et al., 2000] and experimental data. We consider four MR-observable metabolites in human brain: N-acetylaspartate (NAA), creatine (Cr), choline (Cho) and lactate (Lac). For each metabolite, a spectral profile was obtained from quantum mechanical simulations of a spin-echo MR experiment using the jMRUI software pack-

age [Stefan et al., 2009]. Different levels of additive white Gaussian noise were added to the ground truth signal Figure 4.3). The standard deviation ($\sigma$) of the different levels of noise were selected in accordance to values from in vivo scans.

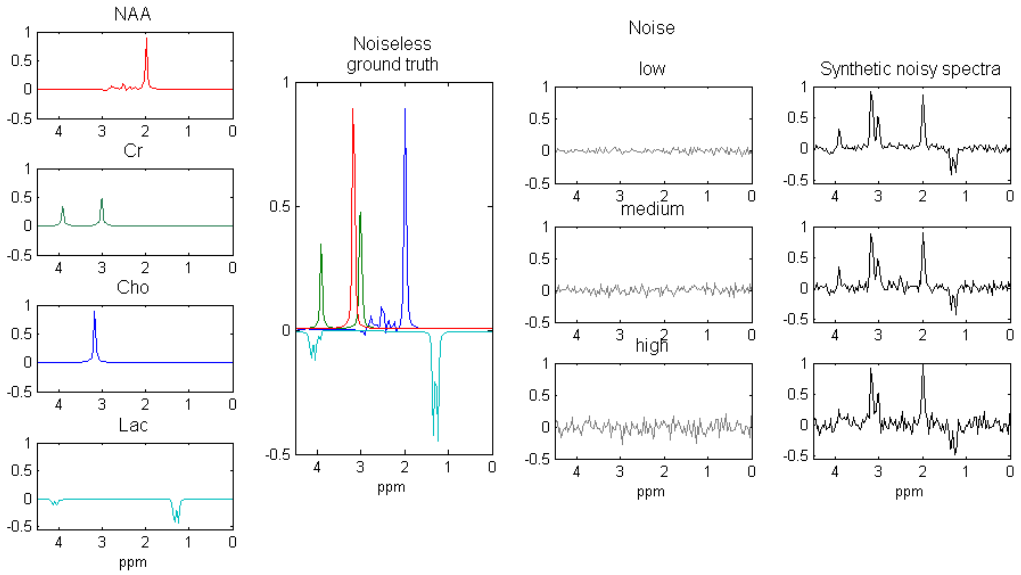


Figure 4.3: Simulation of synthetic MRSI spectra from simulated metabolite profiles.

Two synthetic MRSI datasets presenting different geometries were generated: a dataset with a sharp edge separating tumor-like and normal appearing regions, and another dataset with a smooth edge between both regions (Figure 4.4). The objective is to measure the gain in SNR and to test if the proposed method is able to preserve both the spectral and the spatial features.
In addition, we compare the proposed spatio-spectral regularization (SSR) with conventional apodization (Apod), with spatial 2D wavelet shrinkage (2D-WS) and with the method incorporating spatial-smoothness and autoregressive spectral constraints (SSAC) proposed in [Nguyen et al., 2010]. Apodization refers to the processing technique by which the FID is multiplied pointwise by some appropriate function/filter in order to improve the SNR of the signal. This technique is typically used for MR signals to avoid the spurious peaks that are present in the spectrum when the FID has not

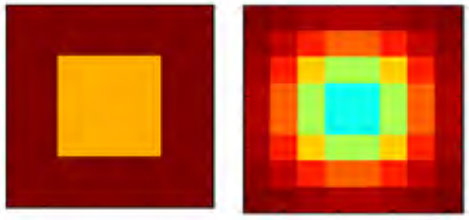

Figure 4.4: Spatial distributions of the synthetic MRSI datasets presenting different geometries: a sharp edge separating different regions (left), and a smooth edge between both regions (right).

decayed completely by the end of the acquisition. In order to avoid this artifact, the signal can be forced to decay more rapidly using an apodization filter. Here we have considered the Hanning function (centered in 0 ms, width 256 ms), one of the most popular apodization filters for MRS signals. For the 2D wavelet shrinkage we have used a Matlab implementation using the the Donoho-Johnstone universal threshold approach [Donoho and Johnstone, 1994]. In SSAC, the spatial and spectral regularization parameters have been chosen so as to optimize the output SNR, while preserving at best the spectral features, especially lineshapes. The SNR in dB of each signal, $\boldsymbol{Y}$, was computed in the frequency domain as $\mathrm{SNR} = 20\log_{10}\frac{\|\boldsymbol{S}_{\mathrm{ref}}\|_2}{\|\boldsymbol{S}_{\mathrm{ref}}-\boldsymbol{Y}\|_2}$, where $\boldsymbol{S}_{\mathrm{ref}}$ denotes the noiseless signal. SSAC is very sensitive to the prediction coefficients and the order of the Autoregressive (AR) model that defines the spectral regularization term. We have chosen here an order $L = 5$ to capture the mean peaks present in the simulated spectra. Linear prediction coefficients were estimated using a least squares method. The same compromise has been applied to tune the regularization parameters in our method (SSR) (see Section 4.3.2.3) for $p = 1$ in Equation [4.2] and $\beta = 1$ in Equation [4.3]. It is worth noticing that fully autocalibrated approaches may be used to automatically estimate these parameters directly from the data [Chaari et al., 2010]. Note that only wavelet detail coefficients were processed. This is equivalent to setting the regularization parameters to zero for the approximation coefficients (i.e., $\alpha_a = 0$ in Eq. [4.2] and $\lambda_a = 0$ in Eq. [4.3]). The parameters $\mu_o$ and $\eta_d$ (in Equations [4.2] and [4.3]) were also set to zero. In order to show an example on how the regularization parameters are selected for the proposed method, Figure 4.5 shows the variation of the SNR as a function of the spectral and spatial parameters for a given MRSI dataset. As it can be seen in the figure, the highest SNR is reached when the spa-

tial regularization parameter is around 0.05 and the spectral regularization parameter takes any of the following values: 0.01, 0.05 or 0.1. In case that different combinations of regularization parameters provide the same (or very similar) SNR, as in this example, we select the smallest parameter value in order to preserve the spatial and spectral features. Therefore, in the example provided we would set the spatial regularization parameter to 0.05 and the spectral parameter to 0.01.

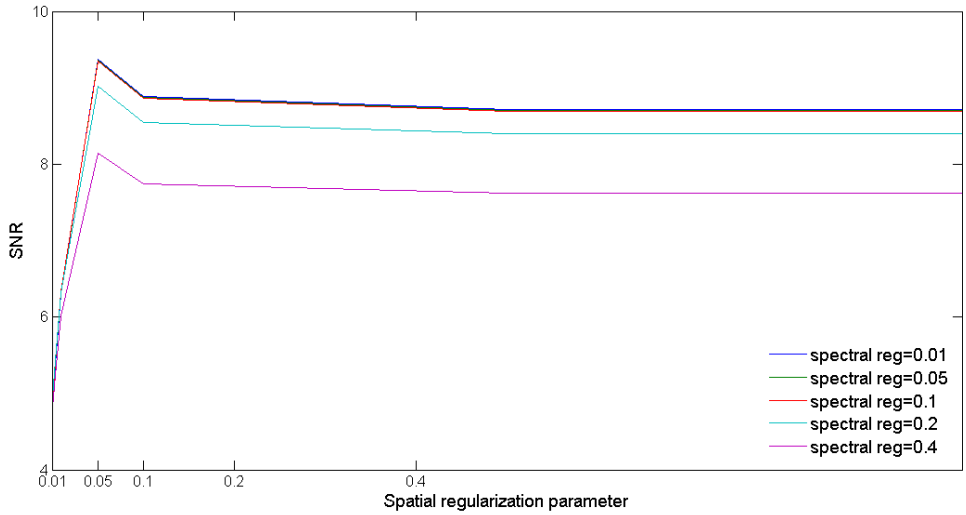


Figure 4.5: SNR of a given MRSI dataset as a function of the spatial and spectral parameters ($\alpha_o$ in Eq. [4.2] and $\lambda_d$ in Eq. [4.3]).

As regards the wavelet transforms (operators $T$ and $F$ in Equations [4.2] and [4.3], respectively), we used a Daubechies basis over one resolution level. The use of Daubechies wavelets is supported by the fact that this wavelet family has already shown to be well suited for MRS(I) data in previous works [Ahmed, 2005; Hu et al., 2008; Geethanath et al., 2012]. The property that distinguishes Daubechies wavelets is that they have minimum local support for any given number of vanishing moments. This trade-off between length of the support and vanishing moments makes the Daubechies family well suited to represent (compress) signals that have few singularities and that are smooth between singularities (as it is normally the case for clinical long/medium TE MRSI data). Indeed, the shorter the wavelet support the less wavelets interacting with each singularity (i. e., fewer wavelet coefficients are needed to describe a spectral peak). Generally speaking, a smaller sup-

port implies less computation and more vanishing moments implies better compression (better representation) of the signal.
In addition, we have explored various wavelet families, including Daubechies, Symlets and Coiflets using synthetic MRSI data. The synthetic dataset with a smoother border between lesion and normal regions was considered for this analysis since it seems to be more realistic than the extreme case represented by the sharp dataset(Figure 4.4). Synthetic datasets at three different levels of noise were generated (Figure 4.3) in order to compare the performance of the different wavelet families. The accuracy of the three wavelets turned out to be very similar, with Daubechies having slightly better SNR results (Table 4.1). Since the efficiency of noise reduction seemed to decrease as the number of Daubechies filter coefficients increased we decided to use db2 (4 filter coefficients). This behaviour has already been reflected in previous works like [Kim et al., 2000].
The reason to use one resolution level is mainly the low spatial resolution of the data. On the other hand, increasing the number of resolution levels increases the number of regularization parameters to be set leading to a more difficult configuration and automation of the algorithm. However, high spatial resolution MRSI images, where the low signal-to-noise ratio is a major limitation, may benefit from the use of different resolution levels.

| | $SNR_{after}$ | | | | |
|---|---|---|---|---|---|
| $SNR_{before}$ | db2 | db4 | db2 | sym2 | coi2 |
| SNR=2 | 6.5 | 6.42 | 6.39 | 6.21 | 6.07 |
| SNR=6 | 11.84 | 11.72 | 11.64 | 11.75 | 11.6 |
| SNR=12 | 16.71 | 16.61 | 16.57 | 16.71 | 16.60 |

Table 4.1: Performance of the proposed denoising method for each of the analyzed wavelet families and for different levels of noise.

We processed the two different synthetic datasets with the different methods at three different levels of noise. The method SSAC could not suppress noise correctly in the metabolite regions (Figure 4.6 (b.1,b.2) and Figure 4.7 (b.1,b.2)). Even if it provides better SNR than the proposed method in some cases (Tables 4.2 and 4.3), the signals in regions close to the metabolite peaks are underestimated as shown in Figures 4.8 and 4.9. Apodization filters provide good SNR but they are known to broaden resonances and distort

spectral lineshapes [Kotyk et al., 1995]. Therefore, this method tend to blur the spatial distribution of the data as shown in Figures 4.8 and 4.9. 2D-WS provides the best SNR values but at the expense of spatial artifacts as it can be seen in the spatial distributions shown in Figure 4.8 and Figure 4.9. The proposed method provides the best trade-off between SNR gain and features preservation.

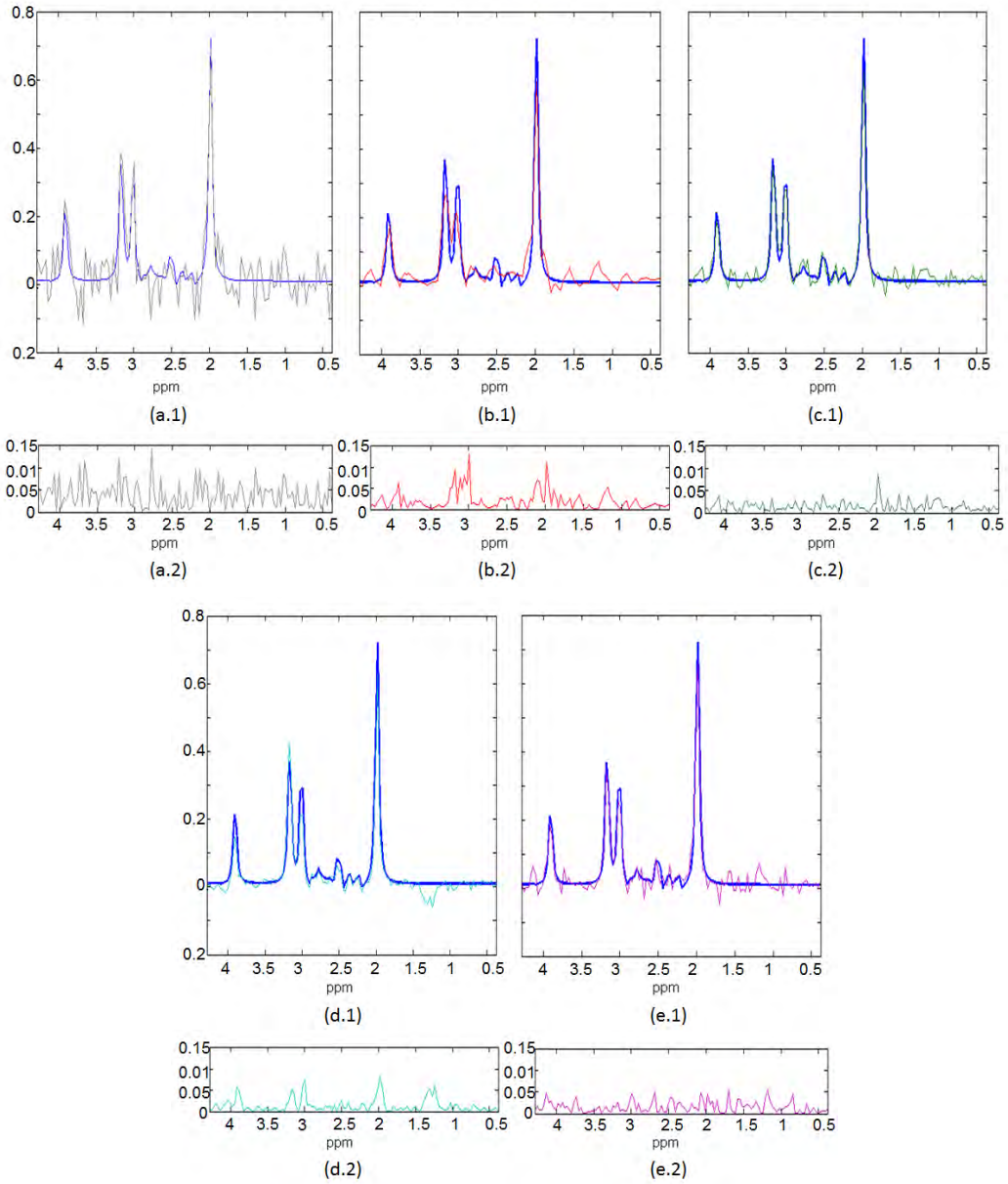


Figure 4.6: Normal appearing spectrum from a particular voxel: (a.1) noisy spectrum; (b.1) spectrum obtained from SSAC; (c.1) spectrum obtained from Hanning apodization; (d.1) spectrum obtained from 2D wavelet shrinkage; (e.1) spectrum obtained from the proposed denoising; (a.2), (b.2), (c.2), (d.2) and (e.2) are the absolute residuals of (a.1), (b.1), (c.1), (d.1) and (e.2), respectively. Ground truth spectrum is shown in blue.

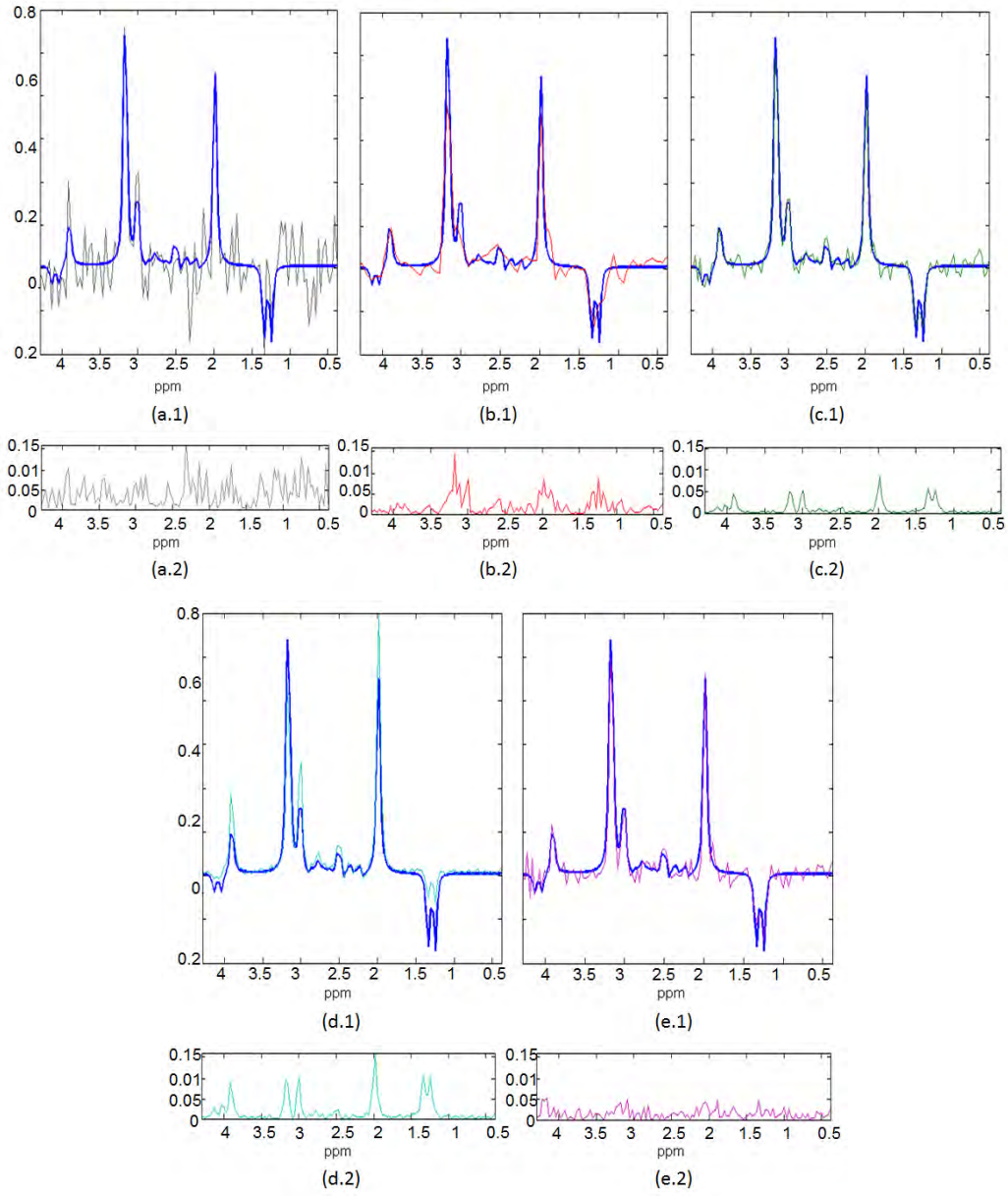


Figure 4.7: Tumor-like spectrum from a particular voxel: (a.1) noisy spectrum; (b.1) spectrum obtained from SSAC; (c.1) spectrum obtained from Hanning apodization; (d.1) spectrum obtained from 2D wavelet shrinkage; (e.1) spectrum obtained from the proposed denoising; (a.2), (b.2), (c.2), (d.2) and (e.2) are the absolute residuals of (a.1), (b.1), (c.1), (d.1) and (e.2), respectively. Ground truth spectrum is shown in blue.

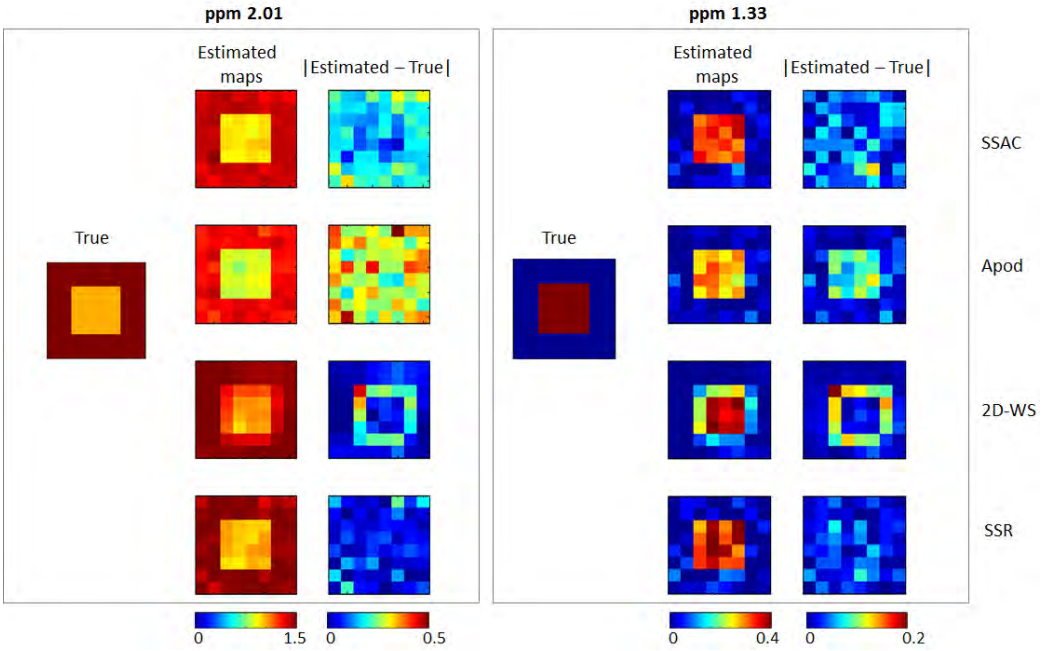


Figure 4.8: Spatial distributions at 2.01 ppm (close to NAA peak) and 1.33 ppm (close to Lac peak) corresponding to the sharp edges dataset of size $8 \times 8$.

| | $\text{SNR}_{\text{after}}$ | | | |
|---|---|---|---|---|
| $\text{SNR}_{\text{before}}$ | SSAC | Apod | 2D-WS | SSR |
| SNR=2 | 5.34 | 6.02 | 7.39 | 6.15 |
| SNR=6 | 9.78 | 12.84 | 12.74 | 10.34 |
| SNR=12 | 14.31 | 17.31 | 16.79 | 13.1 |

Table 4.2: Performance of the compared methods in terms of SNR for the sharp edges dataset.

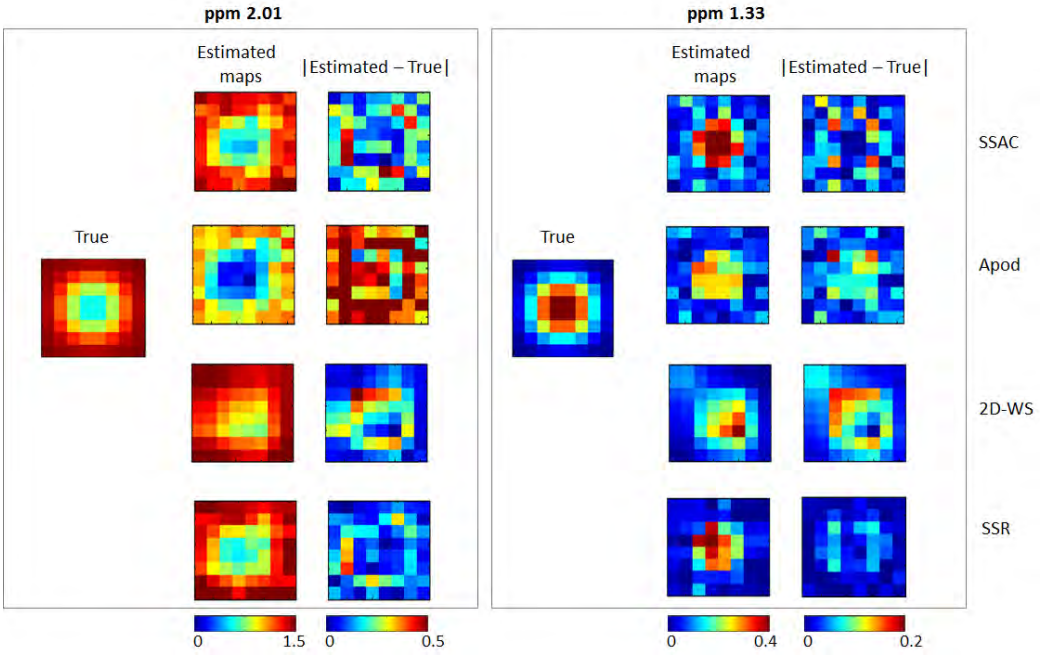


Figure 4.9: Spatial distributions at 2.01 ppm (close to NAA peak) and 1.33 ppm (close to Lac peak) corresponding to the smooth edges dataset of size $8 \times 8$.

| | $SNR_{after}$ | | | |
|---|---|---|---|---|
| $SNR_{before}$ | SSAC | Apod | 2D-WS | SSR |
| SNR=2 | 6.3 | 7.02 | 7.39 | 6.5 |
| SNR=6 | 11.78 | 12.68 | 12.74 | 11.84 |
| SNR=12 | 17.78 | 17.31 | 16.79 | 16.71 |

Table 4.3: Performance of the compared methods in terms of SNR for the smooth edges dataset.

### 4.4.2 In vivo Data

To further analyse the robustness of our method, we have tested the results on in vivo MRSI data from human brain. These data were acquired with a Siemens Avanto 1.5 T using a 3D CSI sequence with water suppression,

TE=135 ms, TR =1500 ms, 512 FID data points and 4 averages. Improvements with SSR, compared to conventional signal apodization, were found on experimental data. By using SSR, the SNR is increased without decreasing spectral resolution, thus maintaining the spectral features. We have also compared the performance of SSAC and SSR on in vivo MRSI signals. SSR has shown to be more robust to noise than SSAC since it is less sensitive to spectral lineshapes. Fig. 4.10 shows a real spectrum (related to abnormal tissue) that has been denoised using both methods. We can easily notice that our approach allows preserving the spectral lineshapes which are underestimated with SSAC. Fig. 4.11 shows how apodization (Hanning filter) distorts spectral lines while they are well preserved after SSR denoising.

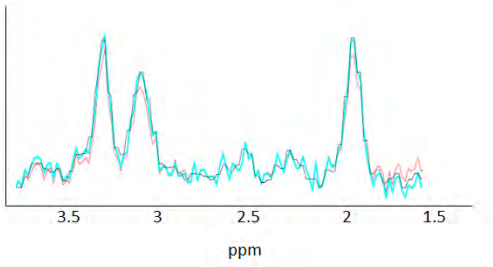


Figure 4.10: Raw in vivo spectrum (blue), spectrum after SSAC denoising (red) and spectrum after SSR denoising (black).

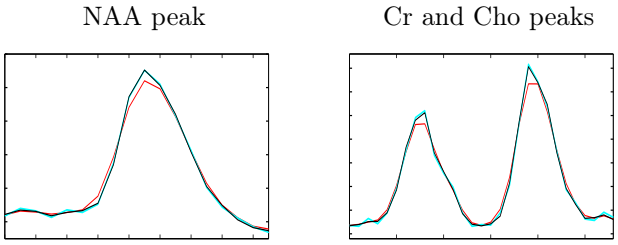


Figure 4.11: Comparison of standard apodization and SSR: raw spectrum (blue), apodized spectrum (red) and spectrum after SSR denoising (black).

In vivo spectra from healthy-appearing tissue were quantified using the method described in [Poullet et al., 2006]. These same spectra were quantified again after being processed using the denoising method described in this chapter. Fig. 4.12 shows boxplots of the distribution of the estimated metabolite

amplitudes ratios in both cases. Values estimated without previous denoising show higher variances than for the other case where previous denoising was applied. This may indicate poorer quantitation accuracy due to the presence of noise. Indeed, according to values commonly reported in the literature [Safriel et al., 2005], the ratios NAA/Cr and Cho/Cr tend to be overestimated in noisy spectra. This behaviour is significantly corrected for all metabolites by reducing the noise in the data before quantification.
Regarding the computational cost, the proposed algorithm is slower than conventional denoising methods (like spectral wavelet shrinkage or apodization filters). This is due to the fact that the proposed spatio-spectral regularization takes into account an additional dimension of the data. Compared to SSAC, the more recent method described in [Nguyen et al., 2010], our method is significantly much faster: less than 50 seconds against few minutes for most of the experiments presented in this chapter. More specifically, the computation times of the proposed algorithm were between 30 and 50 seconds (depending on the size of the MRSI data set and the level of noise), while the computation times for the method in [Nguyen et al., 2010] were always higher than 60 seconds. The experiments were done on a 64-bit 1.8GHz i7-4500U architecture with a Matlab implementation (R2013a).

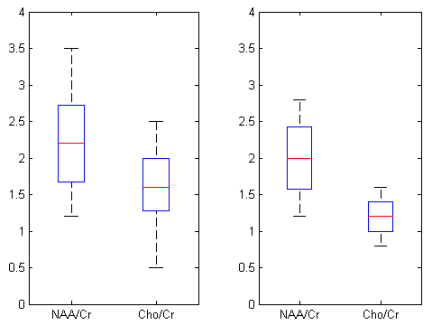


Figure 4.12: Boxplots of the distribution of the relative metabolite amplitudes. Without previous denoising (left), with previous denoising (right).

These results are in accordance with the results presented in our preliminary work [Laruelo et al., 2013b].

## 4.5 Conclusion

We presented a new denoising method for MRSI which overcomes the drawbacks of previous approaches without any lineshape constraint. This property makes our method suitable for handling in vivo data. It explores both spectral and spatial dimensions of MRSI data. The inherent optimization problem is solved using a fast proximal algorithm that allows parallel computations while guaranteeing the convergence to the global minimum. Furthermore, the proposed approach can be easily extended to incorporate more sophisticated priors, such as tissue distributions and anatomical configuration extracted from companion MRI images.

# Chapter 5

# MRSI quantification

## Contents



## 5.1 Introduction

Despite the numerous publications on the subject [Vanhamme et al., 1997; Soher et al., 1998; Provencher, 2001; Ratiney et al., 2005; Poullet et al., 2006; Sava et al., 2011; Kelm et al., 2012], the quantification of MRSI data is still a challenging problem due to the due to the acquisition artifacts (instrumental noise, magnetic field inhomogeneities, body motion) that lead to low signal-to-noise ratio (SNR) of the MRSI signals and overlap of spectral lines. SNR and chemical shift separation of metabolite peaks increase approximately linearly with the increase of the magnetic field. However, considering the relatively weak magnetic fields used in clinical practice, a limited chemical shift dispersion often causes spectral overlap and complicates the separation of metabolites. The difficulty is higher when there are lesions that produce non-characteristic spectra and when nuisance signals, such as poorly suppressed water or lipid signals in $^{1}$H-MRSI, distort the spectra and desirable metabolite signals are almost indistinguishable from noise due to their low concentration. As shown in Chapter 4, improving the SNR is a key factor in achieving robust and accurate quantification of MRSI data. Many quantification methods incorporate techniques to face the low quality of MRSI signals. A common approach to improve the robustness of the quantification of MRSI spectra is the incorporation of prior knowledge for some spectral parameters. For example, AMARES [Vanhamme et al., 1997] allows specify-

ing upper and lower bounds for frequency, damping and phase. It also allows imposing relations (such as differences or ratios) between individual spectral parameters. Simulations as well as in vivo experiments confirm the decrease of the Cramér-Rao lower bounds (CRLB) [Cavassila et al., 2001] when incorporating prior knowledge in the quantification process [Mierisová et al., 1998]. Prior knowledge on the spectral parameters can also be incorporated by making use of experimentally measured (in vitro) or simulated metabolite profiles [Graveron-Demilly et al., 1993; Smith et al., 1994], as implemented in [Provencher, 2001; Ratiney et al., 2005; Poullet et al., 2006]. More recently, some quantification methods have proposed to exploit not only the spectral but also the spatial context of MRSI signals by incorporating spatial priors into the quantification model. An early approach using *a priori* spatial information was introduced by Soher *et al.* [Soher et al., 1998]. In their iterative method, selected parameter estimates are updated at each iteration assuming smoothness of these parameter distributions. The well-known LCModel [Provencher, 2001] also provides a spatial fitting mode for MRSI data. It first analyzes a central voxel and then proceeds in the neighborhood using previously fitted voxels for initialization and soft constraints for new fits.

More recent quantification methods incorporate a penalty term encouraging spatially smooth solutions. In [Kelm et al., 2012], a Bayesian smoothness prior improving the fitting of MRSI data is proposed. This method encourages spatially smooth variations for some selected spectral parameters (frequency, damping and phase). In [Sava et al., 2011], an iterative approach combining the spatial prior proposed in [Kelm et al., 2012] with other methods incorporating spatial information is presented. Spatial smoothing is desirable because it is reasonable to expect that neighbouring pixels will contain similar information. However, it is well known that spatial smoothing tends to blur the images since the edges between different regions may be smoothed out.

In this chapter, we propose a novel quantification technique which benefits from the combination of two strategies, the use of metabolite profiles and the regularization scheme presented in Chapter 4 [Laruelo et al., 2016b]. Spatial and spectral regularization terms are jointly incorporated with the aim of increasing the SNR and exploiting the neighbouring information along the spatial and spectral dimensions for a given MRSI voxel. Contrary to previous quantification methods, the prior knowledge is not imposed directly on selected spectral parameters, but on the representation of the data in

the wavelet domain. The method exploits the fact that the wavelet transform maps white noise in the signal domain to white noise in the transform domain. Thus, while signal energy becomes more concentrated into fewer coefficients in the wavelet domain, noise energy does not. This property enables the efficient separation of signal from noise. A number of wavelet-based techniques, including quantification and denoising, have been previously applied to MR spectroscopy [Serrai et al., 1997, 2000; Cancino-De-Greiff et al., 2002; Zarei et al., 2008]. Fast MR spectroscopic imaging has also been accomplished by the use of wavelets to enable compression in the spectral and spatial domains [Hu et al., 2008; Fu and Serrai, 2011]. To our knowledge, this is the first time that the use of the wavelet properties together with a hybrid regularization able to catch the different nature of the spectral and the spatial dimensions of MRSI data is integrated into the quantification algorithm. This method can be applied in addition to other types of prior knowledge (as upper and lower bounds or smooth spatial variations for some selected spectral parameters). A quantification solution is formulated for the whole MRSI grid. However, in contrast to previous approaches, the presented method is more flexible and less restrictive allowing the preservation of sharp spatial features. In order to simultaneously fit all signals in the MRSI grid while introducing spectral-spatial information, a fast proximal optimization algorithm is proposed to recover the optimal solution.

## 5.2 Regularized quantification

### 5.2.1 Signal model

In vivo magnetic resonance spectroscopy (MRS) signals are measured in the time domain and consist of responses from metabolites (including macromolecules), water and noise. Theoretically, a measured MRS signal at spatial position $r \in \{1, \ldots, R\}$ can be modelled by a sum of $K$ exponentially damped complex sinusoids [Vanhamme et al., 2001] of $M$ time-domain data samples:

$$\boldsymbol{y}^r(m) = \sum_{k=1}^{K} a_k^r \exp(i\boldsymbol{\phi}_k) \exp(-d_k m + 2\pi i f_k m) + \boldsymbol{l}^r(m) + \boldsymbol{w}^r(m) + \boldsymbol{n}^r(m), \quad [5.1]$$

where $m = 1, \ldots, M$. In [5.1],the amplitude $a_k^r$ is proportional to the number of nuclei contributing to the spectral component of frequency $f_k$. The damping factor $d_k$ provides information about the mobility and macromolecular environment of the nucleus, $\phi_k$ is the phase, $\boldsymbol{l}(m)$ is the baseline, i.e., the contribution from the macromolecules, $\boldsymbol{w}(m)$ denotes the water signal and the noise term $\boldsymbol{n}(m)$ is assumed to be a circular complex white Gaussian noise.
Recent quantification algorithms impose spectral prior knowledge using metabolite templates [Provencher, 2001; Ratiney et al., 2005; Poullet et al., 2006]. The MRS signal can therefore be described as a linear combination of basis functions leading to:

$$\boldsymbol{y}^r(m) = \sum_{k=1}^{K} a_k^r \boldsymbol{b}_k(m) + \boldsymbol{l}^r(m) + \boldsymbol{w}^r(m) + \boldsymbol{n}^r(m), \qquad [5.2]$$

where $\boldsymbol{b}_k$ denotes a basis function (in the time or frequency domain) and the amplitudes $a_k^r$ are proportional to the concentration of the respective metabolites. Note that $m$ can refer to either a temporal or spectral index in [5.2]. Section 5.2.2 introduces the new quantification model investigated in this study.

### 5.2.2 Quantification Model

In MRS, quantification is the estimation of spectral parameters from measured data. Signal amplitude (in the time-domain) is the main parameter of interest since it is proportional to the metabolite concentration. Let $\boldsymbol{Y} \in \mathbb{C}^{M \times R}$ be the observed MRSI signal corresponding to a 2D slice involving $M$ spectral points and $R$ spatial positions. Let also $\boldsymbol{A} \in \mathbb{C}^{K \times R}$ be the matrix containing the contribution of the $K$ metabolites to the observed signal at each spatial position $r = 1, \ldots, R$. According to [5.2], and assuming that the water signal and the macromolecular contribution have been previously filtered, we propose to estimate the metabolite amplitudes from the following inverse problem

$$\boldsymbol{Y} = \boldsymbol{B}\boldsymbol{A} + \boldsymbol{N}, \qquad [5.3]$$

where

$$\boldsymbol{B} \triangleq \begin{bmatrix} b_1(1) & \dots & b_K(1) \\ \vdots & \vdots & \vdots \\ b_1(M) & \dots & b_K(M) \end{bmatrix}, \quad \boldsymbol{A} \triangleq \begin{bmatrix} a^1(1) & \dots & a^R(1) \\ \vdots & \vdots & \vdots \\ a^1(K) & \dots & a^R(K) \end{bmatrix}$$

$$\boldsymbol{Y} \triangleq \begin{bmatrix} y^1(1) & \dots & y^R(1) \\ \vdots & \vdots & \vdots \\ y^1(M) & \dots & y^R(M) \end{bmatrix}, \quad \text{and} \quad \boldsymbol{N} \triangleq \begin{bmatrix} n^1(1) & \dots & n^R(1) \\ \vdots & \vdots & \vdots \\ n^1(M) & \dots & n^R(M) \end{bmatrix}. \tag{5.4}$$

For each $k = 1, \dots, K$, $\boldsymbol{b}_k = [b_k(1), \dots, b_k(M)]^\intercal$ denotes a vector of the metabolite basis (spectral profile). For a fixed spatial position $r$, $\boldsymbol{u}^r = [a^r(1), \dots, a^r(K)]^\intercal$ is a column vector containing the contributions of the different metabolites to the observed MRS signal, and $\boldsymbol{n}^r = [n^r(1), \dots, n^r(M)]^\intercal$ is an additive complex-valued Gaussian noise of unknown covariance matrix $\boldsymbol{\Psi}$. Note here that the spatial positions have been vectorized so that a 2D slice is represented by an $R$-dimensional vector.

### 5.2.3 Classic resolution scheme

Our goal here is to solve the inverse problem [5.3] in order to obtain an estimate $\widehat{\boldsymbol{A}}$ based on the observation $\boldsymbol{Y}$, the knowledge of the basis $\boldsymbol{B}$ and the noise covariance matrix $\boldsymbol{\Psi}$. A basic solution to this problem is based on the minimization of the weighted least squares criterion:

$$\hat{\boldsymbol{A}}_{\text{WLS}} = \arg\min_{\boldsymbol{A}} \mathcal{J}_{\text{WLS}}(\boldsymbol{A}) = \arg\min_{\boldsymbol{A}} \| \boldsymbol{BA} - \boldsymbol{Y} \|^2_{\boldsymbol{\Psi}^{-1}} . \tag{5.5}$$

which leads to

$$\hat{\boldsymbol{A}}_{\text{WLS}} = (\boldsymbol{B}^{\text{H}} \boldsymbol{\Psi}^{-1} \boldsymbol{B})^{\sharp} \boldsymbol{B}^{\text{H}} \boldsymbol{\Psi}^{-1} \boldsymbol{Y}, \tag{5.6}$$

where $(\cdot)^{\text{H}}$ stands for transposed complex conjugate, $(\cdot)^{\sharp}$ stands for pseudo-inverse and,
$\| \cdot \|_{\boldsymbol{\Psi}^{-1}} = \sqrt{(\cdot)^{\text{H}} \boldsymbol{\Psi}^{-1} (\cdot)}$ defines a norm on $\mathbb{C}^K$.
Due to the instability of the covariance matrix or the ill-conditioning of the metabolite basis $\boldsymbol{B}$, the inverse problem [5.3] is generally ill-posed. In this case, the solution $\hat{\boldsymbol{A}}_{\text{WLS}}$ can be unstable and of poor quality. For this reason, one must generally resort to regularization [Tikhonov, 1963]. As detailed in

the previous chapter, regularization simply consists of introducing some prior knowledge on the target solution. This issue has been widely investigated in the MRI literature during the last decade [Ying et al., 2004b; Guerquin-Kern et al., 2009b; Chaari et al., 2011, 2014]. Different priors have therefore been investigated promoting smoothness or sparsity of the target solutions, either in the original space or in a transform domain.

### 5.2.4 Spatio-spectral regularization

To the best of our knowledge, all existing methods for regularized MRSI quantitation incorporate spatial smoothness assumptions on some spectral parameters such as phase or line width [Sava et al., 2011; Kelm et al., 2012]. While promoting spatial smoothness for such specific parameters, no constraint is used for the signal amplitudes. In this paper, we propose to incorporate prior knowledge on the MRSI data using a different regularization approach. On one hand, we exploit the sparsity of MR spectra by constraining the $\ell_1$ norm of the wavelet transform. On the other hand, we favor solutions (fits) with few irregularities in the spatial dimension by penalizing the wavelet coefficients of the MRSI grid at each frequency band (Fig. 5.1). The term "irregularities" mostly refers to noise and nuisance components typically present in MRSI data. In fact, in MRSI-acquisition conditions, the noise level is often similar in magnitude to some metabolite signal levels (like Lactate) and noise interferes with signal identification and determination of the metabolite amplitudes.
MRSI data might not be strictly sparse with respect to the $\ell_0$ pseudo-norm due to the typically low spatial resolution of these type of data. In fact, most commonly encountered signals are not strictly sparse in any domain, so that the notion of real sparsity is hard to find in practice. However, we aim to exploit the fact that MRSI data can be represented using only a few dominating coefficients in the wavelet domain leading to a low $\ell_1$ norm. This is true for both, the spectral and the spatial dimensions of the data. Indeed, the spatio-spectral sparsity of MRSI data have already been successfully used in compressed sensing imaging approaches [Hu et al., 2008; Geethanath et al., 2012].
Note that the proposed approach can be easily adapted to any convex penalization in both, the spectral and the spatial dimensions. This prior knowledge is included in the inversion scheme by using two regularization terms in the optimality criterion $\mathcal{J}_{\text{WLS}}$ in [5.5].

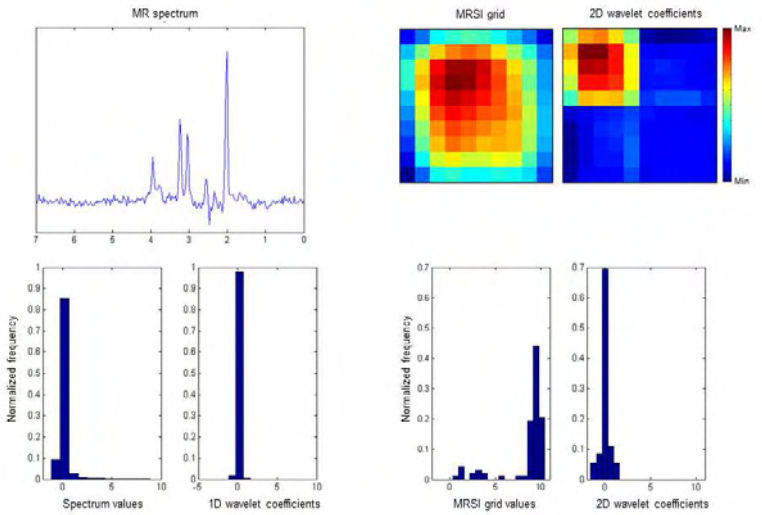


Figure 5.1: MRSI data have a few dominating coefficients in the wavelet domain in the spectral and the spatial dimensions. Top left: real part of a MR spectrum. Top right: MRSI dataset at a specific frequency position (MRSI grid) and its corresponding 2D wavelet transform. Bottom left: Normalized histograms showing the values of a MR spectrum ($\ell_1$) and its corresponding 1D wavelet coefficients. Bottom right: Normalized histograms showing the values of an MRSI grid (at a specific frequency position) and its corresponding 2D wavelet coefficients. Only the detail wavelet coefficients are shown in both cases.

#### 5.2.4.1 Spatio-spectral representation of the data

At a given spectral frequency $m$, let us denote by $\boldsymbol{y}^m \in \mathbb{C}^R$ the 2D complex-valued image of size $R = N_r \times N_c$ which results from reshaping the $R$-dimensional vector $(\boldsymbol{BA})^m$. On the other hand, the spectrum $\boldsymbol{y}^r = (\boldsymbol{BA})^{\boldsymbol{r}}$ of size $M$ at spatial position $r$ can be seen as an element of the Euclidean space $\mathbb{C}^M$.

#### 5.2.4.2 Spatio-spectral representation of the data in the wavelet domain

Using the same notation as in Section 4.3.2.2 in Chapter 4, we employ a dyadic 1D and 2D orthonormal wavelet decomposition operators, $F$ and $T$, over $j^1_{\max}$ and $j^2_{\max}$ resolution levels, respectively.

#### 5.2.4.3 Regularization terms

In order to constrain the solution $\widehat{\boldsymbol{A}}$ to have few irregularities both in the spatial and spectral dimensions, we propose to introduce two regularization terms. The first one describes the 2D spatial prior knowledge about the wavelet coefficients of the target solution. This first regularization term is defined as

$$g_1(\boldsymbol{A}) = \sum_{m=1}^{M} \left\{ \sum_{l=1}^{L_{J^1}} \Phi^p_{\mu_a,\alpha_a} \left[ \left( T(\boldsymbol{y}^m) \right)_{a,l} \right] + \sum_{o \in \mathbb{O}} \sum_{j=1}^{J^1} \sum_{l=1}^{L_j} \Phi^p_{\mu^j_o,\alpha^j_o} \left[ \left( T(\boldsymbol{y}^m) \right)_{o,j,l} \right] \right\}, \tag{5.7}$$

where $\Phi^p_{\mu,\alpha}(\xi) = \alpha|\xi - \mu|^p_p$, $\forall \xi \in \mathbb{C}$, $\mu^j_o \in \mathbb{C}$, $\alpha^j_o \in \mathbb{R}_+$ and $p \geq 1$ (and similarly for $\mu_a$ and $\alpha_a$). Due to the shape parameter $p$, this regularization term makes a compromise between sparsity ($p \sim 1$) and smoothness ($p \sim 2$) of the wavelet coefficients of the 2D image $\boldsymbol{y}^m$. The second regularization term allows us to reduce high spectral discontinuities (especially close to the metabolite peaks) between adjacent frequency bands at a voxel $r$. This regularization is made through the penalization of the wavelet coefficients of the 1D spectra $\boldsymbol{y}^r$:

$$g_2(\boldsymbol{A}) = \sum_{r=1}^{R} \left\{ \sum_{l=1}^{L_{J^2}} \Phi^\beta_{\eta_a,\lambda_a} \left[ \left( F(\boldsymbol{y}^r) \right)_{a,l} \right] + \sum_{j=1}^{J^2} \sum_{l=1}^{L_j} \Phi^\beta_{\eta^j_d,\lambda^j_d} \left[ \left( F(\boldsymbol{y}^r) \right)_{d,j,k} \right] \right\}, \tag{5.8}$$

where $\eta^j_d \in \mathbb{C}$, $\lambda^j_d \in \mathbb{R}_+$ and $\beta \geq 1$ (similarly for $\eta_a$ and $\lambda_a$).
Note that this kind of $\ell_p$ regularization has already been successfully used in sparse MRI reconstruction [Chaari et al., 2011, 2014].

#### 5.2.4.4 Optimization procedure

Based on the spatial and spectral regularization terms defined in [5.7] and [5.8] (resp. $g_1(\boldsymbol{A})$ and $g_2(\boldsymbol{A})$), and accounting for the quadratic data fidelity term $\mathcal{J}_{\text{WLS}}$, the new criterion to be optimized can be written as:

$$\mathcal{J}(\boldsymbol{A}) = \mathcal{J}_{\text{WLS}}(\boldsymbol{A}) + g_1(\boldsymbol{A}) + g_2(\boldsymbol{A}). \quad [5.9]$$

Note here that if for instance one wants to perform only spatial regularization, the spectral regularization term can be removed by setting $\lambda_d^j = \lambda_a = 0$ in [5.8]. However, using both regularizations allows high spectral and spatial discontinuities to be eliminated.
Since $\mathcal{J}$ is strictly convex, the uniqueness of the target solution is guaranteed. However, $\mathcal{J}$ is not necessarily differentiable, which makes impossible the use of standard gradient-based algorithms for minimization. As proposed in Chapter 4, the minimization of $\mathcal{J}$ in [5.9] can be performed by using the concept of proximity operators [Moreau, 1962]. The minimization problem that we need to solve here can not be tackled using PPXA, the proximal algorithm considered in Chapter 4. The denoising problem described in Chapter 4 can be expressed as the sum of a finite number of convex functions as follows:

$$\arg\min_x \sum_{i=1}^{m} f_i(x), \quad [5.10]$$

where $x$ are complex-valued variables. However,the problem that we need to solve now is slightly different:

$$\arg\min_x \sum_{i=1}^{m} f_i(\boldsymbol{B}x), \quad [5.11]$$

where $\boldsymbol{B}$ denotes the matrix in which each column is a metabolite profile.
An appropriate method to solve this optimization problem is the simultaneous direction method of multipliers algorithm (SDMM) firstly introduced in [Setzer et al., 2010] and detailed in [Combettes and Pesquet, 2008]. This methods requires that the matrix $\boldsymbol{B}^T\boldsymbol{B}$ is invertible and the estimation of the proximity operator of the three terms of the criterion to be minimized [5.9], i.e., the data fidelity term and the spatio-spectral regularization terms. The expressions of the proximity operators of these functions and the details of the minimization algorithm are described below.

#### 5.2.4.5 Proximity operator of the data fidelity term

Based on the above definitions, and according to standard rules about the calculation of proximity operators [Combettes and Pesquet, 2011, Table 1], the proximity operator of the data fidelity term $\mathcal{J}_{\text{WLS}}$ is given by:

$$\text{prox}_{\mathcal{J}_{\text{WLS}}} \boldsymbol{A} = \left(\boldsymbol{I}_d + 2\Psi^{-1}\right)^{-1}\left(\boldsymbol{B}\boldsymbol{A} + 2\Psi^{-1}\boldsymbol{Y}\right). \quad [5.12]$$

#### 5.2.4.6 Proximity operators of the regularization terms

Regarding the regularization terms, the proximity operator of $\Phi^p_{\mu,\alpha}$ for every $\xi \in \mathbb{C}$ is given by

$$\text{prox}_{\Phi^p_{\mu,\alpha}} \xi = \text{sign}(\xi)\eta, \quad [5.13]$$

where $\eta = \eta^{\text{Re}} + i\eta^{\text{Im}}$ is the unique solution in $\mathbb{C}_+$ to $\eta + p\eta^{p-1}\alpha = |\xi - \mu|$. If $p = 1$, this proximity operator simplifies as follows:

$$\begin{aligned}\text{prox}_{\Phi^1_{\mu,\alpha}} \xi = \text{sign}\Big[\text{Re}(\xi-\mu)\Big] \max\{|\text{Re}(\xi-\mu)| - \text{Re}(\alpha), 0\} \\ + i\ \text{sign}\Big[\text{Im}(\xi-\mu)\Big] \max\{|\text{Im}(\xi-\mu)| - \text{Im}(\alpha), 0\}. \quad [5.14]\end{aligned}$$

By referring to the spatial and spectral regularization terms $g_1$ and $g_2$ in [5.7] and [5.8], it turns out that the proximity operator of the regularization term can be obtained by calculating the proximity operator of $\Phi^p_{\mu,\alpha} \circ T$ and $\Phi^\beta_{\eta,\lambda} \circ F$. These operators can be calculated based on [Combettes and Pesquet, 2008, Lemma 2.4], leading to $\text{prox}_{\Phi^p_{\mu,\alpha}\circ T} = T^{-1} \circ \text{prox}_{\Phi^p_{\mu,\alpha}} \circ T$ (similarly for $\text{prox}_{\Phi^\beta_{\eta,\lambda}\circ F}$).
Based on the calculated proximity operators, the resulting algorithm for the minimization of the optimality criterion in [5.9] is described below in Algorithm 2.

It is important to note that the computations in this algorithm can be performed in a parallel manner (steps 4 to 6 can be computed in parallel for each $i$). In addition, the global convergence of the algorithm to an optimal solution to the minimization problem is guaranteed. The parameter $\gamma$ is related to the convergence speed of the algorithm and has been chosen by cross validation for each case [Combettes and Pesquet, 2008]. The stopping parameter $\epsilon$ has been set to $10^{-6}$ and the algorithm normally converges in less than 50 iterations.

**Algorithm 2 Simultaneous Direction Method of Multipliers**

Set $\gamma > 0$, $\epsilon \in ]0,1[$, ${\boldsymbol{Z}^1}_{i,0} \in \mathbb{C}^{M \times R}$, ${\boldsymbol{Z}^2}_{i,0} \in \mathbb{C}^{M \times R}$, $i \in \{1, ..., N\}$, $\boldsymbol{Q} = \sum_{n=1}^{N} \boldsymbol{B}^* \boldsymbol{B}$ ($N = 3$ in our case). Set $n = 1$.

1: **repeat**
2: Set $\boldsymbol{A}_n = \boldsymbol{Q}^{-1} \sum_{i=1}^{N} \boldsymbol{B}^* ({\boldsymbol{Z}^1}_{i,n} - {\boldsymbol{Z}^2}_{i,n})$
3: **for** $i = 1$ to $N$ **do**
4: Set $\boldsymbol{Y}_{i,n} = \boldsymbol{B}\boldsymbol{A}_n$.
5: Calculate ${\boldsymbol{Z}^1}_{i,n+1} = \text{prox}_{\gamma g_i}(\boldsymbol{Y}_{i,n} + {\boldsymbol{Z}^2}_{i,n})$.
6: Set ${\boldsymbol{Z}^2}_{i,n+1} = {\boldsymbol{Z}^2}_{i,n} + \boldsymbol{Y}_{i,n} - {\boldsymbol{Z}^1}_{i,n+1}$.
7: **end for**
8: $n \leftarrow n + 1$.
9: **until** $|\mathcal{J}(\boldsymbol{A}_n) - \mathcal{J}(\boldsymbol{A}_{n-1})| < \epsilon$
10: **return** $\hat{\boldsymbol{A}} = \boldsymbol{A}_n$.

## 5.3 Results

### 5.3.1 Synthetic Data

In order to evaluate the performance of the proposed method, different experiments on synthetic data were designed. Simulated MRSI datasets were constructed by combining profiles from the principal metabolites observed in long echo time brain MRS: choline (Cho), creatine (Cr), N-acetyl-aspartate (NAA) and lactate (Lac). Metabolite profiles were obtained from quantum mechanical simulations of a spin-echo MR experiment using the jMRUI software package [Stefan et al., 2009]. First, $N = 50$ Monte Carlo simulations of MRSI data sets of size $10 \times 10$ were performed to measure the accuracy of the proposed method as a function of SNR. To this aim, five different levels of white Gaussian noise were added to a noiseless simulated data set. The SNR in dB of each signal, $\boldsymbol{Y}$, was computed in the frequency domain as $\text{SNR} = 20 \log_{10} \frac{\|\boldsymbol{S}_{\text{ref}}\|_2}{\|\boldsymbol{S}_{\text{ref}} - \boldsymbol{Y}\|_2}$, where $\boldsymbol{S}_{\text{ref}}$ denotes the noiseless signal. Fig. 5.2 shows examples of spectra for different noise levels considered in this experiment.

The root-mean-squared error (RMSE) of the estimated amplitudes for each metabolite $k$ was calculated for each voxel $r$ as:

$$\text{RMSE}_{k,r} = \sqrt{\frac{1}{N} \sum_{n=1}^{N} \frac{(a_{k,r,n}^{\text{ref}} - \hat{a}_{k,r,n})^2}{(a_{k,r,n}^{\text{ref}})^2}}, \qquad [5.15]$$

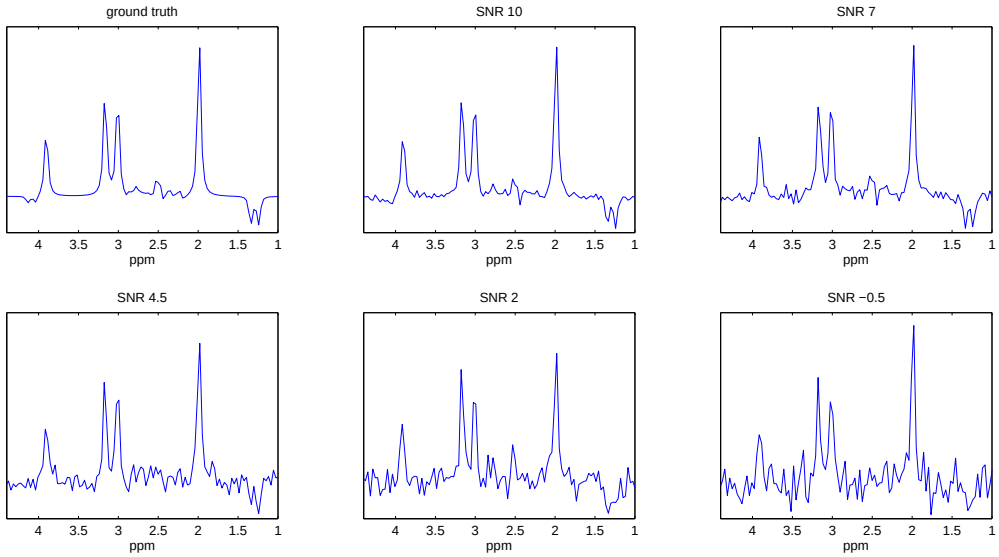


Figure 5.2: Synthetic MRSI spectra for different noise levels [SNR = -0.5, 2, 4.5, 7, 10] and noiseless ground truth.

where $a^{\text{ref}}_{k,r,n}$, $\hat{a}_{k,r,n}$ are the true and estimated amplitudes of the $k$th metabolite respectively at voxel $r$ for the $n$th simulation.

Fig. 5.3 compares the estimation error of the proposed method referred to as Spatial-Spectral Regularization (SSR), with the voxel-wise quantification method AQSES [Poullet et al., 2006] and AQSES-MRSI [Sava et al., 2011]. The estimation error is measured as the $\text{RMSE}_{k,r}$ averaged over all the metabolites and over all the voxels. The increase in accuracy due to the incorporation of the spatial-spectral prior (in the proposed method) is clearly observed. The errors of the proposed method when only one of the regularization terms is considered, referred to as SSR-Spatial (only the spatial regularization term is used) and SSR-Spectro (only the spectral regularization term is used), are also displayed. In the same figure (Fig. 5.3), the errors in the metabolite amplitudes estimated with each method are also compared with the CRLB obtained from the individual voxel approach. SSR provides the best results for all noise levels reducing the error by a mean of 41%, from 24% to 54% depending on the noise level. This difference of accuracy can be

clearly observed and is even below the CRLB in some cases.
A similar analysis is shown in Fig. 5.4, where the mean $\text{RMSE}_{k,r}$ averaged over all the voxels is shown for each individual metabolite.

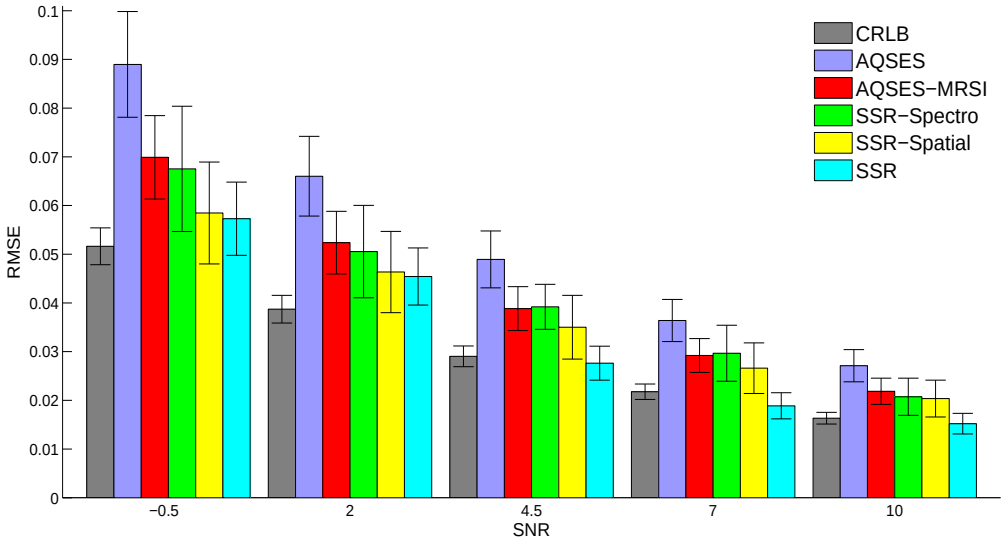


Figure 5.3: $\text{RMSE}_{k,r}$ of the estimated metabolite amplitudes averaged over all the metabolites and over all the voxels computed for 50 synthetic MRSI data sets of size $10 \times 10$ for 5 different noise levels (SNR values are: -0.5, 2, 4.5, 7, 10). The proposed method (SSR) is compared with a voxel-wise quantification method (AQSES) and with a quantification method dedicated to MRSI data (AQSES-MRSI). The averaged RMSE of the proposed method when only the spectral term (SSR-Spectro) or only the spatial term (SSR-Spatial) are considered are also displayed. The CRLBs shown were computed from AQSES.

Fig. 5.5 shows the quality of the fit (measured by the SNR) for each method for different noise levels. The curves show the SNR of the fits, i.e, how close is each fitted model to the ground truth signal. The error bars represent the mean $\text{RMSE}_{k,r}$ of the estimated metabolite amplitudes averaged over all the metabolites and all the voxels at each noise level.
Fig. 5.6 shows the scatter plots of the $\text{RMSE}_{k,r}$ of the metabolite amplitudes at each voxel. Each point corresponds to a given voxel. In most of the voxels,

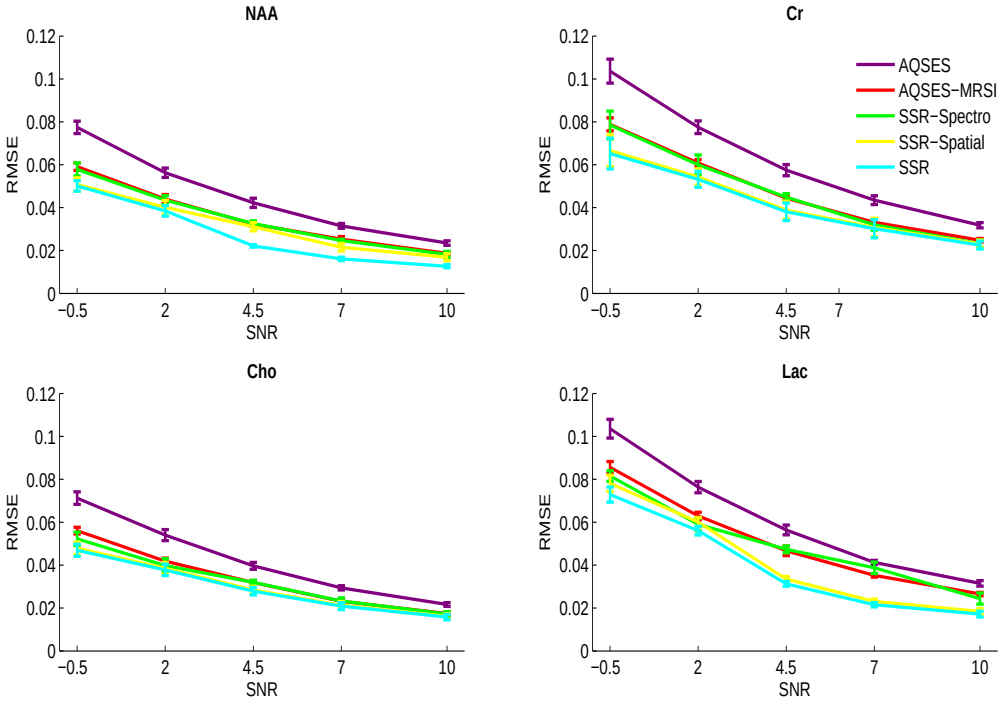


Figure 5.4: Mean $\text{RMSE}_{k,r}$ of the estimated metabolite amplitudes averaged over all the voxels computed for 50 synthetic MRSI data sets of size $10 \times 10$ for 5 different noise levels (SNR values are: -0.5, 2, 4.5, 7, 10). The proposed method (SSR) is compared with a voxel-wise quantification method (AQSES) and with a quantification method dedicated to MRSI data (AQSES-MRSI). The averaged $\text{RMSE}_{k,n}$ of the proposed method when only the spectral term (SSR-Spectro) or only the spatial term (SSR-Spatial) are considered are also displayed.

the proposed method yields lower errors for the metabolite amplitudes when compared to the AQSES-MRSI method.

A second experiment was considered in order to check that the proposed method preserves spatial features. Two MRSI data sets of size $10 \times 10$ representing different spatial features were generated. Both data sets contain a region with healthy appearing signals and a region with tumor-like signals. In the first case there is a sharp transition between the two regions, while a smoother change is applied for the second dataset. The Structural SIMilar-

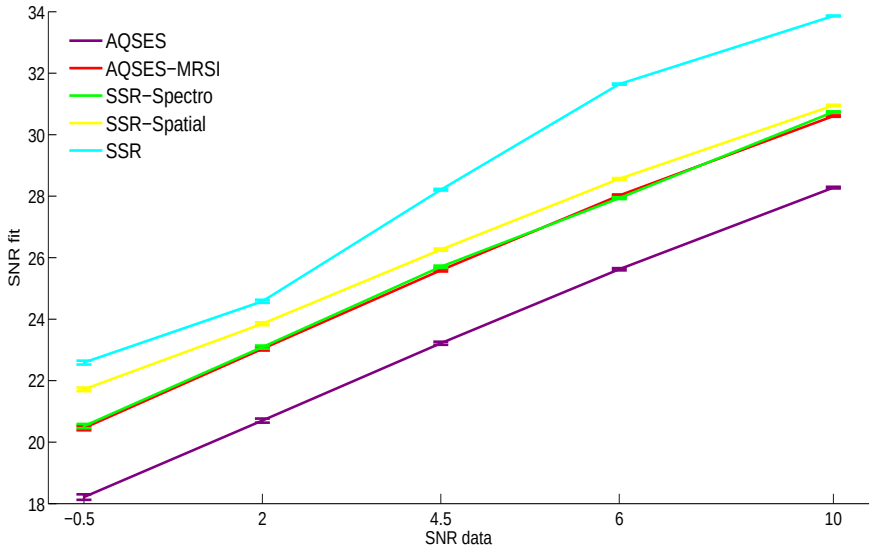


Figure 5.5: Mean SNR values computed for 50 synthetic MRSI data sets of size $10 \times 10$ for 5 different noise levels (SNR values are: -0.5, 2, 4.5, 7, 10). The error bars indicate the mean $\text{RMSE}_{k,r}$ of the estimated metabolite amplitudes averaged over all the metabolites and all the voxels.

ity ($\text{SSIM}_k$) index [Wang et al., 2004] was estimated for the amplitude map of each metabolite. This index provides a valuable measure of performance over the whole grid for each metabolite. Fig. 5.7 presents results obtained for a synthetic data set where the border between the regions of healthy and abnormal spectra is a sharp edge. The first row shows the ground truth for the amplitudes of NAA, Cr, Cho and Lac. The following rows show the solutions obtained from three different approaches and their differences from the ground truth. More precisely, the second row shows the results using the single-voxel approach, the third row shows the results using AQSES-MRSI, the fourth row shows the proposed spectral-spatial prior (SSR), whereas the last three rows show differences between the estimated concentrations and the ground truth. The differences are measured as the percentage respect to the maximum ground truth value for each metabolite. Table 5.1 and table 5.2 show the SSIM values for he metabolite maps in Fig. 5.8 and Fig. 5.8, respectively. This values offer an objective and quantitative measure of the accuracy of the metabolic maps obtained with the different methods.

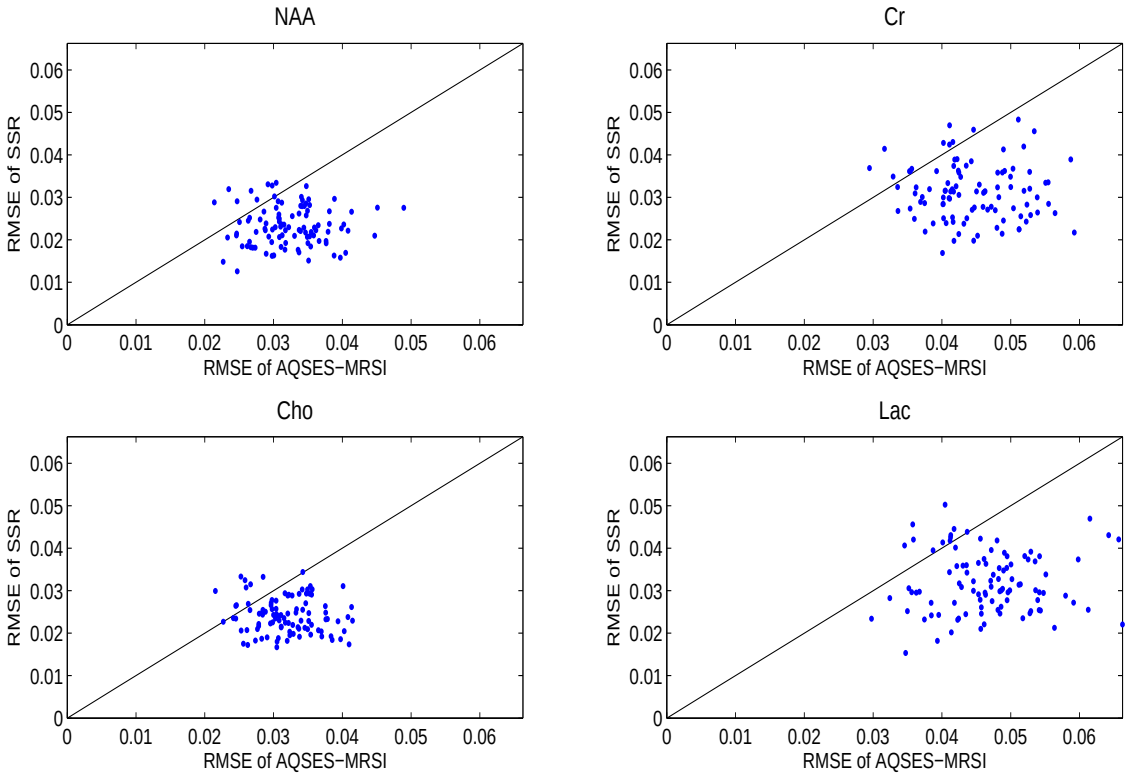


Figure 5.6: $\text{RMSE}_{k,r}$ of the estimated metabolite amplitudes obtained with the proposed method (SSR) and with AQSES-MRSI for 50 synthetic MRSI data sets of size $10 \times 10$ at SNR=4.5. Each point corresponds to one voxel of the MRSI grid.

The same experiment was performed for a simulated data set where the border between healthy and abnormal tissues is represented by a smoother edge. Results are shown in Fig. 5.8.
For all the experiments (for both synthetic and in vivo data), a Daubechies basis with 2 vanishing moments over one resolution level ($J^1 = 1$ and $J^2 = 1$ in [5.7] and [5.8], respectively) was considered. Different types of wavelet families were tested and Daubechies showed to be the best suited for this type of data. The reason to use one resolution level is twofold. On one hand, no significant improvements were noticed using resolution levels greater than

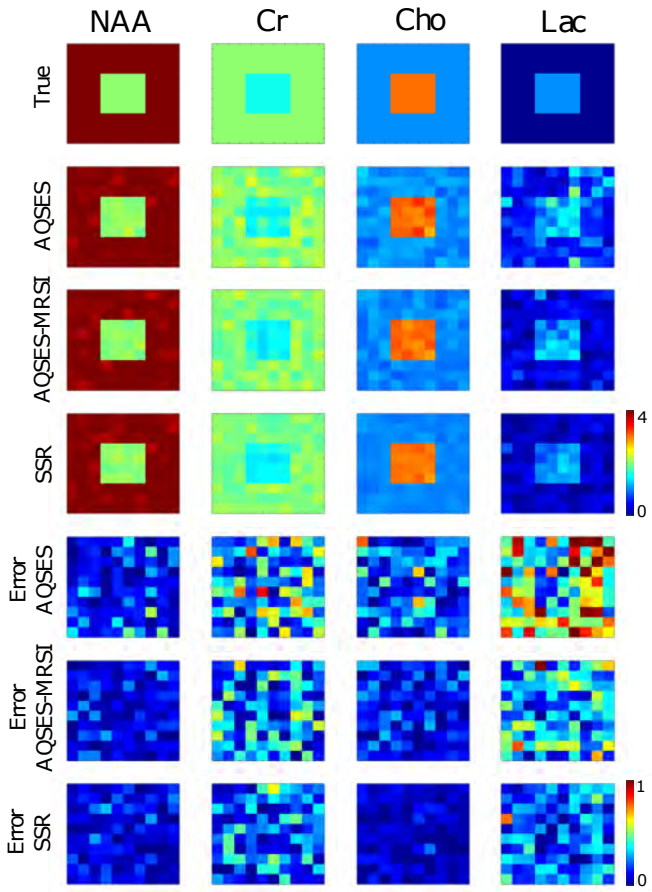


Figure 5.7: Synthetic MRSI data set containing two regions associated with healthy and tumor-like signals separated by a sharp edge. From top to bottom: true metabolite concentrations, estimated metabolite concentrations using AQSES, AQSES-MRSI and SSR, difference (error) between the true metabolite concentrations and the concentrations estimated using AQSES, AQSES-MRSI and SSR.

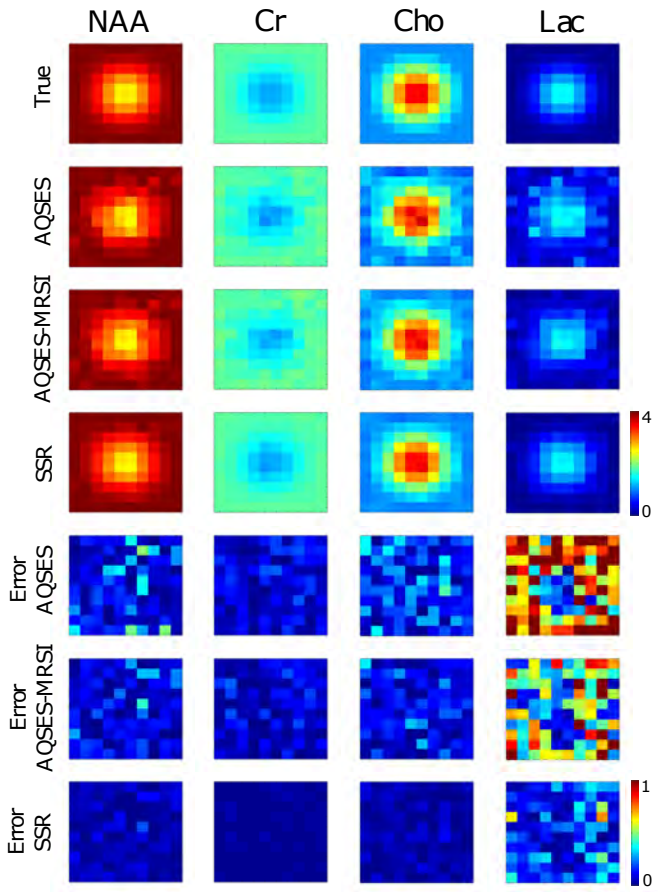


Figure 5.8: Synthetic MRSI data set containing a region with healthy appearing signals and a region with tumor-like signals separated by a smooth edge. From top to bottom: true metabolite concentrations, estimated metabolite concentrations using AQSES, AQSES-MRSI and SSR, difference (error) between the true metabolite concentrations and the concentrations estimated using AQSES, AQSES-MRSI and SSR.

one [Laruelo et al., 2013a]. In the spatial dimension, this is mainly due to the typically low spatial resolution of the MRSI images used in the clinical routine (no bigger than $32 \times 32$). On the other hand, increasing the number of resolution levels increases the number of regularization parameters to be set, which could lead to less preciseness in the prior information used for regularization. In order to promote sparse solutions in the wavelet domain, the values of $p$ and $\beta$ in equations [5.7] and [5.8], respectively, are set to $p = \beta = 1$ for all the experiments. Note that only detail coefficients were processed. This is equivalent to setting the regularization parameter to zero for the approximation coefficients. Regularization parameters were selected manually by testing a number of values for each MRSI dataset. The combination of parameters providing the best trade-off between spectral SNR and spatial features preservation were selected. It is worth noticing that fully autocalibrated approaches may be used to automatically estimate these parameters directly from the data [Belge et al., 2002; Chaari et al., 2010].

| SSIM | AQSES | AQSES-MRSI | SSR |
|---|---|---|---|
| NAA | 0.69 | 0.87 | 0.91 |
| Cr | 0.59 | 0.68 | 0.78 |
| Cho | 0.78 | 0.91 | 0.94 |
| Lac | 0.20 | 0.27 | 0.36 |

Table 5.1: SSIM values for each metabolite amplitude map in Fig. 5.7.

| SSIM | AQSES | AQSES-MRSI | SSR |
|---|---|---|---|
| NAA | 0.83 | 0.94 | 0.98 |
| Cr | 0.61 | 0.87 | 0.90 |
| Cho | 0.78 | 0.92 | 0.95 |
| Lac | 0.41 | 0.55 | 0.69 |

Table 5.2: SSIM values for each metabolite amplitude map in Fig. 5.8.

### 5.3.2 In vivo data

We further analyze the performance of our method for in vivo MRSI data. In vivo MRSI data were acquired at Institut Claudius Regaud using a 1.5T clinical MR scanner (Siemens Magnetom Avanto) using a 3D CSI sequence with water suppression, TE=135 ms, TR =1500 ms, 512 FID data points, 4 averages, slice thickness: 15mm, matrix size: $16 \times 16$, FOV: $160 \times 160$ mm yielding a voxel size of 10 mm $\times$ 10 mm $\times$ 15 mm. Data were acquired from a healthy volunteer and from two patients with diagnosed Glioblastoma multiforme included in a prospective clinical trial. Note that an estimation of the noise covariance matrix $\mathbf{\Psi}$ has been obtained from a signal(and artifact)-free part of the MRSI spectra for in vivo data. Preprocessing applied to in vivo MRSI signals includes: residual water suppression (using the Hankel singular value decomposition (HSVD) algorithm [Laudadio et al., 2002]) and standard polynomial baseline correction. For the quantification of in vivo data, a metabolite basis set containing Cho, Cr, NAA and Lactate was considered. The choice of this basis set was based on the fact that these metabolites are the most visible in long echo time spectra. Due to the experimental conditions suffered by in vivo signals during the acquisition, it is typically necessary to apply phase, frequency and damping corrections to the simulated metabolite profiles. We have used AQSES to estimate these corrections for each MRSI signal. The estimated corrections were then averaged over the MRSI grid and applied to the metabolite profiles in the basis set $B$ [5.3].

The robustness of the proposed method was tested on in vivo data to check if the results are consistent with real conditions. Metabolite maps obtained using the proposed method were compared with the maps obtained using voxel-wise quantification methods (AQSES [Poullet et al., 2006] and QUEST [Ratiney et al., 2005]) and the spatially-constrained approach AQSES-MRSI [Sava et al., 2011]). Regularization parameters were selected manually using a grid-search strategy as described in Section 5.3.1. The SNR for in vivo spectra was computed in frequency domain as $SNR = \frac{I}{\sigma}$, where $I$ denotes the height of the NAA peak in the real spectrum and $\sigma$ the standard deviation of the noise (measured in a signal-free region of the spectrum) [Kreis, 2004]. On Fig. 5.9, the metabolite maps depict the presence of NAA, Cho and Cr as expected in healthy tissue. For the operated GBM patient (Fig. 5.10), the Lac map presents a spatial distribution which matches with the surgical cavity. The presence of Lac is often observed after surgery and can be linked

to the post-operative reorganization of the tissue. The Cho map presents higher concentrations in correspondence with the contrast-enhancing bud of the anterior part of the lesion, suggesting higher cellular proliferation in this area. For the non-operated GBM patient (Fig. 5.11), the NAA map presents lower concentrations spatially matching the center of the contrast-enhancement area and the necrosis that can be seen on the T1-weighted post-gadolinium injected MR image. The Cho map shows high concentrations corresponding to the anterior left part of the contrast-enhancing lesion. The elevated presence of Cho together with the collapsing of NAA suggests a metabolically active tumor region. The Lac map shows higher concentration at the anterior left part of the tumor, suggesting the presence of anaerobic metabolism in this area and emphasizing the heterogeneous aspect of the tumor. Fig. 5.12 shows nine adjacent voxels from a patient with brain tumor and the corresponding fits from AQSES, AQSES-MRSI and SSR.
Regarding the computational cost, SSR is quite efficient. The computation time depends on the size of the MRSI grid, the samples of the spectra and on the level of noise. For the in vivo cases presented in this study, the computation times for processing the whole image were between 50 and 90 seconds. The experiments were done on a 64-bit 1.8GHz i7-4500U architecture with a Matlab implementation (R2013a). The convexity of the objective function guarantees the convergence to a global minimum.

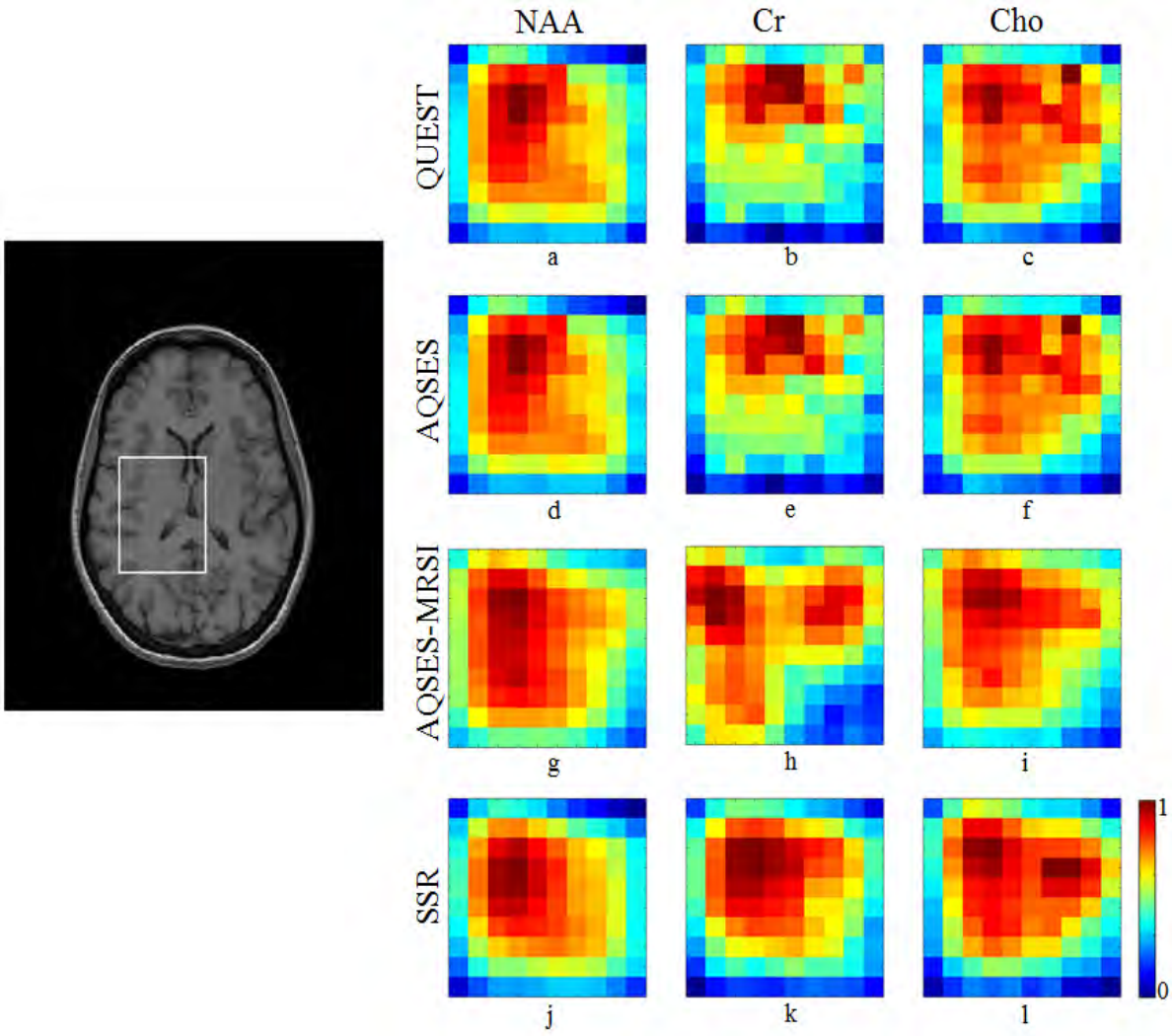


Figure 5.9: In vivo 3D MRSI acquisition on a healthy volunteer located in the central hemispheric right part of the brain. Metabolite maps of NAA, Cr and Cho are presented, respectively from top to bottom, using QUEST, AQSES, AQSES-MRSI and SSR. For comparison purposes metabolite estimations have been normalized between 0 and 1.

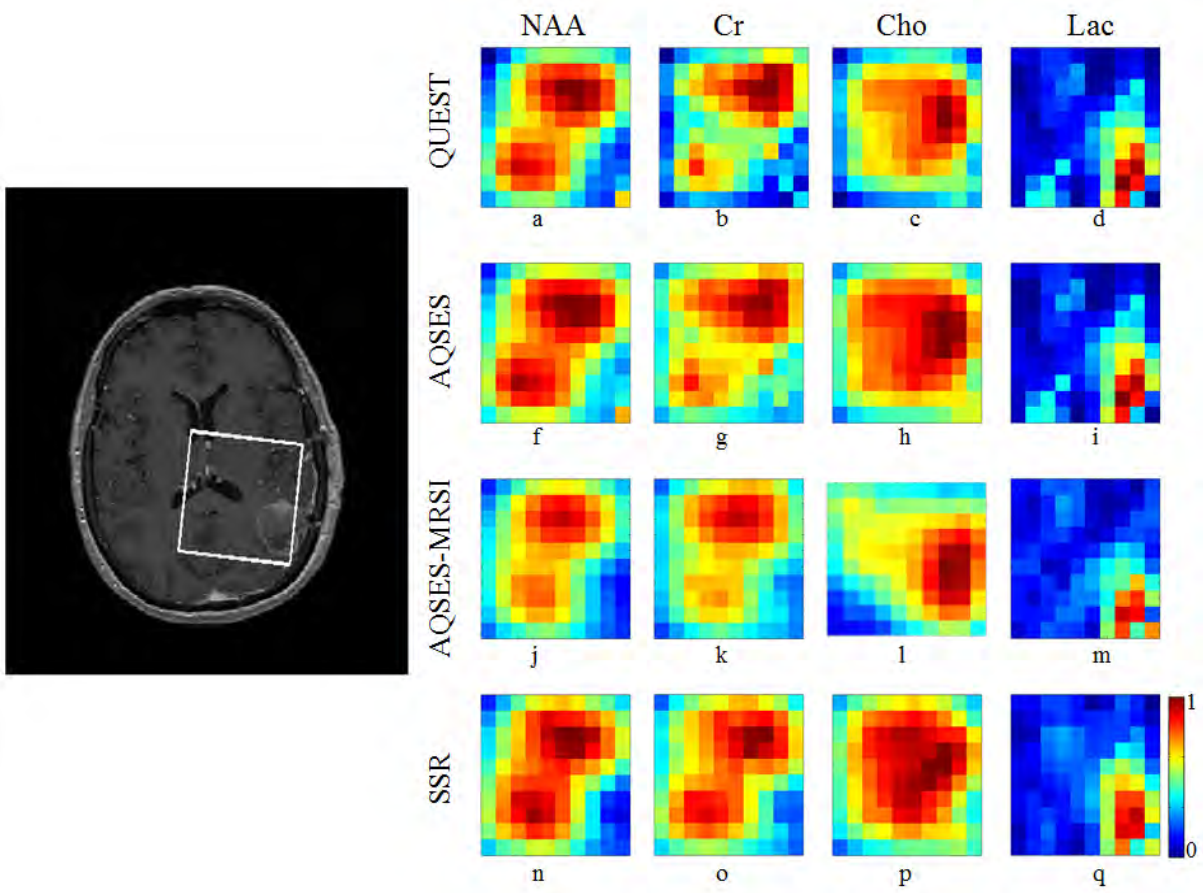


Figure 5.10: In vivo 3D MRSI acquisition on a resected Glioblastoma multiforme patient with a left parietal lesion associated to a thin peripheral contrast-enhancement. Metabolite maps of NAA, Cr, Cho and Lac are presented, respectively from top to bottom, using QUEST, AQSES, AQSES-MRSI and SSR. For comparison purposes metabolite estimations have been normalized between 0 and 1.

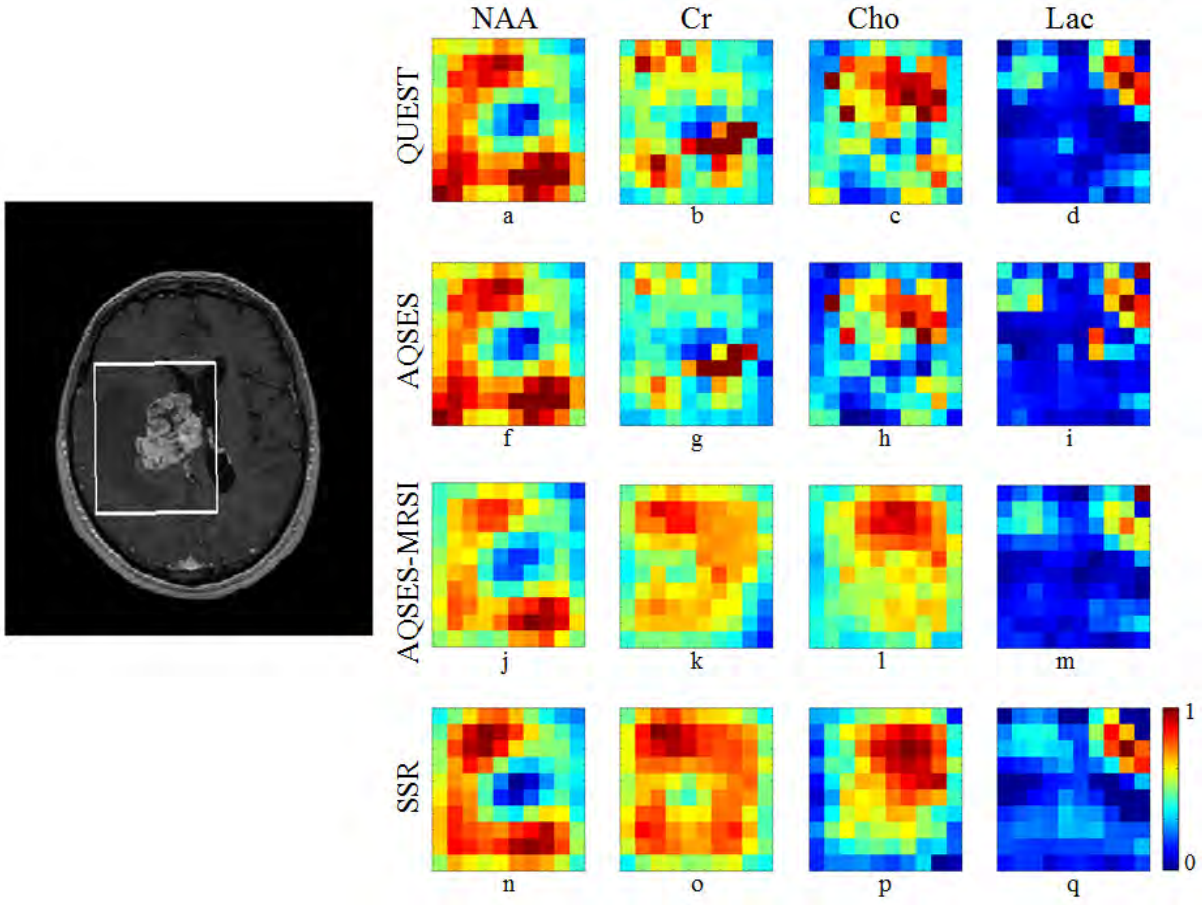


Figure 5.11: In vivo 3D MRSI acquisition on a biopsied Glioblastoma multiforme patient presenting a central hemispheric right lesion with a mass effect on the right lateral ventricle and a deviation of the structures thorugh the left of the median line. Metabolite maps of NAA, Cr, Cho and Lac are presented, respectively from top to bottom, using QUEST, AQSES, AQSES-MRSI and SSR. For comparison purposes metabolite estimations have been normalized between 0 and 1.

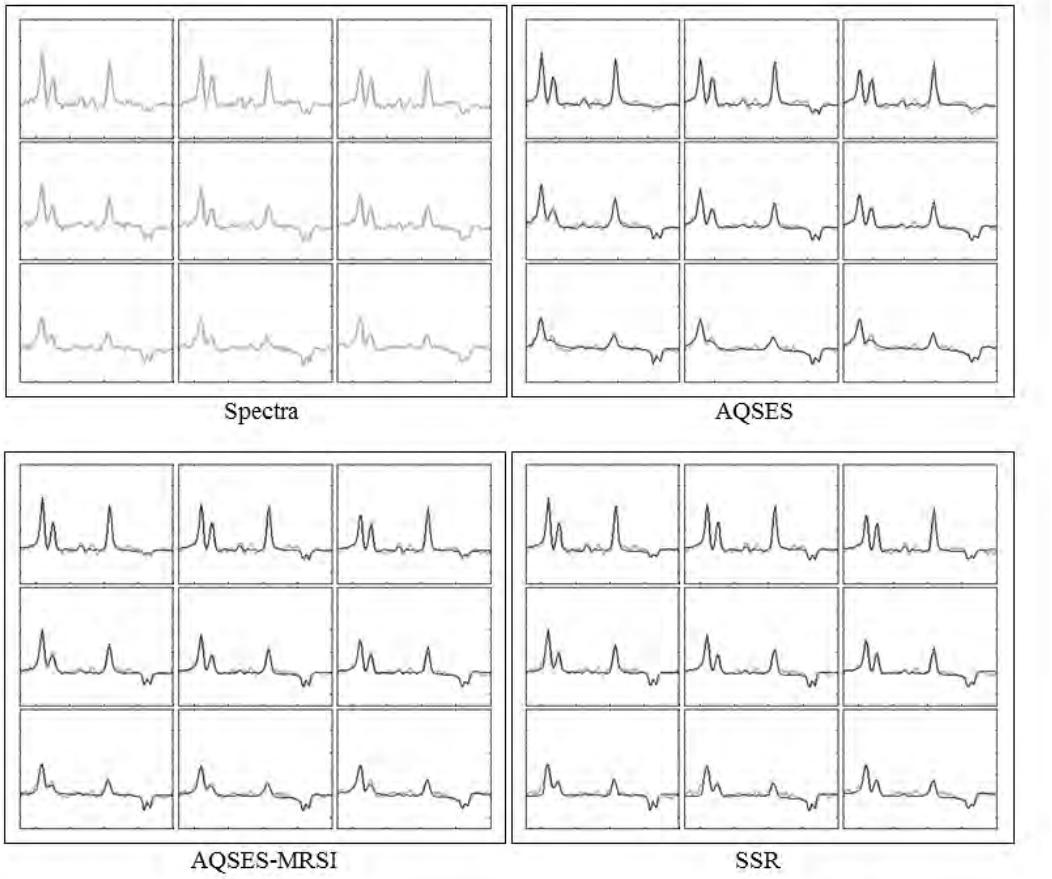


Figure 5.12: Nine adjacent voxels from a patient with a brain tumor (Gliobastoma Multiforme) and the corresponding AQSES, AQSES-MRSI and SSR fits. Cr and Lac peaks are erroneously fitted by the voxel-wise approach (AQSES) in many voxels. AQSES-MRSI clearly improves the quality of the fits but still Cr and Lac are not well captured. SSR is able to correctly fit all the spectra.

## 5.4 Discussion

In order to apply the MRSI technique to routine clinical practice, it is important to maximize the accuracy and the robustness of the quantification. Additionally, both processing time and technique subjectivity should be minimized by, for example, automation. The use of regularization techniques has been proved to be a powerful approach to achieve these objectives. We have presented here a quantification method based on a combined spatial-spectral regularization scheme. Contrary to previous methods, the regularization terms are expressed in the wavelet domain. This allows the method to explore other types of prior knowledge and going beyond the conventional assumption of spatial smoothness . The benefits of imposing appropriate constraints for both spectral and spatial dimensions of MRSI data have been presented in this chapter. Experiments with synthetic data show that the proposed method increases the accuracy and the robustness against noise of the quantification (Fig. 5.3). The presented spectral-spatial prior prevents the quantification algorithm from moving away from the true solution by narrowing down the search space. As a result, the method becomes, not only more accurate, but also more robust being able to cope with signals containing high noise levels. The better accuracy provided by SSR can be explained by a more accurate fitting of the data as shown in Fig. 5.5. The proposed method outperforms other quantification methods even in the presence of sharp spatial features as it is shown in 5.7 and in Table 5.1. The higher SSIM values provided by SSR confirm objectively that the metabolic maps obtained by SSR are closer to the ground truth than the maps from AQSES and AQSES-MRSI. Experiments with in vivo data show that the proposed method provides less noisy spatial metabolite distributions. This leads to better contoured metabolite maps. In addition, overlapping peaks (e.g., Cho and Cr with respective resonance frequency at 3.2 and 3.0 ppm) and metabolites present at relatively low concentrations (e.g., lactate) can be better estimated (Fig. 5.12). The good performance of the method can be explained by the $\ell_1$-norm regularization which leads to soft-thresholding of the wavelet coefficients. The wavelet thresholding acts a non-linear low-pass filter in the wavelet domain where most image information is contained in a few largest wavelet coefficients, while the noise is uniformly spread out across all coefficients. Thus thresholding mostly affects the noise rather than the signal. The risk of missing spatial features of the smoothing filters is alleviated by

wavelets, which preserve the sharpness of images. Another interesting property is that, even if we focus in the use of the $\ell_1$-norm in this manuscript, the presented method in not restricted to this case. Other $\ell_p$-norm (for $1 \geq p$) could be considered since the method can cope with any convex penalty. Therefore, the regularization imposed on the spectral and spatial dimensions can be different. For example, it might be interesting to exploit the sparsity of the spectral dimension in combination with a spatial smoothness prior to quantify MRSI data from a homogeneous region. It is interesting to note that the use of an averaged metabolite basis set could limit the performance of the method in case of high variances between voxels. However, this limitation is true for any method assuming smooth spatial variations. Methods able to handle different metabolite basis for each voxel will be analyzed in future studies. Interestingly, the proposed method requires tuning only two parameters which give weights to the two regularization terms and can be automatically estimated from the data [Chaari et al., 2010]. This facilitates the necessary automation of the quantification process in order to make MRSI, not only appealing but, feasible into the clinical setting. The method presented here can be extended to incorporate 3D spatial information by using a 3D wavelet operator. This makes it especially attractive in view of the increasing interest in high resolution 3D MRSI data where the low SNR is a main limiting factor.

## 5.5 Conclusion

A new method combining spatial and spectral regularizations in the wavelet domain to improve MRSI data quantification has been presented. It benefits from the combination of using a basis of metabolite profiles and incorporating simultaneously spectral and spatial constraints. Contrary to previous approaches, the suggested method combines two regularization terms to favor solutions with specific properties in both the spatial and the spectral dimensions. Note that the spectral parameters are not restricted to have spatially smooth variations. The method allows the use of other priors promoting properties such as the sparsity of the MRSI spectra in the wavelet domain. Experiments on synthetic data clearly demonstrated some significant improvements in quantification accuracy and robustness by using the proposed spatial-spectral regularization. Experiments on in vivo data showed well contoured metabolite maps that can be used to define more targeted and

more individualized treatments [Laprie et al., 2008; Ken et al., 2013; Deviers et al., 2014]. In addition, the presented method was able to correctly quantify metabolites that are missed by other methods due to the presence of noise or nuisance components as it has been shown for the case of the lactate. This is especially relevant for the quantification of metabolites present in low concentrations. The dependency on only two hyperparameters and the use of a fast proximal algorithm that allows parallel computations facilitate the automation of the presented method, which is crucial for the acceptance of any quantification method to the routine clinical implementation. Future work includes the extension of the proposed method to incorporate 3D spatial information available from 3D MRSI data and validation with high spatial resolution MRSI images where the low signal-to-noise ratio is a major limitation. The integration of an automatic hyperparameter estimation method is also an interesting prospect. Furthermore, the proposed method can be extended to incorporate more sophisticated priors, such as tissue distributions and anatomical structures extracted from companion MRI images.

# Chapter 6

# Tumor relapse prediction based on multi-parametric MR data classification

## Contents



## 6.1 Introduction

In the previous chapter (Chapter 5), a novel quantification method for MRSI data is proposed. The estimated metabolite amplitudes can be used as input features in a classifier to discriminate different tissue types based on metabolic information. From this point of view, quantification can be considered as a feature extraction and dimension reduction technique. In this chapter, we propose an automated decision support system based on a supervised classification method for the identification of regions at risk of relapse in brain tumor patients. The ultimate goal is to show the potential of combining metabolic information with other MRI imaging modalities to define new biologically tailored target volumes for dose escalation in radiotherapy treatments.

## 6.2 Motivation

GBM is the most common and deadliest of malignant primary brain tumors in adults [Stupp et al., 2005]. The current standard of care is surgical resection (if feasible) followed by radiotherapy (RT) and concomitant and adjuvant temozolomide (TMZ) chemotherapy [Stupp et al., 2005]. Although RT has played a key role in the treatment of this tumor since several decades ago, local tumor regrowth occurs in irradiated areas in 93% of the patients [McDonald et al., 2011]. Recent RT technologies, such as the intensity-modulated radiation therapy (IMRT) [Amelio et al., 2010; Monjazeb et al., 2012], allow the delivery of high doses to specific regions of the tumor while sparing normal tissue. These technical advances enable to consider innovative strategies to optimize the treatment of GBM. One of these strategies is based on the assumption that the local tumor control may be improved if the tumor areas with high probability of recurrence received a higher dose [Laprie et al., 2008; Deviers et al., 2014]. Therefore, the identification of sites with high probability of recurrence appears as a promising way to define new target volumes for dose escalation in RT treatments.

MRI is used for diagnosis, characterization, and radiotherapeutic treatment planning of brain tumors. However, conventional MRI has a limited specificity in describing the tumor extent and functional regions within the heterogeneous GBM tumors. The use of more advanced MR techniques, like MRSI, is a promising tool for the analysis of brain tumours as it is able to characterize biochemical, metabolic, and pathologic changes of brain tissues [Alger et al., 1990; Dowling et al., 2001; Astrakas et al., 2004; Tzika, 2008]. Previous studies have shown that certain metabolically abnormal regions detected by MRSI are predictive of the location of tumor relapse [Nelson, 2001; Laprie et al., 2008; Deviers et al., 2014]. MRSI data interpretation has been mainly based on single-variable classifiers, i.e., MRSI voxels with a value greater than or equal to a threshold would receive a positive prediction, and those below the threshold would receive a negative prediction [McKnight et al., 2001; Laprie et al., 2008; Raschke et al., 2014; Deviers et al., 2014]. A multiparametric imaging assessment of tumors, combining anatomical and metabolic information, represents an attractive approach for mapping the heterogeneity of brain tumors. In fact, the automated classification of multivariate MR data from brain tumor patients is a growing field of research and development. Classification methods based on machine learning tools such as linear

discriminant analysis [McLachlan, 2004], artificial neural networks [Bishop, 1995], and support vector machines [Cortes and Vapnik, 1995; Cristianini and Shawe-Taylor, 2000], have been reported to provide results in agreement with histopathology based on biopsy [McKnight et al., 2002; Alonso et al., 1998]. On the other hand, classification methods based on the combination of imaging and spectroscopy data have shown to be superior to using images or spectroscopy independently [Devos et al., 2005; Simonetti et al., 2005]. Therefore, combining different imaging modalities is an interesting approach to find a multi-parametric fingerprint (pattern) of relapse that does not seem possible using a single modality (Figure 6.1).

The objective of the approach detailed in this chapter is to find a map between the multiparametric MR data acquired before the RT treatment and the site of relapse of the brain tumour. The proposed method relies on the assumption that pre-radiotherapy images contain information that can be used to predict the formation of new contrast-enhancing (CE) regions (indicating potential relapse) after radiotherapy. To this aim, we used a support vectors machine (SVM) [Cortes and Vapnik, 1995; Cristianini and Shawe-Taylor, 2000] classification algorithm to identify regions at risk of relapse in newly diagnosed glioblastoma patients. Our feature space included features from MRI and MRSI. The ground truth used for training the algorithm was defined by images acquired at relapse contoured by experienced medical staff. The results of the proposed classifier were compared with the CNI index [McKnight et al., 2001] (described in Chapter 3, section 3.3.1.3) with an optimal threshold estimated for the cohort of patients.

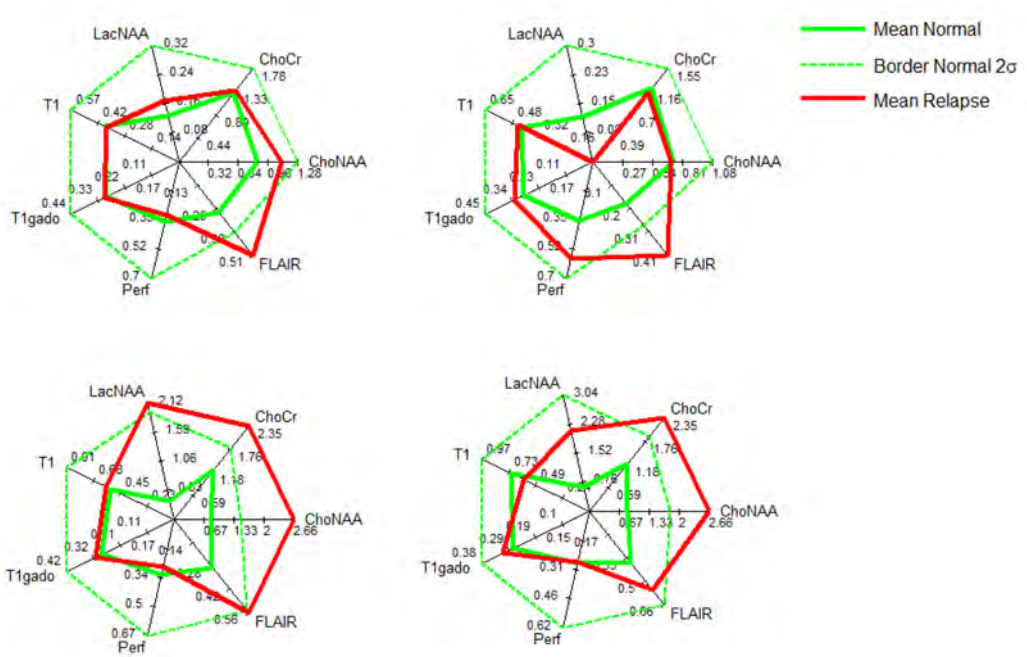


Figure 6.1: Radar charts showing the mean values of different parameters (imaging intensities (FLAIR, T1-weighted before (T1) and after gadolinium injection (T1gado) and perfusion (Perf)) and metabolite ratios) before RT treatment for 4 patients. Data acquired before starting the RT treatment may contain information able to discriminate the site of relapse. Mean values for the voxels lying out of the site of the posterior relapse (green), margin around the normal values (dashed green) ($\sigma$ is the standard deviation of the normal values for each parameter), mean values for voxels lying within the region of relapse (red). For each patient, a different combination of parameters is able to discriminate voxels within the site of relapse from normal tissue.

## 6.3 Used data

### 6.3.1 Patients

The patient database consisted of 10 newly diagnosed GBM patients included in the Spectro-Glio clinical trial described in Chapter 2 (Section 2.5.2.2). All the patients were treated with the reference treatment of 60 Gy, and underwent magnetic resonance imaging (MRI) and MR spectroscopy (MRSI)

before the RT treatment and every 2 months until relapse.

### 6.3.2 Data acquisition

For all patients, MR data acquisition was performed on a 1.5 T Magnetom Avanto Siemens scanner (Erlangen,Germany), with the standard head coil. MRI modalities considered for this study were: fluid attenuated inversion recovery (FLAIR) T2-weighted (TR = 8000 ms, TI = 2400 ms, TE = 105 ms), as well as a T1-weighted (TR= 532 ms, TE= 17 ms) obtained before and after the injection of a standard dose of gadolinium contrast agent (at the rate of 5mL/s).
In vivo MRSI data were acquired using a 3D CSI sequence with water suppression (TE=135 ms, TR =1500 ms, 512 FID data points, 4 averages, slice thickness: 15mm, matrix size: $16 \times 16$, FOV: $160 \times 160$ mm$^2$ yielding a voxel size of $10 \times 10 \times 15$ mm$^3$). The 3D-MRSI box was positioned to cover the majority of abnormalities and normal appearing tissue, while avoiding regions that could corrupt the spectra (such as bone and subcutaneous lipids). Saturation bands were also positioned around the volume of interest (VOI) to suppress signals from excited regions outside the VOI, and to provide good fat suppression.

## 6.4 Relapse prediction

### 6.4.1 Preprocessing

#### 6.4.1.1 Image registration

All the images were registered to the pre-radiotherapy T1-weighted after gadolinium injection (T1-Gd) dataset. The registration was performed using an automatic 3D intensity-based registration algorithm [Gholipour et al., 2007]. The basic principle of intensity-based techniques is to search, in a certain space of transformations, the one that maximizes (or minimizes) a criterion or cost function (metric) measuring the intensity similarity of corresponding voxels [Khunt and Makwana, 2012]. The intensity-based registration algorithm determines iteratively the transformation that is applied to the misaligned volume (moving volume) according to a specified transformation type. The metrics considered in this work were mean squared

difference [Thevenaz et al., 1998; Kybic and Unser, 2003] for monomodal registration, and mutual information [Viola and Wells, 1997; Pluim et al., 2003] for multimodal registration. The geometric transformation applied to the moving volume at each iteration was an affine transformation (consisting of translation, rotation, scale, and shear). The registration algorithm was developed using the functions $imregconfig$ and $imregister$ from the Image Processing Toolbox of Matlab (R2013a). The MRSI spectroscopic grid was assumed to be registered with the T1-Gd images, since they were acquired consecutively. Only voxels within the volume of interest (VOI) of the MRSI box were considered.
The site of relapse was considered as the new appearing CE areas on T1-Gd images, excluding CE before RT (Figure 6.2) or resection cavity for patients without initial CE (Figure 6.3). The regions of CE were manually contoured on both the pre- and post-radiotherapy T1-Gd images by experienced medical staff using the SUMMER prototype.

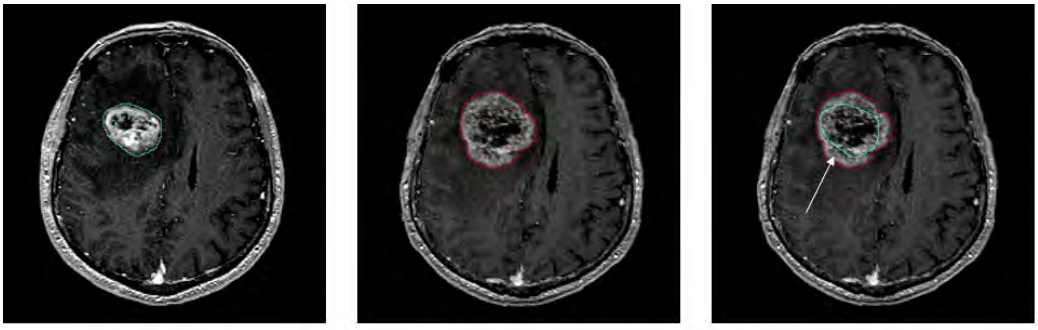

Figure 6.2: Registered T1-weighted images after gadolinium injection of a non-resected patient: pre-RT (left), relapse (middle), site of relapse defined (white arrow) as CE at relapse (red contour) excluding excluding excluding CE before RT (light blue contour) (right).

Preprocessing applied to in vivo MRSI spectra included residual water suppression (using the Hankel singular value decomposition (HSVD) algorithm [Laudadio et al., 2002]), frequency alignment and standard polynomial baseline correction.

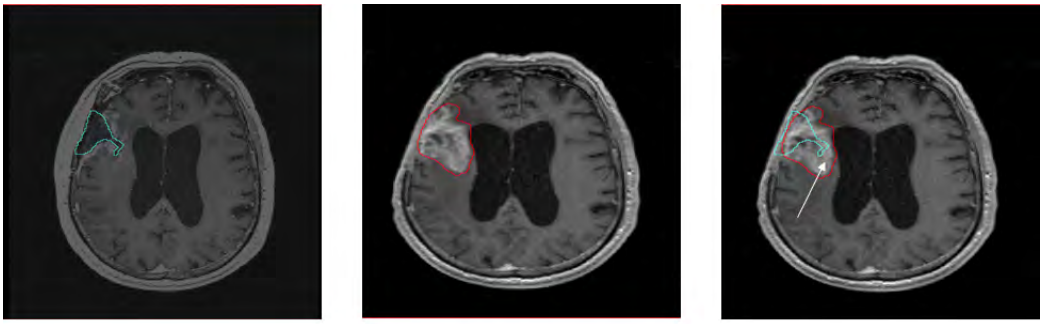

Figure 6.3: Registered T1-weighted images after gadolinium injection of a resected patient: pre-RT (left), relapse (middle), site of relapse (white arrow) defined as CE at relapse (red contour) excluding resection cavity (light blue contour) (right).

### 6.4.2 Feature extraction

Any classification method uses a set of features or parameters to characterize each object to be classified. In our study, the objects are brain regions (voxels) characterized by features derived from the combination of MR imaging and spectroscopic data. Transforming the input data into a set of features is called feature extraction. The set of features used has a big influence in the classification performance, computational efficiency, and results interpretability of the classifier [Nguyen and De la Torre, 2010]. Based on data availability and on previous works combining MRI and MRS(I) data to build classifiers for brain tumor diagnosis [Devos et al., 2005; Luts et al., 2007; Lee and Nelson, 2008], the feature space used in the present study combines intensity values from different MR imaging modalities and metabolic information extracted from MRSI data.

#### 6.4.2.1 MRI features

The intensities from two MRI modalities were considered in this study: T1-Gd and FLAIR. This selection was based in data availability. In order to combine information from MRI and MRSI, the resolution of the MRI images was lowered to the one of the MRSI. This was performed by averaging MRI pixel intensities within each MRSI voxel as proposed in [Simonetti et al., 2003; Luts et al., 2009] (Figure 6.4).

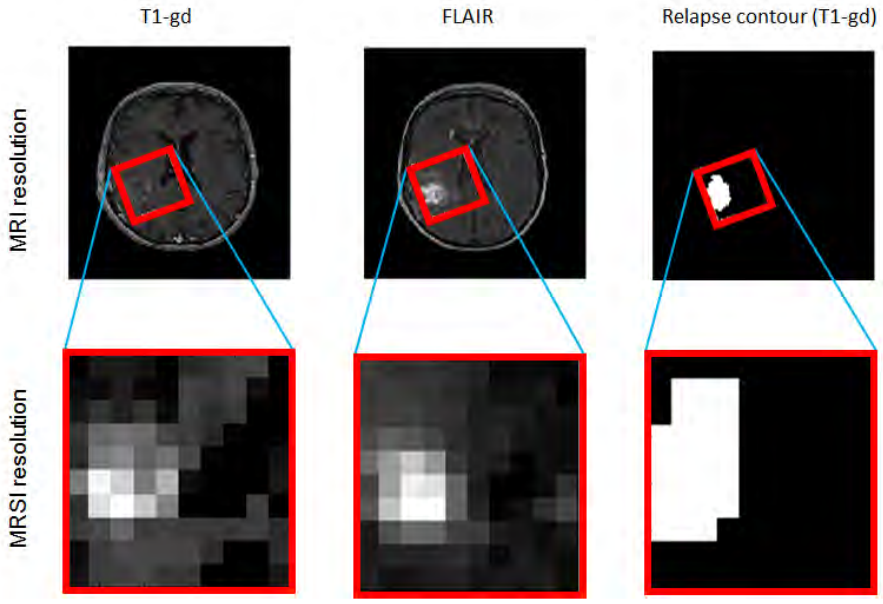


Figure 6.4: The resolution of the MRI images was lowered to the one of the MRSI by averaging MRI pixel intensities within each MRSI voxels. Only voxels within the VOI of the MRSI box (red) were considered.

#### 6.4.2.2 MRSI features

Regarding the spectroscopic data, the full MR spectra can be used as input for the classification method. In that case, all the spectral points are considered as features. Results from previous works on brain tumor diagnosis [Lukas et al., 2004; Menze et al., 2006] suggest that using the full spectrum provides a better performance of the classification algorithms. However, reduction of these features to a smaller number can minimize redundancy and exclude noise and artifacts often present in the spectrum. In addition, the reduction of features can help to improve the performance, decrease the amount of complexity, and simplify the calculation. In this context, quantification can be considered as a feature extraction and dimensionality reduction technique. Additionally, quantification provides a biological interpretation of MR spectra that can be useful to interpret the results. Therefore, MRSI spectra were quantified using the method described in Chapter 5. The spatial and spectral regularization parameters of this method (Equations [5.7] and [5.8]) were both set to 0.05 for all the MRSI datasets. Spectra showing large quan-

tification errors were discarded. The R-square value of the quantification fit was used as criterion [Carpenter, 1960; Draper et al., 1966]:

$$\text{R-square} = 1 - \frac{\sum_{i=1}^{N}(s_i - f_i)^2}{\sum_{i=1}^{N}(s_i - \bar{s})^2}, \qquad [6.1]$$

where $s = [s_1, ..., s_N]$ is the spectrum, $f = [f_1, ..., f_N]$ is the quantification fit and $\bar{s}$ is the mean of the spectrum. R-square can take any value between 0 and 1, with a value closer to 1 indicating a better fitting. Spectra with R-square lower than 0.6 were automatically rejected (Figure 6.5).

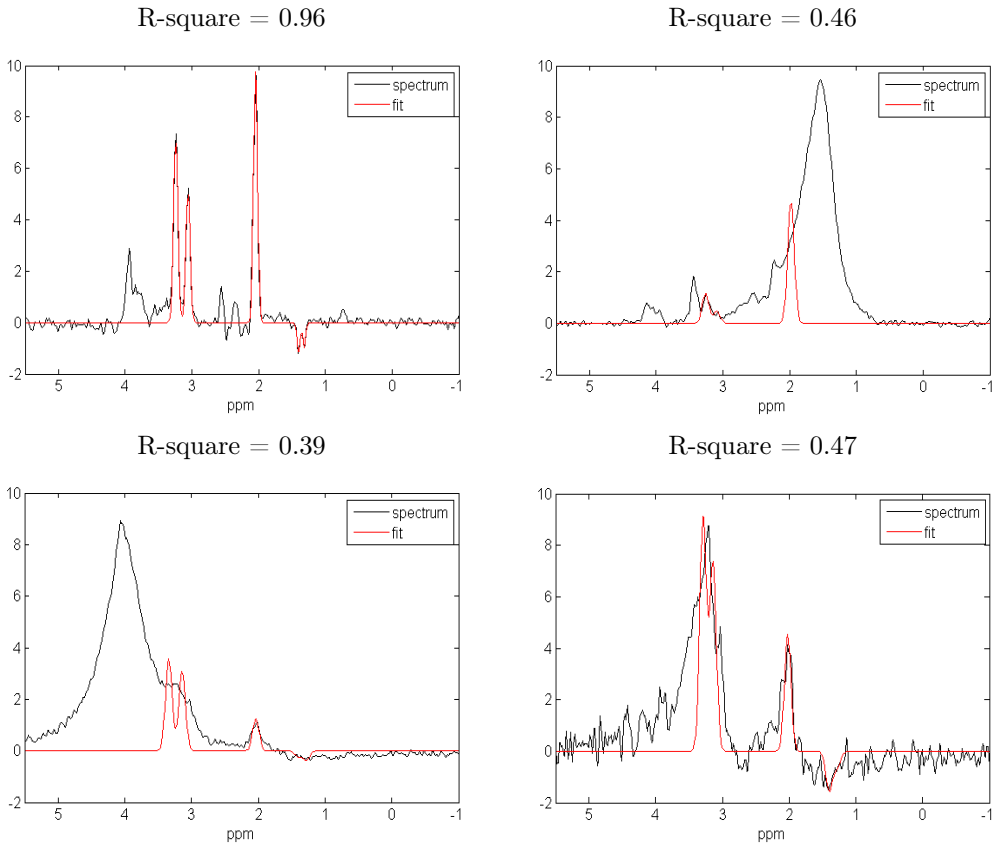


Figure 6.5: Spectrum suitable for quantification (top left); spectra discarded for further analysis due to lipid contamination (top right), water contamination (bottom left) and overlapping Cho and Cr peaks (bottom right).

The peak areas of N-acetyl-aspartate (NAA), creatine (Cr), choline (Cho),

lactate (Lac) and lipids (Lip) were estimated. Metabolite ratios describing the relative levels of Cho to NAA, Cho to Cr and Lac to NAA were also estimated.

#### 6.4.2.3 Spatial correlation

It is well known that MR sequences cause a certain point spread leading to MR signals that are spatially correlated. In the context of MRSI, the slow decay of the point spread function results in cross talk between spectra from adjacent spatial regions. In addition, the information of a MRSI voxel is highly statistically dependent on the values of its neighbors (surrounding voxels) since regional tissue patterns (histopathological classes) normally cover neighbouring voxels. Most classification methods do not incorporate spatial neighborhood information and treat the data as independent observations. Such methods label a voxel based on its feature properties and do not consider spatial correlations between neighboring voxels. In the presence of experimental artifacts, those classifiers can label single voxels with a different class from the neighborhood. Spatial information can help to avoid undesired isolated voxels and to make the edges between different classes more clearly defined. In addition, it may disambiguate the classification problem in case of significant overlap among tissue classes. In fact, it has been shown that properly fusing spectral information with spatial-context information results in an increased robustness to noisy training sets in the learning phase of the classifier [Bruzzone et al., 2007]. In this work, in order to take into account the spatial correlation between neighbouring voxels, the feature set characterizing each MRSI voxel included the values of the features in the surrounding $3 \times 3$ neighborhood (Figure 6.6). The selection of a $3 \times 3$ neighbourhood is based in the fact that the point spread function is usually narrow (the effective voxel size is normally less than 1.5 times the nominal voxel size) [Siemens, 2005].

#### 6.4.2.4 Data normalization

Because SVM algorithms assume that each feature contributes equally to the classification results, all values were normalized between $-1$ and 1. The summary of the all the extracted features is shown in Table 6.1.

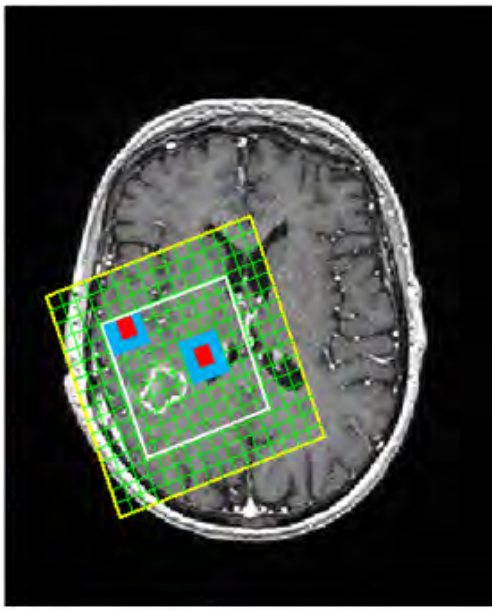

Figure 6.6: Neighbourhood regions (blue) that are taken into account for each voxel (red) in the MRSI grid.

| Image intensities | Metabolite peak areas | Metabolite ratios |
|---|---|---|
| T1-wg Gado<br>FLAIR | Cho<br>Cr<br>NAA<br>Lac<br>Lip | Cho/NAA<br>Cho/Cr<br>Lac/NAA |
| MRI pixel intensities averaged within each MRSI voxel | $3 \times 3$ Neighbourhood | |

Table 6.1: Set of features used for the classification.

### 6.4.3 Support Vectors Machine

Using as input the set of features extracted from pre-treatment multi-parametric MR data as described above, a supervised learning system based on support vector machines (SVM) was trained to generate a probability map of relapse for GBM patients. SVM [Cortes and Vapnik, 1995; Cristianini and Shawe-Taylor, 2000] is among the most popular machine learning techniques because it is easy to understand and to interpret. SVM-based classifiers have shown

to provide good performances in previous works in the context of multiparametric MR data [Devos et al., 2005; Luts et al., 2007]. The basic idea behind support vector machines is illustrated with the example shown in Figure 6.7. Given a training set with points (samples) that belong to two classes, it finds the best hyperplane to differentiate between the two types of points (classes) (i.e. the distance between the hyperplane and the closest training points is maximized). In this example the data is assumed to be linearly separable. Therefore, there exists a linear hyperplane (or decision surface) that separates the points into two different classes. In the two-dimensional case, the hyperplane is simply a straight line. The minimal distance from the separating hyperplane to the closest training point is called margin. The training samples that lie on the margin define the border between the two classes and are referred to as support vectors.

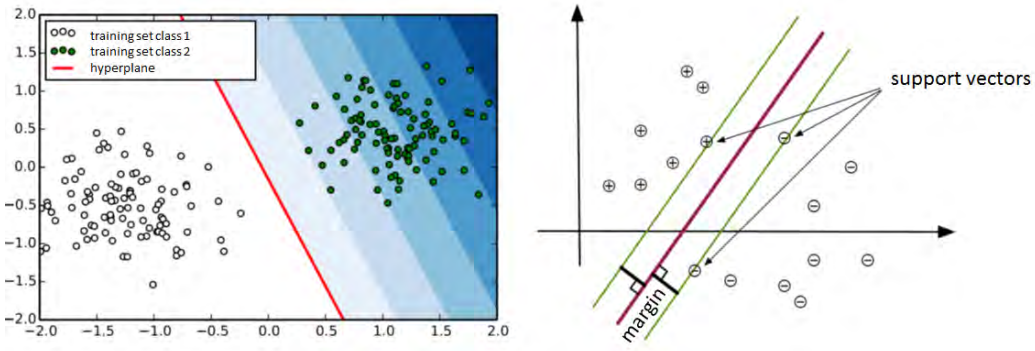


Figure 6.7: Given a linearly separable training set, SVM finds the best hyperplane (straight line in the two-dimensional case) that differentiate the two classes (left). The minimal distance from the separating hyperplane to the closest training point is called margin. The training samples that lie on the margin are referred as support vectors (right).

If training data are not linearly separable in the original space, they can be mapped to a higher dimensional space by using what is called a kernel function. By employing kernel transformations to map the samples from their original space into a higher-dimensional feature space, SVM can separate objects which are not linearly separable (Figure 6.8). Kernel-based techniques are less sensitive to the amount of data and the input dimension than other methods (like K-Nearest Neighbour [Samadzadegan et al., 2010] or Linear Discriminant Analysis [Devos et al., 2005]) and are able to detect automat-

ically important characteristics independently of the input pattern [Devos et al., 2005].

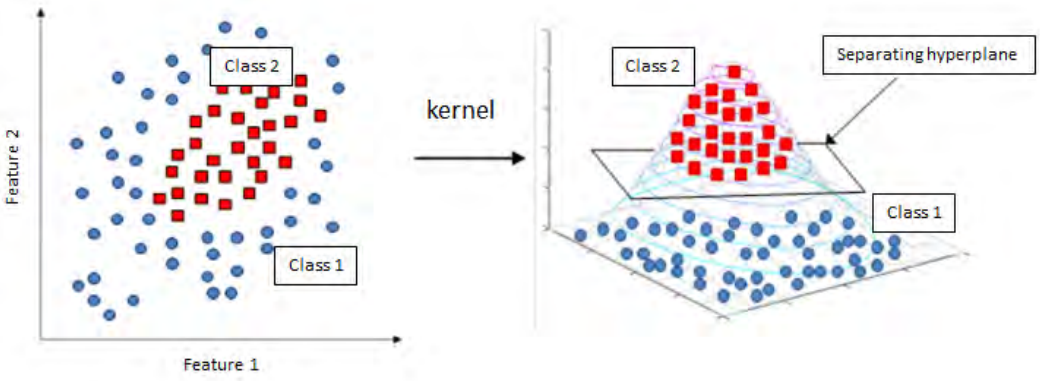


Figure 6.8: The kernel function transforms the data into a higher dimensional space to make it possible to perform the separation. Edited from [Statnikov et al., 2011].

#### 6.4.3.1 Kernel selection and parameters tuning

Several kernels can be used to map the input features into a higher-dimensional space, according to the nature of the data. The performance of the SVM algorithms closely depends on the kernel function and its corresponding parameters. The most widely used kernels includes linear, polynomial and radial basis (RBF) functions. In this study, we used the RBF kernel because non-linear techniques may improve the classification performance [Suykens and Vandewalle, 1999], and they have shown to provide better classification accuracy than other kernel functions in previous works [Devos et al., 2005; Luts et al., 2007]. In addition, it is worth noticing that the linear kernel is a special case of RBF kernel. A second reason to use this kernel is the number of hyperparameters which influences the complexity of model selection, which is lower than with other non-linear kernels, such as the polynomial kernel.
There are two parameters that can be tuned in the RBF kernel and which depend on the input data: a parameter which determines the trade-off between minimizing the training errors and minimizing the model complexity

(C) (a small value for C means the margin is calculated using many or all of the observations around the separating line (more regularization); a large value for C means that the margin is calculated on observations close to the separating line (less regularization)), and the radius (or width) of the kernel ($\gamma$). The performance of the SVM classifier strongly depends on the choice of these parameters. Different techniques have been proposed to estimate the optimal parameters for an RBF kernel [Chapelle et al., 2002; Ayat et al., 2002; Ahn, 2010]. In this study we have considered two well-known approaches: a grid-search strategy [Hsu et al., 2003] and the Jaakkola's heuristic [Jaakkola et al., 1999]. More details about these methods and their application to our data can be found in the next Section 6.5.

## 6.5 Results

In order to build an optimal classifier for our data, a grid-search strategy was employed to find the optimal parameters (C and $\gamma$) of the RBF kernel. To this aim, we performed a two-dimensional grid search over the possible values of the parameters C and $\gamma$. A coarse grid search was initially conducted (Figure 6.9). After identifying the best region on the grid, a finer grid search on that region was performed. For each combination of the parameters, the SVM method was trained and tested using leave-one-out-cross-validation (LOOCV). LOOCV is a simple cross-validation in which each training set is created by taking all the samples except one, and the test set is the sample left out. Thus, for $n$ samples, we have $n$ different training sets and $n$ different test sets. The optimal parameters were selected based on the accuracy (area under the curve), sensitivity and specificity. For patients in the conventional arm of the trial, the optimal values empirically estimated for C and $\gamma$ were 1 and 0.025, respectively. The publicly available library *libsvm* [Chang and Lin, 2011] was used to perform the SVM-based classification. More precisely, the two-class C-support vector classification (C-SVC) formulation was used [Boser et al., 1992; Cortes and Vapnik, 1995]. This formulation has an extension to provide probability estimates [Platt, 2000; Wu et al., 2004; Lin and Weng, 2004] (to generate the probability maps). The output of the classifier are then class probabilities. This means that instead of binary output scores (0 for "no relapse" and 1 for "relapse") we get probability values for each class.
We compared the results from the SVM method (using the estimated optimal

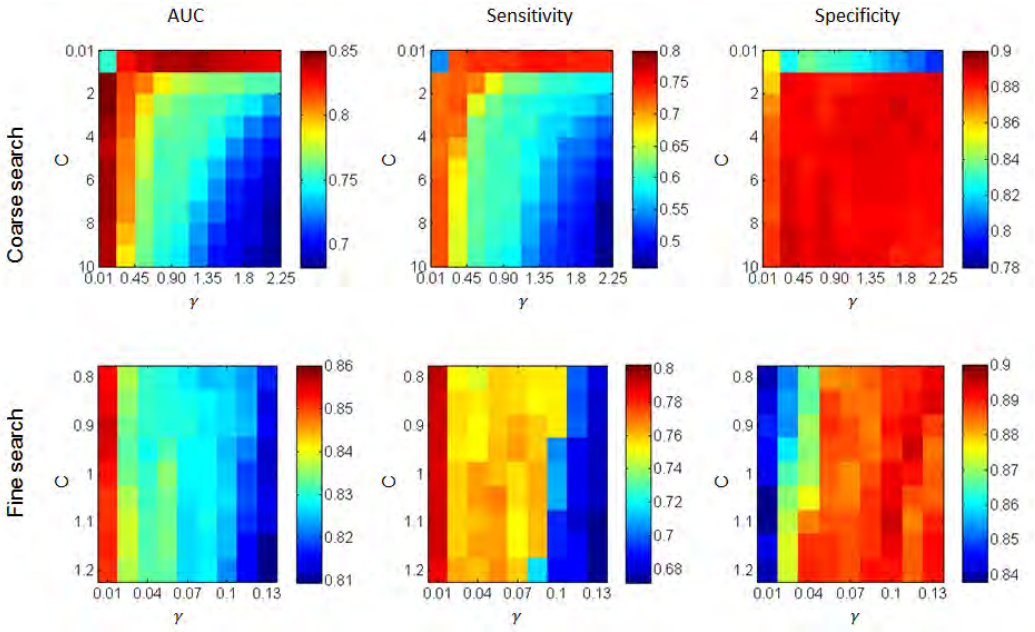


Figure 6.9: Optimal parameter selection. A coarse (top) and fine (bottom) grid search is performed to find the optimal hyperparameters C and $\gamma$ for the RBF kernel. A balance between accuracy, sensitivity and specificity is employed for the decision of the parameters.

parameters) with the standard CNI index described in Section 3.3.1.3 [McKnight et al., 2001]. For comparison purposes, the probability maps generated with the SVM approach were thresholded with a value of 0.5. Thus, only voxels with values higher than 0.5 on the probability map were considered to predict the site of relapse. As the classes might be unbalanced (there are much less voxels that relapse than voxels that do not relapse), it is more appropriate to use the sensitivity (the ratio of true positives and the sum of true positives and false negatives) and the specificity (the ratio of true negatives and the sum of false positives and true negatives) as performance measures [Luts et al., 2007] (see Figure 6.10).
The sensitivity and specificity of the proposed method were 0.80 ($\pm$0.19) and 0.87 ($\pm$0.09), respectively. The optimal threshold for the CNI index was estimated (for all the cohort of patients) from the receiver operating characteristic (ROC) curve [Swets, 1988] (Figure 6.11). A ROC curve is a plot of the sensitivity or true positive rate (TPR) (on the y-axis) versus (1

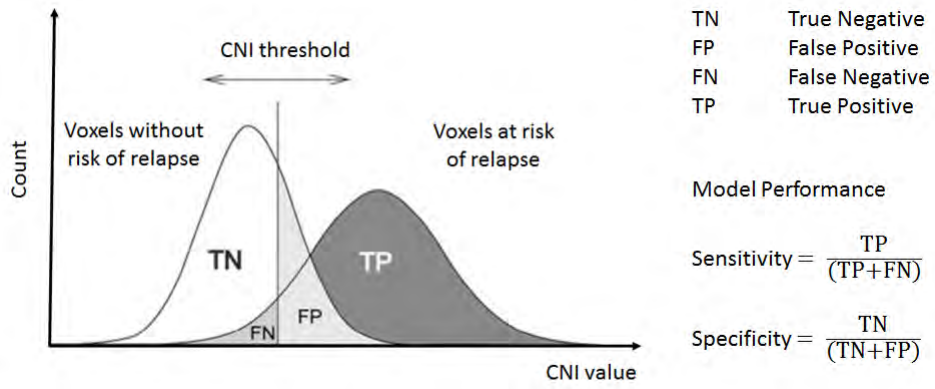


Figure 6.10: One of the most important tasks of ROC analysis is the determination of the optimal cutoff value. If the position of the threshold is varied, sensitivity and specificity are also changed. Edited from [Vranova et al., 2009].

- specificity) or false positive rate (FPR) (on the x-axis) for different cut-off points of a parameter (CNI in this case) (Figure 6.11).
As it can be seen in Figure 6.11, the optimal CNI threshold was estimated using three different methods. The conventional "minimum distance" approach assumes that the best cut-off is the point on the ROC curve closest to the (0,1) point, i.e. high up on the left-hand side of the graph (where sensitivity=1 and specificity=1). The CNI threshold estimated by this approach was 1.78, and the corresponding sensitivity and specificity values were 0.56 ($\pm$0.25) and specificity 0.72 ($\pm$0.13). The Youden index assigns the cut-off value to the point on the ROC curve for which the sum (sensitivity + specificity) is maximal [Youden, 1950; Reiser, 2000]. The CNI threshold obtained using this method was 2.67, and the corresponding sensitivity and specificity values were 0.38 ($\pm$0.23) and specificity 0.94 ($\pm$0.14). In order to find the CNI threshold that maximizes and balances simultaneously the specificity and the sensitivity, the point on the ROC curve for which the sum (sensitivity + specificity) is maximal and the difference $|(\text{sensitivity} - \text{specificity})|$ is minimal was estimated. The CNI threshold obtained using this method was 1.55, and the corresponding sensitivity and specificity were 0.62 ($\pm$0.25) and a specificity of 0.63 ($\pm$0.13). Table 6.2 summarizes the results form the proposed method and the CNI index.

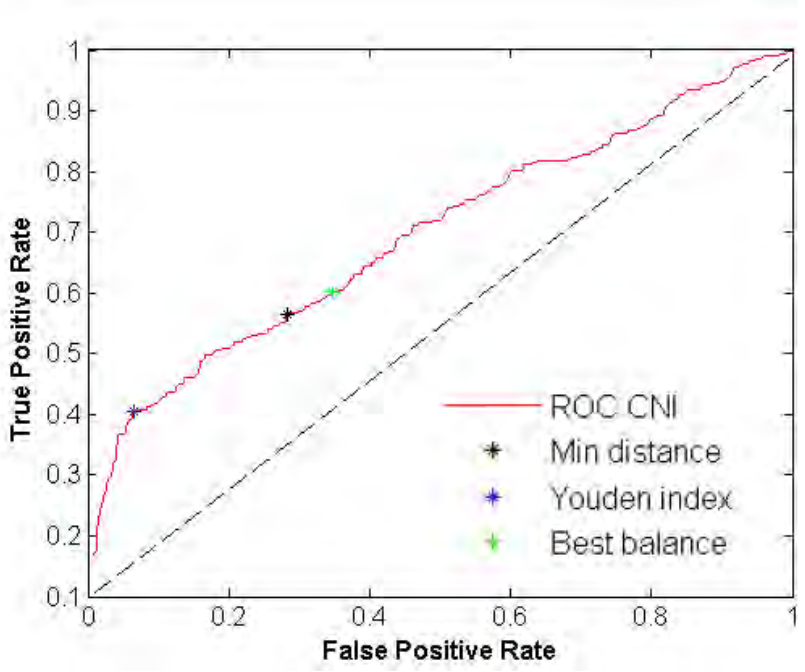


Figure 6.11: Receiver operating characteristic (ROC) curve for standard CNI approach. The optimal cut-off points estimated using different methods are displayed.

| | Threshold | Sensitivity | Specificity | AUC |
|---|---|---|---|---|
| Minimum distance | 1.78 | 0.56 (±0.25) | 0.72 (±0.13) | |
| Youden | 2.67 | 0.38 (±0.23) | 0.94 (±0.14) | 0.70 (±0.16) |
| Balanced | 1.55 | 0.62 (±0.25) | 0.63 (±0.13) | |
| SVM | - | 0.80 (±0.19) | 0.87 (±0.09) | 0.92 (±0.09) |

Table 6.2: Performances of the CNI method and the proposed SVM-based approach.

The proposed method provides higher sensitivity than the standard CNI approach for all the CNI thresholds analyzed. The specificity is also better except for the CNI threshold estimated using the Youden index approach. However, the high specificity for the CNI index in this case (0.94 ±0.14) is related to a very low sensitivity (0.38 ±0.23). The ROC curves in Figure 6.12

show that the presented approach also outperforms CNI in terms of accuracy since it has a significantly higher area under the curve (AUC). In addition, the proposed method is more robust across patients as demonstrated by the lower variances for the accuracy, sensitivity and specificity. An example of a probability map of relapse areas generated by the proposed approach is shown in Figure 6.13. As it can be seen, relapse regions predicted by the SVM-based method are in high accordance with the manually contoured region.

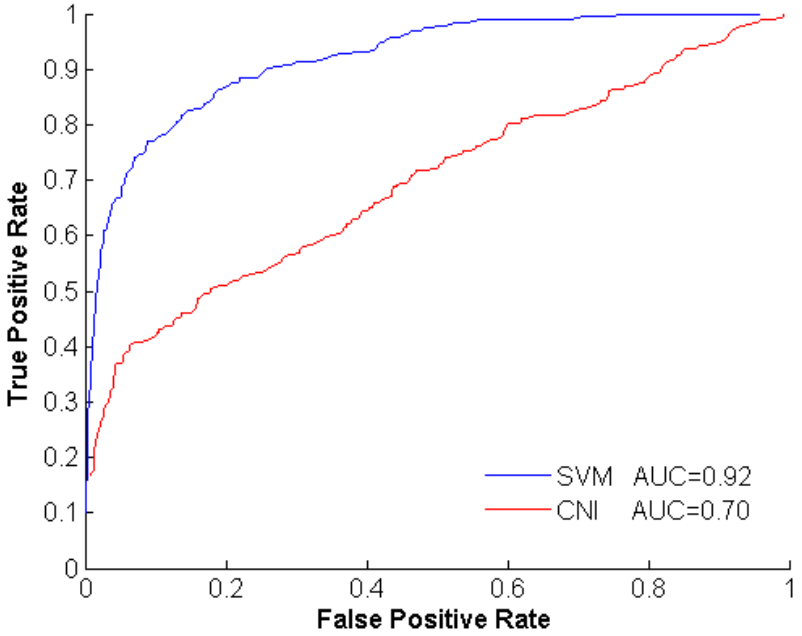


Figure 6.12: Receiver operating characteristic (ROC) curves for the proposed method (blue) and for the standard CNI approach (red). The corresponding areas under the curve (AUC) are also displayed.

The bar plot in Figure 6.14 clearly shows that the combined use of MRI and MRSI improves the performance of the classifier. The results obtained using the CNI method are also displayed for comparison purposes.

It is worth noting that SVM methods predict only class labels without probability information. In this study we have used an extension to derive class probability estimates [Platt, 2000; Wu et al., 2004; Lin and Weng, 2004;

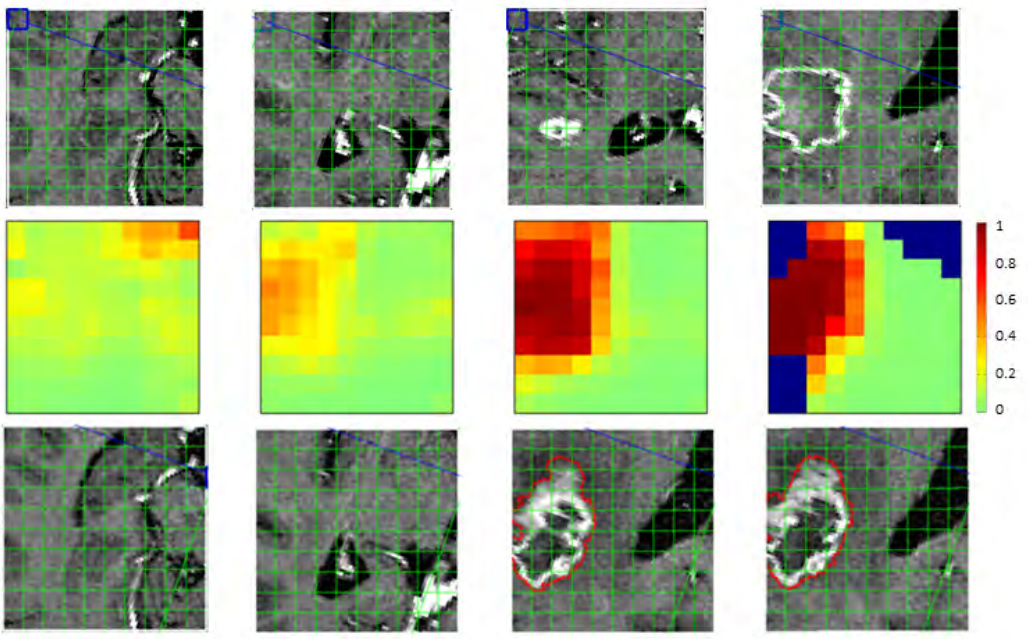


Figure 6.13: Pre-RT T1-Gd (top), probability maps of GBM relapse generated by the proposed approach (middle) and reference manual contours of the relapse for a given patient (bottom). Each slice represents a slice in the axial view. Dark blue on the probability maps indicate voxels where metabolic information was not available. The areas at risk of relapse predicted by the proposed approach (using MR data acquired before RT) are in clear accordance with the manually contoured relapse regions.

Chang and Lin, 2011]. Alternatively, regression approaches like ridge logistic regression or elastic net could have been also considered. Logistic regression and elastic nets perform pretty similar than traditional linear SVMs [Gareth, 2013]. However, logistic regression also allows kernel extensions [Zhu and Hastie, 2012], and elastic net regularization can be combined within the SVM method in order to perform feature selection with SVM classification. In addition, elastic nets can be helpful in classification problems where the number of features is much higher than the number of obervations, and where features are highly correlated. However, compared to these approaches, more efficient and well documented libraries are available for SVM approaches. It is relevant to mention here that, recently, it has been shown that any elas-

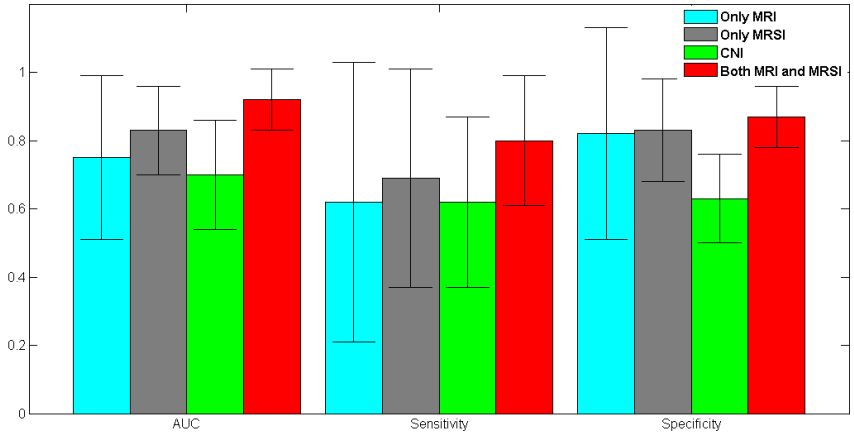


Figure 6.14: The combined use of image intensities and spectroscopic information improves the accuracy of the classifier.

tic net regression problem can be reduced to SVM classification Zhou et al. [2015]. Therefore, elastic net problems can be efficiently solved using the existing optimized SVM algorithms to obtain a highly optimized solver for the elastic net.

## 6.6 Conclusion

A learning system based on SVM trained with multi-parametric MR data has been presented. Reported results imply that this learning scheme can provide probability maps indicating the areas of relapse of GBM. This study has shown that, in comparison with single-variable classifiers like the CNI index, it is possible to increase the cross-patient robustness by using a multi-parametric set of features through machine learning techniques. The results suggest the potential of multi-parametric MR data in addressing specific questions in GBM management. A key finding of this study, from the tumor biology perspective, is that metabolic features in the pre-treatment scan appear to provide relevant information to predict the tumor relapse. Future work includes the assessment of the method with a larger cohort of patients and the integration of other imaging modalities. Combining dimension reduction techniques with SVM classifiers can also be considered in order to

improve the classification performance. The integration of the RT dose into the features space would be an interesting approach to be addressed in future works.

# Chapter 7

# MRSI unmixing

## Contents



## 7.1 Introduction

As shown in Chapter 5, quantification is the conventional method to extract information from MRSI data. Quantification results are influenced by the presence of artifacts in the data and the choice of the quantification algorithm. Therefore, alternative approaches to interpret MRSI data are emerging. This chapter describes a novel spectral unmixing algorithm for brain tissue classification and visualization of tumor spread using MRSI data [Laruelo et al., 2016a]. Different experiments with in-vivo MRSI data are shown to demonstrate the ability of the algorithm to extract physically meaningful patterns and its robustness against the presence of low quality spectra.

## 7.2 Motivation

Conventional magnetic resonance imaging (MRI) is widely used for the diagnosis and follow-up of brain tumors due to its ability to provide detailed information about brain structures. Nevertheless, MRI does not always have sufficient specificity to identify different pathological areas in heterogeneous brain tumors. MR spectroscopic imaging (MRSI) helps to overcome this limitation as it is able to characterize biochemical changes in brain tissues before they become visible in conventional MRI [Laprie et al., 2008; Deviers

et al., 2014]. The existence of areas with different metabolic profiles leading to different treatment response have been reported in previous studies. $^{1}$H MRSI has been proved to highlight the metabolically active areas of the tumor in high-grade gliomas [McKnight et al., 2002; Pirzkall et al., 2004]. This metabolic tool is also able to characterize hypoxic areas associated with a poorer response to radiotherapy treatments [Deviers et al., 2014]. On the other hand, many studies have reported metabolic evidence of microscopic tumor activity/infiltration beyond the borders of the contrast-enhancing lesions and lesions appearing as hyperintense on T2-weighted MR images of both patients with recurrent and newly diagnosed gliomas [Patel et al., 1999; Burtscher et al., 2000; Graves et al., 2000; Pirzkall et al., 2001]. The results from these studies demonstrate that, on average, one third to one half of the non-enhancing regions of malignant glioma contain active tumor that, if left untreated, may have a negative impact on patient survival [McKnight et al., 2002]. Therefore, the ability to identify different metabolic tumor areas and tumor activity in the nonenhancing regions is crucial for the management of most brain tumors.

Supervised pattern recognition methods relying on known spectral models have been widely used to discriminate between brain tissue types. However, the outcome of these methods strongly depends on the prior knowledge considered and the algorithm used [Mosconi et al., 2014b]. In addition, supervised methods require a large number of expert-labeled spectra which are not always available. Blind source separation (BSS) techniques appear as an interesting alternative for the analysis of MRSI data as they allow to estimate the sources and their abundances without (or with very little) prior knowledge. Different BSS methods have been proposed in the context of neuro-oncology to distinguish normal from abnormal spectra. Most of these methods are variants of the well-known non-negative matrix factorization (NMF) algorithm [Lee and Seung, 1999]. Sajda *et al.* [Sajda et al., 2004] proposed a constrained non-negative matrix factorization method to extract physically meaningful tissue patterns from long-echo time (TE) MRSI data. Ortega-Martorel *et al.* [Ortega-Martorell et al., 2012] used convex NMF for brain tumor delineation on pre-clinical data. Li *et al.* [Li et al., 2013] introduced a hierarchical NMF method able to identify normal, tumor and necrosis tissues in glioblastoma (GBM) patients. All these methods are heavily dependent on the initialization values and/or require the sources to be non-negative. The use of non-negative sources can be a clear limitation for the analysis of MRSI data given that MR spectra can take negative values (such

as the inverted lactate peak for long-TE data.)
Recently, BSS methods exploiting not only the spectral but also the spatial context of the signals have been proposed [Gillis, 2012]. These algorithms incorporate spatial priors based on smooth spatial variations or on the sparsity of the abundance matrix. In this chapter we describe a method which jointly incorporates prior knowledge about the spatial and spectral dimensions of MRSI data. The originality of this method lies in the combination of spectral and spatial priors in a transformed domain into a spectral unmixing procedure, as well as the control of the non-negativity constraint for the sources. It aims at increasing the signal-to-noise ratio (SNR) of the data and favoring solutions with few irregularities in the spatial and the spectral dimensions. The proposed method is able to extract more than two physically meaningful tissue patterns and it is not restricted to non-negative sources. In addition, the convergence to a global optimal solution is guaranteed since this algorithm relies on the optimization of convex functions. Furthermore, it is robust to noise and to the presence of low quality spectra.

## 7.3 Blind Source Separation

BSS methods assume that the measurements (spectra) can be expressed as linear mixtures of sources plus some noise. This can be expressed in matrix form as follows:

$$\boldsymbol{Y} = \boldsymbol{S}\boldsymbol{A} + \boldsymbol{N}, \qquad [7.1]$$

where $\boldsymbol{Y} \in \mathbb{R}^{M \times R}$ is the data matrix in which each column is a measurement (real or magnitude spectrum) involving $M$ spectral points and $R$ spatial positions, $\boldsymbol{S} \in \mathbb{R}^{M \times K}$ is the unknown source matrix in which each column is a source, $\boldsymbol{A} \in \mathbb{R}^{K \times R}$ is the unknown mixing matrix which defines the contribution (abundance) of each source in each spatial position (voxel) and $\boldsymbol{N}$ is the unknown noise matrix accounting for instrumental noise and/or model imperfections. Note that the sources matrix $\boldsymbol{S}$ in equation [7.1] is equivalent to the matrix $\boldsymbol{B}$ in equation [5.3] of Chapter 5. However, while $\boldsymbol{B}$ is a known matrix in Chapter 5, in the current problem [7.1] $\boldsymbol{S}$ needs to be estimated together with the abundances matrix $\boldsymbol{A}$.
BSS methods aim at estimating both $\boldsymbol{A}$ and $\boldsymbol{S}$ from the measured data $\boldsymbol{Y}$. Under the assumption of independent and identically distributed (i.i.d.)

Gaussian noise, the maximum-likelihood estimator is defined by the standard problem:

$$(\widehat{S}, \widehat{A}) = \arg\min_{\boldsymbol{S},\boldsymbol{A}} \frac{1}{2}\|\boldsymbol{Y} - \boldsymbol{S}\boldsymbol{A}\|_2^2. \quad [7.2]$$

The problem [7.2] is ill-posed in the sense that it has an infinite number of solutions. In order to find an optimal solution of [7.2] it is standard to constrain $\boldsymbol{A}$ and/or $\boldsymbol{S}$ to privilege solutions with desired properties. These constraints can be seen as prior information injected in the resolution of [7.2]. The following sections describe the priors used in this work.

### 7.3.1 Spectral prior

In many applications, sources are considered sparse as for the case for MRSI spectra. In the wide sense, a sparse signal is a signal that can be expressed with only few non-zero coefficients, or can be well approximated in such a way. The sparsity of the sources can be enforced by constraining their $\ell_1$ norm, which leads to the following optimization problem:

$$(\widehat{S}, \widehat{A}) = \arg\min_{\boldsymbol{S},\boldsymbol{A}} \frac{1}{2}\|\boldsymbol{Y} - \boldsymbol{S}\boldsymbol{A}\|_2^2 + \alpha_1\|\boldsymbol{S}\|_1, \quad [7.3]$$

where $\alpha_1 \in \mathbb{R}_+$ controls the trade-off between data fidelity and prior information. In order to better model this kind of signals, one can express them in a different domain where the sparsity is more noticeable. In this chapter, we exploit the fact that the sources are sparse in the wavelet domain leading to the following problem:

$$(\widehat{S}, \widehat{A}) = \arg\min_{\boldsymbol{S},\boldsymbol{A}} \frac{1}{2}\|\boldsymbol{Y} - \boldsymbol{S}\boldsymbol{A}\|_2^2 + \alpha_1\|T\boldsymbol{S}\|_1, \quad [7.4]$$

where $T$ is a dyadic 1D orthonormal wavelet decomposition operator.

### 7.3.2 Spatial prior

As shown in Chapters 4 and 5, recent methods to process MRSI data incorporate not only the spectral, but also the spatial context of the signals by incorporating spatial priors [Nguyen et al., 2010; Sava et al., 2011; Kelm et al., 2012; Laruelo et al., 2013a]. MRSI signals are no longer processed individually but the intrinsic spatio-spectral nature of the data is exploited by taking

advantage of the correlations between spatial and spectral neighbors. Following this idea, some BSS methods have targeted the integration of contextual information to guide the sources extraction and/or the abundances estimation steps. Previous BSS methods favor smooth spatial variations or spatial sparsity by imposing appropriate constraints on the mixing-matrix $\boldsymbol{A}$ [Kim and Haesun, 2008; Moudden et al., 2009; Gillis and Plemmons, 2012]. We propose a novel spatial prior which, together with the spectral term, increases the signal-to-noise ratio (SNR) of the data and exploits the neighbouring information along the spatial dimension for a given MRSI voxel. The proposed criterion to be minimized can be written as follows:

$$\arg\min_{\boldsymbol{S},\boldsymbol{A}} \frac{1}{2}\|\boldsymbol{Y}-\boldsymbol{S}\boldsymbol{A}\|_2^2+\alpha_1\|T\boldsymbol{S}\|_1+\alpha_2\sum_{m=1}^{M}\|F(\boldsymbol{S}A)^m\|_1, \qquad [7.5]$$

where $\alpha_2 \in \mathbb{R}_+$ is the regularization parameter of the spatial prior information, $m = 1, ..., M$ is the spectral frequency, $(\boldsymbol{S}\boldsymbol{A})^m$ is the 2D image which results from reshaping the m$th$ column of $\boldsymbol{S}\boldsymbol{A}$ and $F$ is a dyadic 2D orthonormal wavelet decomposition operator.

### 7.3.3 Non-negativity constraints

The entries of both the abundances $\boldsymbol{A}$ and the sources $\boldsymbol{S}$ are often assumed to be non-negative. This is always true for $\boldsymbol{A}$ since the mixture coefficients are function of the relative concentrations of the observed physical entities, which are necessarily non-negative. However the non-negativity assumption does not always hold for MRSI spectra that may include negative peaks (as it is the case of the inverted lactate peak for long-TE MRSI data). BSS methods based on NMF are limited to use absolute or truncated spectra (negative values set to zero). In order to avoid this limitation, we propose to relax the non-negativity constraint for the matrix of extracted sources as follows:

$$\begin{aligned}(\widehat{S},\widehat{A}) = \arg\min_{\boldsymbol{S},\boldsymbol{A}} \frac{1}{2}\|\boldsymbol{Y}-\boldsymbol{S}\boldsymbol{A}\|_2^2+\alpha_1\|T\boldsymbol{S}\|_1+\alpha_2\sum_{m=1}^{M}\|F(\boldsymbol{S}A)^m\|_1 \\ + i^+(\boldsymbol{A})+\alpha_3 i^+(\boldsymbol{S}), \qquad [7.6]\end{aligned}$$

where $i^+$ is the indicator function of the non-negative half line $\mathbb{R}_+ = [0, +\infty)$, and $\alpha_3 \in \{0, 1\}$ allows the relaxation of the non-negativity constraint of the

sources. The indicator function of the non-negative half-line $\mathbb{R}_+$ is defined as:

$$i^+(x) = \begin{cases} 0, & \text{if } x \geq 0; \\ +\infty, & \text{otherwise.} \end{cases}$$

### 7.3.4 Optimization procedure

The minimization of the objective function [7.6] can be carried out solving alternately the convex subproblems with respect to $\boldsymbol{A}$ and $\boldsymbol{S}$. However the objective functions of both sub-problems are not differentiable, which prevents the use of standard gradient-based algorithms for minimization. We therefore propose to perform the minimization by using proximal splitting methods [Combettes and Pesquet, 2008, 2011; Pustelnik et al., 2011] that, as it has been shown in previous chapters (Chapter 4 and Chapter 5), have already been successfully used in a number of recent works in convex optimization [Chaari et al., 2011]. Proximal splitting methods aim at minimizing convex functions which are not differentiable. The idea of these methods is to split the cost function into the sum of several convex functions which are alternately locally minimized. The marginal problem in $\boldsymbol{S}$ is a convex functional that can be split into the sum of a convex smooth and two convex non-smooth terms:

$$\widehat{S} = \arg\min_{\boldsymbol{S}} \frac{1}{2}\|\boldsymbol{Y} - \boldsymbol{S}\boldsymbol{A}\|_2^2 + \alpha_1\|T\boldsymbol{S}\|_1 + \alpha_3 i^+(\boldsymbol{S}). \qquad [7.7]$$

The smooth part of the objective function is the data fidelity term:

$$D(\boldsymbol{S}) = \frac{1}{2}\|\boldsymbol{Y} - \boldsymbol{S}\boldsymbol{A}\|_2^2, \qquad [7.8]$$

where $D$ is differentiable and its gradient $\nabla D(\boldsymbol{S}) = (\boldsymbol{S}\boldsymbol{A} - \boldsymbol{Y})\boldsymbol{A}^T$ is L-Lipschitz with $L = \|\boldsymbol{A}\boldsymbol{A}^T\|_2$. On the other hand, the proximity operator of the sum of the two non-smooth terms has an explicit form:

$$\text{prox}_{\alpha_1\|T.\|_1 + \alpha_3 i^+(.)}(x) = \left[\text{sign}(x)[|x| - \alpha_1]_+\right]_+, \qquad [7.9]$$

where $[x]_+ = \max(x, 0), \forall x \in \mathbb{R}$. Therefore, the problem [7.7] can be solved using a well known proximal splitting algorithm: the forward-backward splitting algorithm (FBS) [Combettes and Pesquet, 2008]. However, we propose

to solve the marginal problem in $\boldsymbol{S}$ by using the generalized forward-backward (GFB) algorithm [Raguet et al., 2013] that is able to to cope with more than one non-smooth terms. Using this approach, we can switch on and off any of the terms (set $\alpha_3 = 0$ to allow sources with negative peaks for example), or to keep the flexibility of incorporating other regularizations as, for example, $\|T\boldsymbol{S}\|_p$ with $p > 1$. The use of the GFB algorithm also keeps open the possibility of incorporating more terms in the criterion [7.7], since it is among the first algorithms able to deal with more than one non-smooth regularization terms.

In the case of the subproblem in $\boldsymbol{A}$, the term $\alpha_2 \sum_{m=1}^{M} \|F(\boldsymbol{S}A)^m\|_1$, where the non-smooth convex function $\|.\|_1 \circ F$ is evaluated on the product of the the matrix $S$ by the sought solution $A$, prevents us to consider in this case the GFB algorithm used to solve the subproblem in $\boldsymbol{S}$. We propose to solve the minimization problem with respect to $\boldsymbol{A}$ using the simultaneous direction method of multipliers (SDMM) described in [Combettes and Pesquet, 2008] and already introduced in Chapter 5.

Using these algorithms to solve the subproblems in A and S, we can now solve the unmixing problem [7.6] by alternating the updates of $\boldsymbol{A}$ and $\boldsymbol{S}$ for a number of iterations. The steps of the proposed unmixing algorithm are described in Algorithm 3.

**Algorithm 3 BSS Algorithm**

Set $N, T, F, \alpha_1, \alpha_2, \alpha_3$
  Set NbSources $= VCA(\boldsymbol{Y})$
  Set $\boldsymbol{A}_0 = abs(randn(\text{NbSources}, \text{NbSpectra}))$
  **for** $n = 1$ to $N$ **do**
    Set $\boldsymbol{A}^{-1} = pinv(\boldsymbol{A}_{n-1})$
    Set $\boldsymbol{S}_{n-1} = \boldsymbol{Y} * \boldsymbol{A}^{-1}$
    Calculate $\boldsymbol{S}_n = GFB(\boldsymbol{Y}, \boldsymbol{A}_{n-1}, \boldsymbol{S}_{n-1}, T, \alpha_1, \alpha_3)$
    Calculate $\boldsymbol{A}_n = SDMM(\boldsymbol{Y}, \boldsymbol{A}_{n-1}, \boldsymbol{S}_{n-1}, F, \alpha_2)$
  **end for**
  **return** $\boldsymbol{S} = \boldsymbol{S}_N$
  Normalize columns of $\boldsymbol{A}_N$.
  **return** $\boldsymbol{A} = \boldsymbol{A}_N$

## 7.4 Results

We have tested the proposed method on in-vivo MRSI data from 10 patients with newly diagnosed GBM included in the prospective clinical trial SpectroGlio (see Chapter 2, Section 2.5.2.2). We show the results for different representative cases: identification of intratumoral necrotic areas, discrimination of necrosis and hypoxia and detection of tumor infiltration. The locations of the tissue patterns were confirmed by experienced research staff involved in the clinical trial. Data were acquired with a Siemens Avanto 1.5 T using a 3D CSI sequence with water suppression, echo time (TE) of 135 ms, repetition time (TR) of 1500 ms, 512 data points and 4 averages.
Preprocessing applied to in vivo MRSI spectra included residual water suppression (using the Hankel singular value decomposition (HSVD) algorithm [Laudadio et al., 2002]), frequency alignment and standard polynomial baseline correction. The spectra were normalized to the same intensity scale, with one being the maximum (absolute) peak intensity for every spectrum. This was accomplished by dividing all spectrum intensities by the absolute maximum value.
We have used Vertex Component Analysis (VCA) [Nascimento and Bioucas Dias, 2005] to estimate the number of sources. Highly correlated sources (Pearson's correlation coefficient [Swinscow and Campbell, 2002] ($\rho$) higher than a threshold) were automatically discarded. The threshold used for this study was 0.8. Figures 7.1 and 7.2 show examples of uncorrelated sources (Pearson's coefficient below the selected threshold) and correlated sources (Pearson's coefficient above the selected threshold), respectively.
$\boldsymbol{A}$ was initialized as the absolute value of an i.i.d. Gaussian random matrix. The values of the spatial and the spectral regularization parameters of the objective function [7.6] were estimated by cross validation and set to $\alpha_1 = 0.05$ and $\alpha_2 = 0.1$. Regarding the wavelet decompositions, a Daubechies basis with 2 vanishing moments over one resolution level was considered. Fig. 7.4 shows a comparison of the proposed method (SSR) with two other state-of-the-art BSS methods, accelerated HALS [Gillis and Glineur, 2012] and preprocessed NMF (PNMF) [Gillis, 2012]. HALS stands for accelerated hierarchical alternating least squares algorithm and was initially proposed in [Cichocki et al., 2007]. This algorithm successively updates each column of the observed data ($\boldsymbol{Y}$) with an optimal and easy to compute closed-form solution. We have used the accelerated version of this algorithm proposed

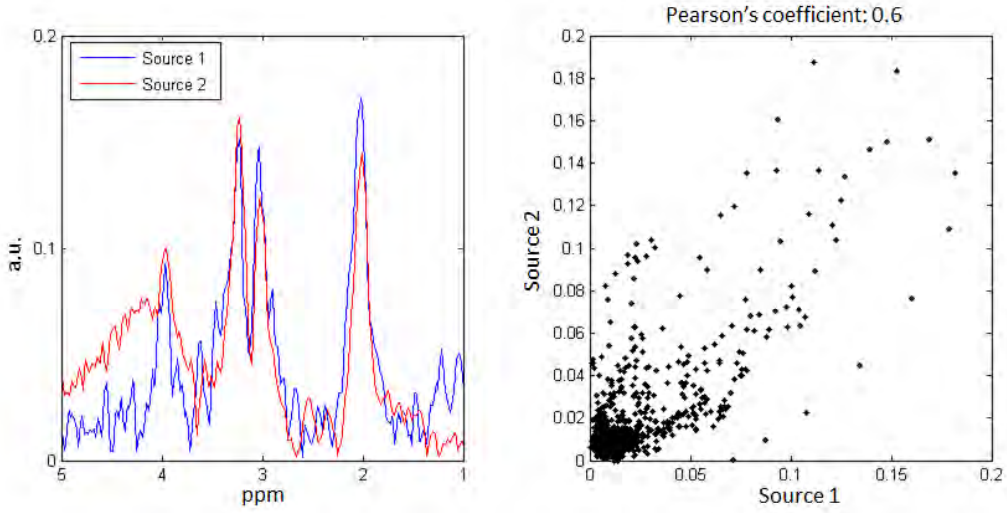


Figure 7.1: Sources with Pearson's correlation coefficient below 0.8 (left). Scatterplot of the two sources (right).

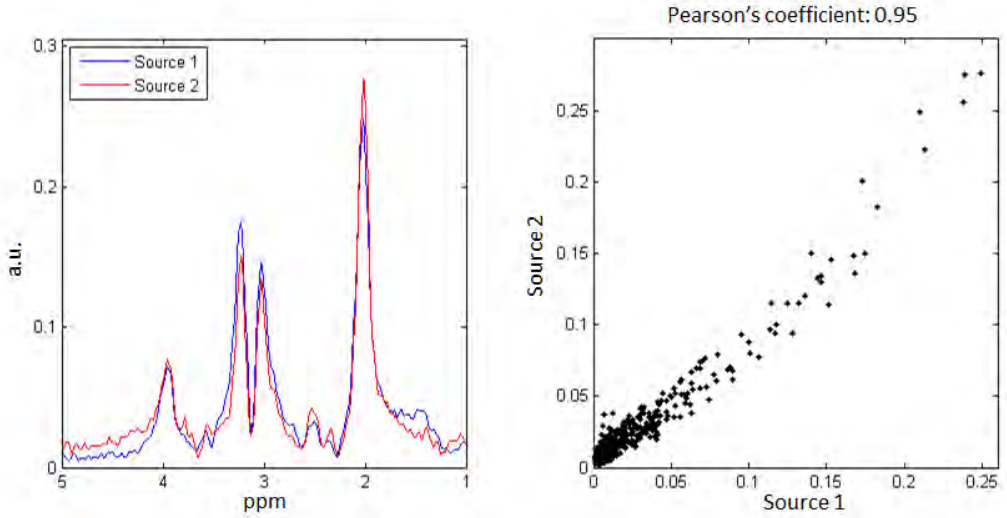


Figure 7.2: Sources with Pearson's correlation coefficient above 0.8 (left). Scatterplot of two sources (right).

in [Gillis and Glineur, 2012]. Preprocessed NMF, introduced in [Gillis, 2012], is based on the preprocessing of the input data matrix ($\boldsymbol{Y}$) with the aim to

obtain more well-posed NMF problems whose solutions are sparser. Both algorithms have been run using the default parameters proposed by their authors. In order to show the improvement due to the incorporation of the spatial term, the results obtained when only the sparsity of the sources is considered ($\alpha_1 = 0.05$ and $\alpha_2 = 0$ in [7.6]) are also displayed and referred to as SSR-Spectro. While HALS and PNMF are able to extract only two physically meaningful sources, SSR is able to detect three sources (normal (j), tumor (k) and necrosis (l) in Fig. 7.4) that are in agreement with the companion MRI image. Note that the abundance maps correspond to the voxels within the volume of interest (VOI), i.e., the inner $10 \times 10$ grid inside the white rectangle. With "physically meaningful sources" we refer to spectral sources that can be easily associated to a specific tissue type. Examples of sources reflecting different tissue patterns are shown in Figure 7.3.

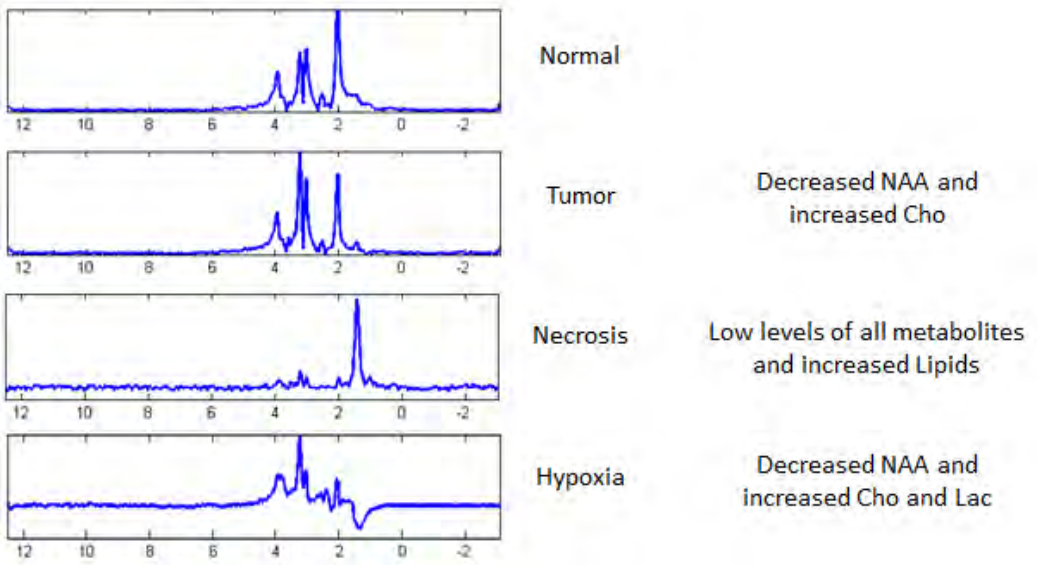


Figure 7.3: Spectral sources reflecting different tissue types.

Among the compared methods, SSR is the only one capable of identifying the necrosis area even when only the spectral prior is considered (SSR-Spectro). However, by adding the spatial term, the identification of the tumor and necrosis regions is clearly improved and the sources are less correlated (mean $\rho$ is 0.65 for SSR and 0.74 for SSR-Spectro) and therefore more easily interpretable than the sources obtained with SSR-Spectro. The identification of

intratumoral necrotic tissue can be helpful in several situations. Necrosis may help to distinguish anaplastic glioma from GBM [Fayed and Modrego, 2005], as this finding is much more frequent in GBM. In fact, necrosis is the hallmark of glioblastoma and is caused by tumor hypoxia as a result of increased cell proliferation and mitotic activity, as well as insufficient tissue perfusion. On conventional contrast-enhanced T1-weighted images, tumor necrosis can be easily diagnosed with the fact that necrotic zones are typically less enhanced, giving the tumor an appearance of irregular rim enhancing mass (Figure 4(a)). However, imaging diagnosis of necrosis can be problematic in early stages or in micronecrosis in which the necrotic region may show to be enhanced or not enhanced at all. MRSI is able to show characteristic metabolites accumulated in the necrotic regions, even when necrosis is not clearly seen on contrast-enhanced T1-weighted images. Differentiating tumor and therapy-related necrosis remains challenging because both entities share similar imaging features, such as irregular rim-like contrast enhancement, mass effect, and vasogenic edema [Hung-Wen et al., 2013]. MRSI has been shown to differentiate between the two conditions. In the study of Nakajima et al. [Nakajima et al., 2009], it was shown that the Lac/Cho ratios are significantly higher in radiation necrosis than in tumor recurrence.
Another clinical application is the differentiation between ring-enhancing brain abscesses and tumor necrosis on T1-weighted images as shown in [Lai et al., 2002]. On the other hand, tumor necrosis is a significant prognostic factor of survival. In [Martens et al., 2013], patients with tumor visible necrosis had a median survival of 5.4 months whereas patients without tumor necrosis had a median survival of 7.2 months. A likely explanation might be the effect of hypoxia on radiosensitivity (hypoxia impacts on outcome by reducing radiosensitivity).
For the comparison we have used magnitude spectra since HALS and SNMF (NMF-based methods) are restricted to non-negative sources. This can be a clear limitation because different tissue patterns may present similar magnitude spectra. For example, the presence of lactate (marker of hypoxia) and lipids (indicating the presence of necrosis) are of high diagnostic value because these metabolites are not detectable in healthy brain tissue. However, in (long-TE) MRSI spectra the inverted peak of lactate occupies the same resonant frequency as lipid, and both metabolites are difficult to differentiate when using magnitude spectra. The regions of lactate most likely represent areas of hypoxic but viable tumor, whereas the regions of mobile lipid represent necrotic nonviable tissue. The separate detection of the two

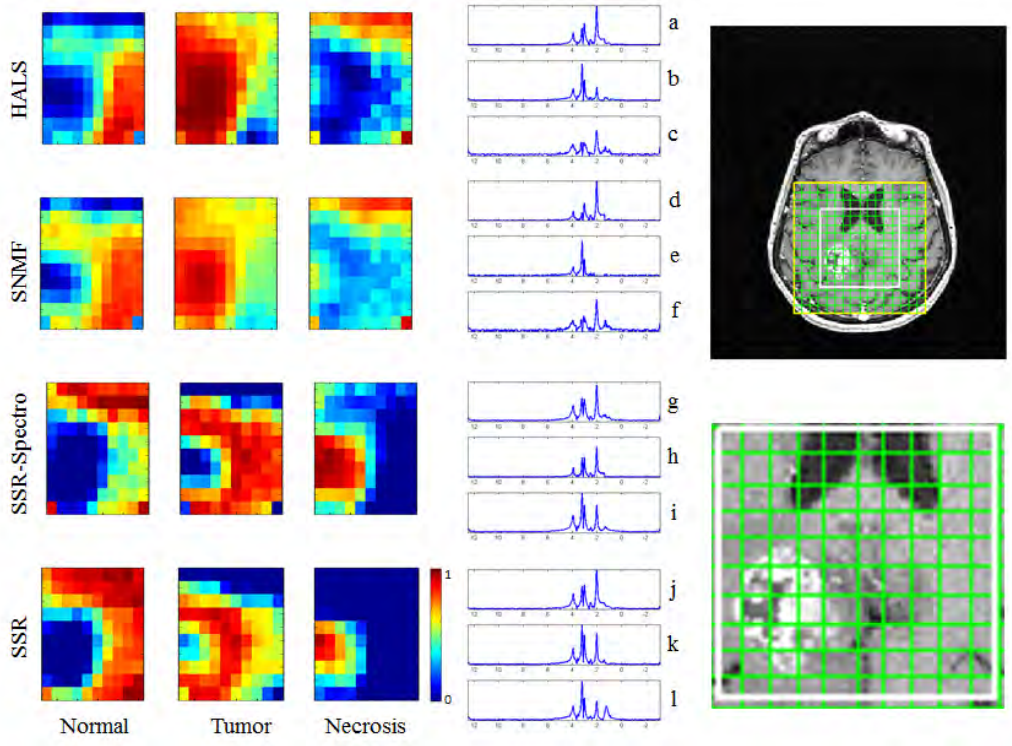


Figure 7.4: Left: Maps showing the spatial distribution of the different tissue patterns (sources). Middle: sources related to normal tissue (a, d, g, j), tumor (b, e, h, k) and necrosis (c, f, i, l). Right: T1-weighted after gadolinium injection (top), voxels within the volume of interest (bottom).

metabolites is therefore important in studying the relationship between hypoxia and necrosis within a brain tumor [Cha, 2006]. Fig. 7.5 shows the results provided by the proposed method using the real part of the spectra for an MRSI dataset presenting hypoxic and necrotic tumor regions. The spatially predominant (c) spectral pattern (g) corresponds to spectra with normal levels of choline (Cho), creatine (Cr) and N-acetyl-aspartate (NAA) and presence of lactate (Lac) throughout the FLAIR-enhanced area (b). SSR is able to differentiate two different tumor patterns, the necrotic core (d) (spectral pattern (h) showing the presence of lipids) and a hypoxic area (e) (spectral pattern (i) showing high Cho, low NAA and presence of Lac). Apart from the presence of Lipids, the spectral pattern showing necrosis (h) presents abnormal metabolite levels (elevated Cho and low NAA). This pre-

sumably corresponds to a mixture of tumor and necrosis tissues due to the relatively large size of the MRSI voxels. In addition, the proposed method is robust against the presence of bad quality spectra, which are grouped in a separated pattern. This is the case of the fourth source (j) that represents spectra where the NAA signal is obscured due to a severe lipid contamination.

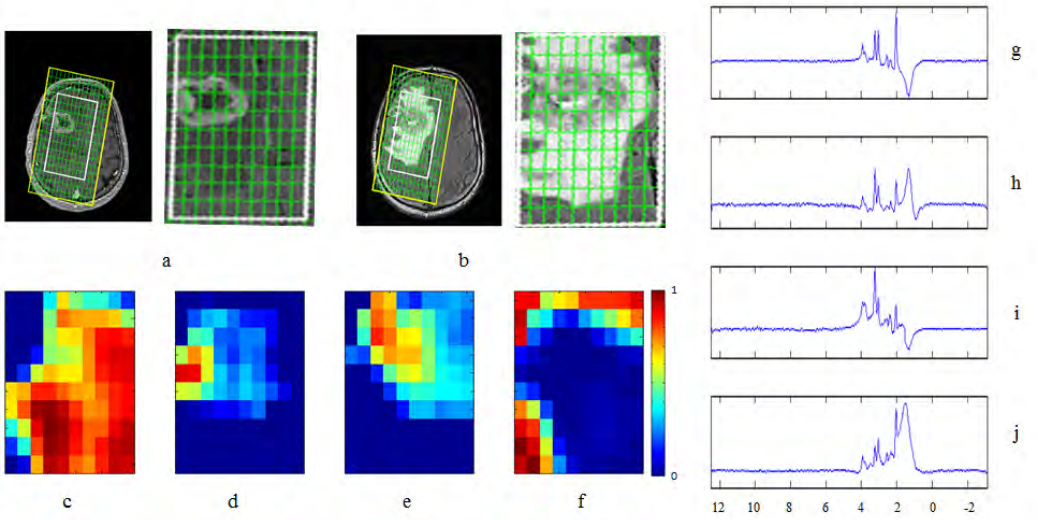


Figure 7.5: T1-weighted after gadolinium injection (left) and voxels within the volume of interest (right) (a); FLAIR (left) and voxels within the volume of interest (right) (b); Maps showing the spatial distribution of normal tissue (c), necrosis (d), hypoxia (e) and lipid contamination (f); Sources related to normal tissue (g), necrosis (h), hypoxia (i) and lipid contamination (j).

Tumor infiltration into the normal tissue, beyond the contrast-enhanced or abnormal MRI areas, is a well-known phenomenon that cannot always be differentiated from edema on T2-weighted or FLAIR images. By using MRSI, it is possible to discriminate both aspects: edema does not modify metabolic ratios whereas the area of cellular infiltration usually demonstrates abnormal Cho/NAA ratio [Nelson et al., 2002]. Fig. 7.6 shows that the proposed method is also able to differentiate between tumor infiltration and edema in peri-enhancing FLAIR/T2 areas. The spectral pattern of edema (j) shows normal metabolic ratios, while tumor infiltration (f) shows a pattern (i) with increased Choline and decreased NAA. The pattern of edema (j) shows reduced metabolite peaks possibly due to the presence of interstitial water

that decreases the signal of the metabolites [Di Costanzo et al., 2003]. The presence of Lac and decreased NAA are also in accordance with cerebral peritumoral edema [Riccia et al., 2007]. The map of tumor infiltration (f) is in accordance with the later relapse of the patient (d).

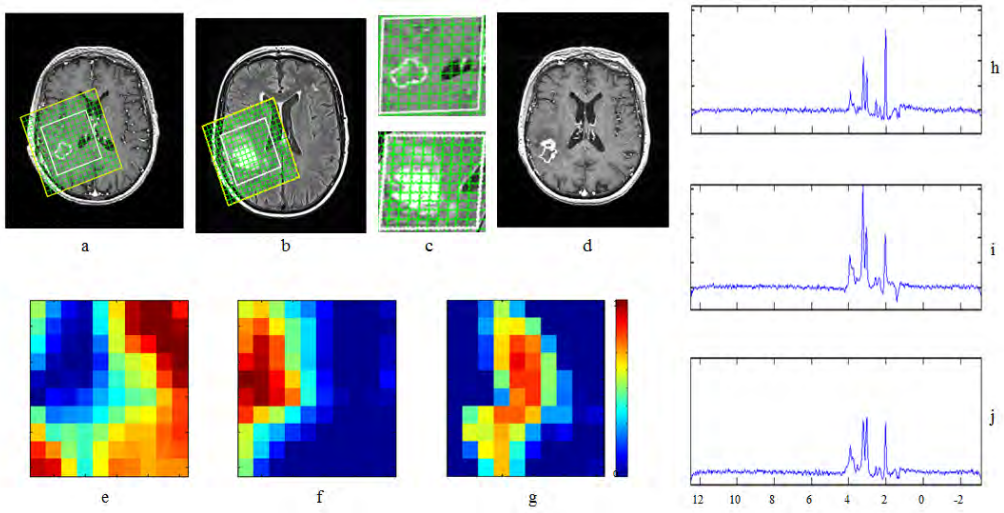


Figure 7.6: T1-weighted after gadolinium injection and FLAIR images before treatment (a) and (b); corresponding voxels within the volume of interest (c); T1-weighted after gadolinium injection at relapse (d); Maps showing the spatial distribution of normal tissue (e), tumor infiltration (f) and edema (g); Sources related to normal tissue (h), tumor infiltration (i) and edema (j).

Figure 7.7 below, shows a recently resected patient. In this case, the resection cavity shows remaining tumor with high levels of lipids indicating necrosis. The tissue around the cavity does not shows signs of infiltration. The spectral pattern in this area shows a sloping baseline which may result from the presence of interstitial water from the edema [Di Costanzo et al., 2003].
In some cases, using a higher number of sources can provide additional information about the heterogeneous distribution of the lesion. Figure 7.8 shows the results for a biopsied patient before RT using 3 sources. The number of sources was estimated using [Nascimento and Bioucas Dias, 2005] and the the highly correlated sources were discarded as described above. The peri-enhancing apparently oedematous area (a,b) shows presumed tumour with a spectral pattern (f) with high levels of Cho and a highly abnormal Cho/NAA ratio. Spectra in regions closer to the skull (e) are contaminated by lipids

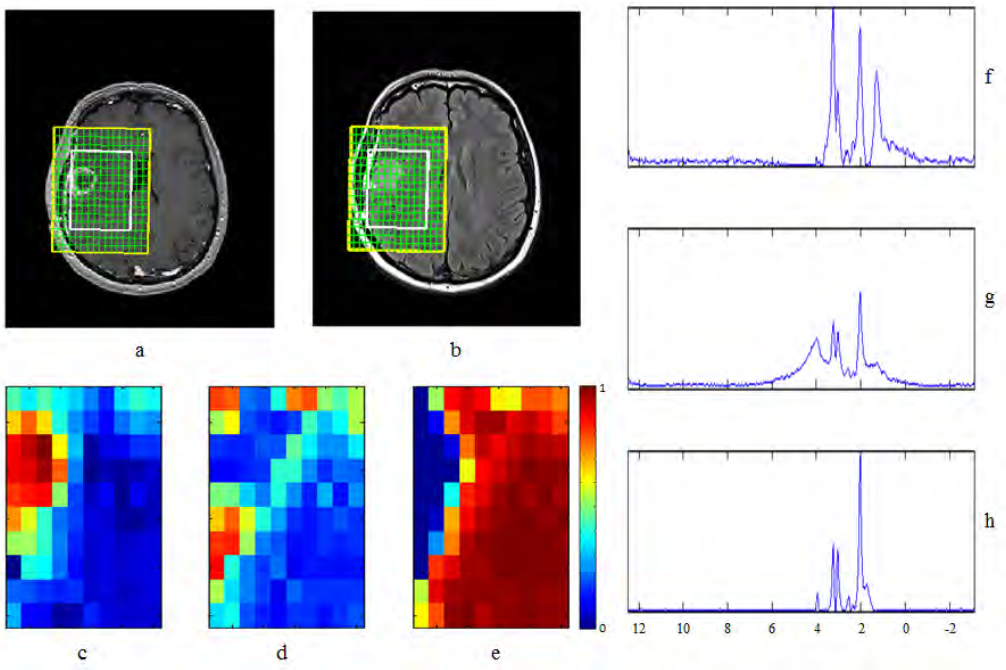


Figure 7.7: T1-weighted after gadolinium injection and FLAIR images before treatment (a) and (b); Maps showing the spatial distribution of tumor tissue (c), edema (d) and normal (e); Sources related to tumor (f), edema (g) and normal tissue (h).

and are correctly identified by the proposed method. Figure 7.9 shows the results for the same patient using 4 sources. Using an additional sources, the method is able to discriminate between the tumor core (d) and tumor infiltration (e). The area showing higher infiltration (e) corresponds to the area of posterior relapse of the patient (c). This suggests that testing with an additional source may be useful to extract more detailed information for some cases.

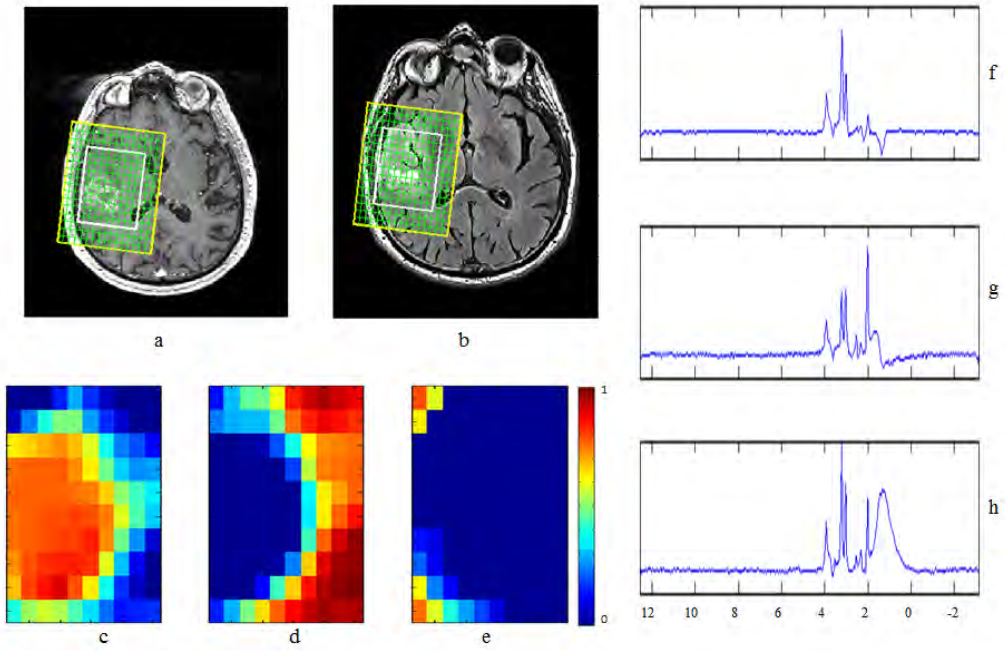


Figure 7.8: T1-weighted after gadolinium injection and FLAIR images before treatment (a) and (b); Maps showing the spatial distribution of tumor tissue (c), normal (d) and lipid contamination (e); Sources related to tumor (f), normal (g) and lipid contamination (h).

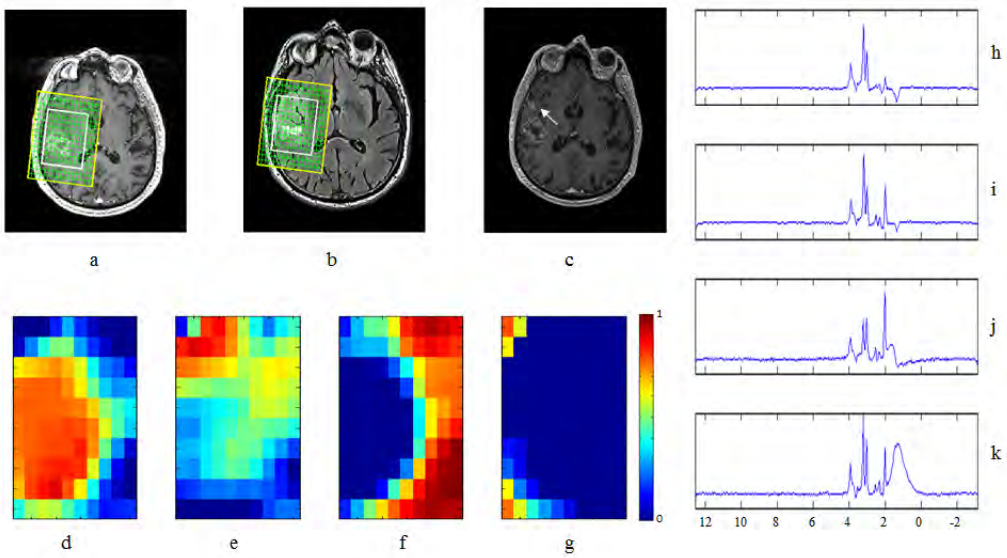


Figure 7.9: T1-weighted after gadolinium injection and FLAIR images before treatment (a) and (b); T1-weighted after gadolinium injection at relapse (c); Maps showing the spatial distribution of tumor tissue (d), infiltration (e) normal (f) and lipid contamination (g); Sources related to tumor (h), infiltration (i), normal (j) and lipid contamination (k).

## 7.5 Conclusion

We presented a new blind source separation method which combines spatial and spectral regularizations in the wavelet domain. The method exploits magnetic resonance spectroscopic imaging data properties such as the sparsity of the spectra in the wavelet domain and the spatial regularity between neighbouring voxels. Experiments on in-vivo data show that the proposed method is able to extract more than two physically meaningful tissue patterns easily interpretable. The abundance maps show spatially coherent and well defined areas, in agreement with expert assesment conducted on companion anatomical MRI images. Unlike previous existing methods, the proposed strategy can deal with negative sources and is not sensitive to initialization. In addition it is robust against noise and the presence of low quality spectra. Future work includes a consistency analysis of the proposed method for a larger group of patients.

# Chapter 8

# Conclusion

MRSI is a non-invasive imaging modality which has demonstrated the ability to characterize physiological changes in tissues before they become visible in conventional MRI. Information provided by MRSI can be used to guide RT treatments by the definition of biologically tailored target volumes for dose escalation. Despite the numerous publications on the topic, the interpretation of MRSI data is still a challenging problem due to different factors such as the low SNR of the signals, the overlap of spectral lines or the presence of nuisance components. This PhD thesis has contributed to the development of new processing algorithms able to achieve reliable results even under degraded experimental conditions. This objective is addressed through a methodological approach based on novel processing methods that incorporate prior knowledge on the MRSI data using a hybrid regularization in the wavelet domain. Contrary to previous approaches, the suggested methods combine two regularization terms to favor solutions with specific properties in both the spatial and the spectral dimensions. Experiments on synthetic and in vivo data have shown the benefit of using this type of regularization in different applications. Chapter 4 described a method that exploits the proposed regularization scheme to increase the SNR of MRSI data. It suppresses noise in MRSI signals in a non-constrained way. Results showed that the SNR is increased while the spectral and the spatial features of the data are preserved. This makes this technique suitable to describe the disturbed lineshapes and the spatial variations exhibited by in vivo scans, especially in the context of lesions. In Chapter 5, the proposed spatio-spectral regularization is used to improve the robustness of the quantification of MRSI data. Unlike previous quantification algorithms, which are restricted to spatially smooth variations of the parameters, this method allows the use of other prior knowledge such as the sparsity of the MRSI spectra in the wavelet domains. Results demonstrated significant improvements in quantification accuracy and robustness compared to well-known existing methods. In addition, the proposed algorithm was able to correctly quantify metabolites that are missed by other methods due their lower concentrations. This quantifi-

cation algorithm is then used as a feature extraction technique in Chapter 6, where a supervised classification method for the identification of regions at risk of relapse in brain tumor patients is described. Results from this work showed the potential of integrating MRSI information in the RT treatment planning. Finally, Chapter 7 presented a novel blind source separation technique for tissue classification based on the proposed spatio-spectral regularization. This method showed to be robust against noise and the presence of low quality spectra. Unlike other existing techniques, this algorithm is able to extract many physically meaningful tissue patterns and can deal with negative sources.
In all the presented methods, regularization is used to inject prior knowledge about the solutions in the wavelet domain. The dependency on only two hyperparameters (weights of both regularization terms), and the use of fast proximal algorithms that allows parallel computations facilitate the automation of these approaches, which is crucial for the acceptance of the MRSI technique into the clinical routine. The proximal optimization algorithms have been carefully chosen and adapted depending on the specificities of each of the proposed methods.
This PhD opens the way for future developments and applications to be addressed in future works:

1) 3D regularization: extension of the proposed methods to incorporate 3D spatial information available from 3D MRSI data.

2) Validation with high-spatial resolution data: validation of the presented algorithms with high-spatial resolution MRSI data where the low signal-to-noise ratio is a major limitation.

3)Integration of an automatic hyperparameter estimation method: development of a fully auto-calibrated approach to automatically estimate the regularization parameters directly from the data.

4) Multi-parametric regularization: the proposed methods can be extended to incorporate more sophisticated priors, such as tissue distributions, anatomical configurations or functional information extracted from companion (MRI) imaging modalities.

5) Spectral unmixing to improve spatial coverage: any classification method

based on quantification estimates is limited by the fact that there are many MRSI voxels where the quality of the spectra does not allow reliable quantification. Spectral unmixing algorithms tend to be more robust against noise and nuisance components than conventional quantification methods. They can therefore be used as an alternative approach to obtain information from those voxels where quantification is not possible. Combining information from both techniques to build the feature space could be an interesting approach to improve the performance (more information from each voxel), and the spatial coverage (more voxels with available information) of the classification method.

6) Other MRI applications: all the experiments presented in this work have been focused on brain data. It would be very interesting to process MRSI data from other organs, like prostate or breast, with the proposed algorithms.

# Bibliography


Ahmed, OA. 2005. New denoising scheme for magnetic resonance spectroscopy signals, *IEEE Transactions on Medical Imaging*, 24, 809–816.

Ahn, J. 2010. A stable hyperparameter selection for the Gaussian RBF kernel for discrimination, *Statistical Analysis and Data Mining*, 3(3), 142–148.

Alger, JR, JA Frank, A Bizzi, MJ Fulham, BX DeSouza, MO Duhaney, SW Inscoe, JL Black, PC Van Zijl, and CT Moonen. 1990. Metabolism of human gliomas: assessment with H-1 MR spectroscopy and F-18 fluorodeoxyglucose PET, *Radiology*, 177(3), 633–641.

Alonso, J, F Bartumeus, F Isamat, I Ferrer, F Vila, E Ferrer, A Capdevila, and C Arús. 1998. Towards a method for automated classification of 1H MRS spectra from brain tumours, *NMR in Biomedicine*, 11, 177–191.

Amelio, D, S Lorentini, M Schwarz, and M Amichetti. 2010. Intensity-modulated radiation therapy in newly diagnosed glioblastoma: a systematic review on clinical and technical issues, *Radiotherapy and Oncology*, 97(3), 361–369.

Aronen, HJ, IE Gazit, DN Louis, BR Buchbinder, FS Pardo, RM Weisskoff, GR Harsh, GR Cosgrove, EF Halpern, and FH Hochberg. 1994. Cerebral blood volume maps of gliomas: comparison with tumor grade and histologic findings, *Radiology*, 191(1), 41–51.

Askin, NC, B Atis, and E Ozturk-Isik. 2012. Accelerated phosphorus magnetic resonance spectroscopic imaging using compressed sensing, in *Annual International Conference of the IEEE Engineering in Medicine and Biology Society (EMBC)*, IEEE, 1106–1109.

Astrakas, LG, D Zurakowski, AA Tzika, MK Zarifi, DC Anthony, U De Girolami, NJ Tarbell, and PM Black. 2004. Noninvasive magnetic resonance spectroscopic imaging biomarkers to predict the clinical grade of pediatric brain tumors, *Clinical Cancer Research*, 10(24), 8220–8228.

Ayat, NE, M Cheriet, and CY Suen. 2002. Optimization of the svm kernels using an empirical error minimization scheme, in *Pattern Recognition with Support Vector Machines*, Springer, 354–369.

Bao, Y and AA Maudsley. 2007. Improved reconstruction for MR spectroscopic imaging, *IEEE Transactions on Medical Imaging*, 26, 686–695.

Barker, PB and D Lin. 2006. In-vivo proton mr spectroscopy of the human brain, *Progress in Nuclear Magnetic Resonance Spectroscopy*, 49(2), 99–128.

Bartha, R, DJ Drost, and PC Williamson. 1999. Factors affecting the quantification of short echo in-vivo $^1$H MR spectra: prior knowledge, peak elimination, and filtering, *NMR in Biomedicine*, 12, 205–216.

Bax, A and R Freeman. 1980. Enhanced NMR resolution by restricting the effective sample volume, *Journal of Magnetic Resonance*, 37(1), 177–181.

Belge, M, ME Kilmer, and EL Miller. 2002. Efficient determination of multiple regularization parameters in a generalized L-curve framework, *Inverse Problems*, 18, 1161–1183.

Bertholdo, D, A Watcharakorn, and M Castillo. 2013. Brain Proton Magnetic Resonance Spectroscopy, *Neuroimaging Clinics*, 23(3), 359–380.

Bishop, CM. 1995. *Neural networks for pattern recognition*, Oxford university press.

Bloch, F. 1946. Nuclear induction, *Physical review*, 70(7-8), 460.

Block, KT, M Uecker, and J Frahm. 2007. Undersampled radial MRI with multiple coils. Iterative image reconstruction using a total variation constraint, *Magnetic Resonance in Medicine*, 57(6), 1086–1098.

Block, KT, M Uecker, and J Frahm. 2009. Model-based iterative reconstruction for radial fast spin-echo MRI, *IEEE Transactions on Medical Imaging*, 28(11), 1759–1769.

Blüml, S. 2013. Magnetic resonance spectroscopy: basics, in *MR Spectroscopy of Pediatric Brain Disorders*, Springer, 11–23.

Boer, VO, DW Klomp, C Juchem, PR Luijten, and RA de Graaf. 2012. Multislice $^1$H MRSI of the human brain at 7T using dynamic B(0)and B(1) shimming., *Magnetic Resonance in Medicine*, 68, 662–670.

Boser, BE, IM Guyon, and VN Vapnik. 1992. A training algorithm for optimal margin classifiers, in *Proceedings of the 5th Annual Workshop on Computational Learning Theory*, ACM, 144–152.

Bottomley, PA. 1987. Spatial localization in NMR spectroscopy in vivo, *Annals of the New York Academy of Sciences*, 508, 333–348.

Boyer, C, P Ciuciu, P Weiss, and S Mériaux. 2012. HYR 2 PICS: Hybrid regularized reconstruction for combined parallel imaging and compressive sensing in MRI, in *Proceedings of the IEEE International Symposium on Biomedical Imaging (ISBI)*, IEEE, 66–69.

Brown, TR, BM Kincaid, and K Ugurbil. 1982. NMR chemical shift in three dimensions, *Proceedings of the National Academy of Sciences*, 79(11), 3523–3526.

Bruzzone, L, M Marconcini, and C Persello. 2007. Fusion of spectral and spatial information by a novel SVM classification technique, in *Proceedings of the IEEE International Geoscience and Remote Sensing Symposium (IGARSS)*, IEEE, 4838–4841.

Burtscher, IM, G Skagerberg, B Geijer, E Englund, F Ståhlberg, and S Holtås. 2000. Proton MR spectroscopy and preoperative diagnostic accuracy: an evaluation of intracranial mass lesions characterized by stereotactic biopsy findings, *American Journal of Neuroradiology*, 21(1), 84–93.

Bushong, SC. 2013. *Magnetic resonance imaging: physical and biological principles*, Elsevier Health Sciences.

Cancino-De-Greiff, HF, R Ramos-Garcia, and JV Lorenzo-Ginori. 2002. Signal de-noising in magnetic resonance spectroscopy using wavelet transforms, *Concepts in Magnetic Resonance*, 14(6), 388–401.

Carmeliet, P and RK Jain. 2000. Angiogenesis in cancer and other diseases, *Nature*, 407, 249–257.

Carpenter, RG. 1960. Principles and procedures of statistics, with special reference to the biological sciences, *The Eugenics Review*, 52(3), 172.

Cavassila, S, S Deval, C Huegen, D van Ormondt, and D Graveron-Demilly. 2001. Cramér-rao bounds: an evaluation tool for quantification, *NMR in Biomedicine*, 14, 278–283.

Cha, S. 2006. Update on brain tumor imaging: From anatomy to physiology, *American Journal of Neuroradiology*, 27(3), 475–487.

Chaari, L. 2010. *Parallel Magnetic Resonance Imaging reconstruction problems using wavelet representations*, Ph.D. thesis, Université de Paris-Est Marne-la-Vallée.

Chaari, L, P Ciuciu, S Mériaux, and JC Pesquet. 2014. Spatio-temporal wavelet regularization for parallel MRI reconstruction: application to functional MRI, *Magnetic Resonance Materials in Physics, Biology and Medicine (MAGMA)*, 27(6), 509–529. DOI: 10.1007/s10334-014-0436-5.

Chaari, L, JC Pesquet, A Benazza-Benyahia, and P Ciuciu. 2008a. Autocalibrated parallel MRI reconstruction in the wavelet domain, in *Proceedings of the IEEE International Symposium on Biomedical Imaging (ISBI)*, Paris, France, 756–759.

Chaari, L, JC Pesquet, A Benazza-Benyahia, and P Ciuciu. 2008b. Autocalibrated regularized parallel MRI reconstruction in the wavelet domain, in *Proceedings of the IEEE International Symposium on Biomedical Imaging (ISBI)*, IEEE, 756–759.

Chaari, L, JC Pesquet, A Benazza-Benyahia, and P Ciuciu. 2011. A wavelet-based regularized reconstruction algorithm for SENSE parallel MRI with applications to neuroimaging, *Medical Image Analysis*, 15(2), 185–201.

Chaari, L, JC Pesquet, JY Tourneret, P Ciuciu, and A Benazza-Benyahia. 2010. A hierarchical Bayesian model for frame representation, *IEEE Transactions on Signal Processing*, 18(11), 5560–5571.

Chambolle, A and T Pock. 2011. A first-order primal-dual algorithm for convex problems with applications to imaging, *Journal of Mathematical Imaging and Vision*, 40(1), 120–145.

Chang, CC and CJ Lin. 2011. LIBSVM: A library for support vector machines, *ACM Transactions on Intelligent Systems and Technology*, 2(3), 27. Software available at http://www.csie.ntu.edu.tw/∼cjlin/libsvm.

Chapelle, O, V Vapnik, O Bousquet, and S Mukherjee. 2002. Choosing multiple parameters for support vector machines, *Machine learning*, 46(1-3), 131–159.

Chen, L, Z Weng, G Lai, and M Garland. 2002. An efficient algorithm for automatic phase correction of NMR spectra based on entropy minimization., *Journal of Magnetic Resonance*, 158, 164–168.

Cichocki, A, R Zdunek, and S Amari. 2007. Hierarchical ALS Algorithms for Nonnegative Matrix and 3D Tensor Factorization, in *Independent Component Analysis and Signal Separation*, Springer, 169–176.

Ciuciu, P, JB Poline, G Marrelec, J Idier, C Pallier, and H Benali. 2003. Unsupervised robust nonparametric estimation of the hemodynamic response function for any fMRI experiment, *IEEE Transactions on Medical Imaging*, 22(10), 1235–1251.

Cobas, C and S Sykora. 2007. Extended dispersion-absorption approach to automatic phasing of HR-NMR spectra., in *Proceedings of the 48th Experimental Nuclear Magnetic Resonance (ENC) Conference*, Daytona Beach, USA.

Cobas, JC, MA Bernstein, M Martín-Pastor, and P García Tahoces. 2006. A new general-purpose fully automatic baseline-correction procedure for 1D and 2D NMR data., *Journal of Magnetic Resonance*, 183(1), 145–151.

Combettes, PL and JC Pesquet. 2008. A proximal decomposition method for solving convex variational inverse problems, *Inverse problems*, 24(6).

Combettes, PL and JC Pesquet. 2011. Proximal splitting methods in signal processing, *Fixed-Point Algorithms for Inverse Problems in Science and Engineering*, 185–212.

Cortes, C and V Vapnik. 1995. Support-vector networks, *Machine Learning*, 20(3), 273–297.

Craig, E and A Marshall. 1998. Automated phase correction of FT NMR spectra by means of phase measurement based on dispersion versus absorption relation (DISPA)., *Journal of Magnetic Resonance*, 76(13), 458–475.

Cristianini, Nello and J Shawe-Taylor. 2000. *An introduction to support vector machines and other kernel-based learning methods*, Cambridge university press.

De Rochefort, L. 2010. Encoding with Radiofrequency Spoiling, Equilibrium States and Inverse Problem for Parametric Mapping, in *Proceedings of the International Society for Magnetic Resonance in Medicine (ISMRM)*, vol. 18, 350.

De Sanctis, S, MW Malloni, W Kremer, AM Tomé, EW Lang, KP Neidig, and HR Kalbitzer. 2011. Singular spectrum analysis for an automated solvent artifact removal and baseline correction of 1D NMR spectra., *BMC Bioinformatics*, 210(2), 177–183.

Deviers, A, S Ken, T Filleron, B Rowland, A Laruelo, I Catalaa, V Lubrano, P Celsis, I Berry, G Mogicato, E Cohen-Jonathan Moyal, and A Laprie. 2014. Evaluation of lactate/N-acetyl-aspartate ratio defined with MR spectroscopic imaging before radiotherapy as a new predictive marker of the site of relapse in patients with glioblastoma multiforme, *International Journal of Radiation Oncology Biology Physics*, 90(2), 385–393.

Devos, A, AW Simonetti, M Van Der Graaf, L Lukas, JA Suykens, L Vanhamme, LM Buydens, A Heerschap, and S Van Huffel. 2005. The use of multivariate MR imaging intensities versus metabolic data from MR spectroscopic imaging for brain tumour classification, *Journal of Magnetic Resonance*, 173(2), 218–228.

Di Costanzo, A, F Trojsi, M Tosetti, GM Giannatempo, F Nemore, M Piccirillo, S Bonavita, G Tedeschi, and T Scarabino. 2003. High-field proton MRS of human brain, *European Journal of Radiology*, 48, 146–153.

Diop, A, Y Zaim-Wadghiri, A Briguet, and D Graveron-Demilly. 1994. Improvements of quantitation by using the Cadzow enhancement procedure prior to any linear-prediction methods, *Journal of Magnetic Resonance*, 105, 17–24.

Donoho, DL and JM Johnstone. 1994. Ideal spatial adaptation by wavelet shrinkage, *Biometrika*, 81(3), 425–455.

Dowling, C, AW Bollen, SM Noworolski, MW McDermott, NM Barbaro, MR Day, RG Henry, SM Chang, WP Dillon, SJ Nelson, et al. 2001. Preoperative proton MR spectroscopic imaging of brain tumors: correlation with histopathologic analysis of resection specimens, *American Journal of Neuroradiology*, 22(4), 604–612.

Draper, NR, H Smith, and E Pownell. 1966. *Applied regression analysis*, Wiley New York.

Dydak, U, M Weiger, KP Pruessmann, D Meier, and P Boesiger. 2001. Sensitivity-encoded spectroscopic imaging, *Magnetic Resonance in Medicine*, 46(4), 713–722.

Eisenhauer, EA, P Therasse, J Bogaerts, LH Schwartz, D Sargent, R Ford, J Dancey, S Arbuck, S Gwyther, M Mooney, et al. 2009. New response evaluation criteria in solid tumours: revised RECIST guideline (version 1.1), *European Journal of Cancer*, 45(2), 228–247.

Ernst, R. 1969. Numerical Hilbert transform and automatic phase correction in magnetic resonance spectroscopy., *Journal of Magnetic Resonance*, 1, 7–26.

Eslami, R and M Jacob. 2009a. Reduction of distortions in MRSI using a new signal model., in *Proceedings of the IEEE International Symposium on Biomedical Imaging (ISBI)*, 438–441.

Eslami, R and M Jacob. 2009b. Spatial spectral modeling for robust MRSI, in *Proceedings of the Annual International Conference of the IEEE Engineering in Medicine and Biology Society (EMBC'09)*, IEEE, 6663–6666.

Evelhoch, JL. 1999. Key factors in the acquisition of contrast kinetic data for oncology, *Journal of Magnetic Resonance Imaging*, 10, 254–259.

Fayed, N and PJ Modrego. 2005. The contribution of magnetic resonance spectroscopy and echoplanar perfusion-weighted MRI in the initial assessment of brain tumours, *Journal of neuro-oncology*, 72(3), 261–265.

Frahm, J, KD Merboldt, and W H"anike. 1987. Localized proton spectroscopy using stimulated echoes, *Journal of Magnetic Resonance*, 72(3), 502–508.

Fu, Y and H Serrai. 2011. Fast magnetic resonance spectroscopic imaging (MRSI) using wavelet encoding and parallel imaging: in vitro results, *Journal of Magnetic Resonance*, 211(1), 45–51.

Gamper, U, P Boesiger, and S Kozerke. 2008. Compressed sensing in dynamic MRI, *Magnetic Resonance in Medicine*, 59(2), 365–373.

García-Figueiras, R, S Baleato-González, AR Padhani, L Oleaga, JC Vilanova, A Luna, and JC Gómez. 2016. Proton magnetic resonance spectroscopy in oncology: the fingerprints of cancer?, *Diagnostic and Interventional Radiology*, 22(1), 75.

Gareth, J. 2013. *An Introduction to Statistical Learning: with Applications in R*, Springer.

Geethanath, S, HM Baek, SK Ganji, Y Ding, EA Maher, RD Sims, C Choi, MA Lewis, and VD Kodibagkar. 2012. Compressive sensing could accelerate 1H MR metabolic imaging in the clinic, *Radiology*, 985–994.

Gholipour, A, N Kehtarnavaz, R Briggs, M Devous, and K Gopinath. 2007. Brain functional localization: a survey of image registration techniques, *IEEE Transactions on Medical Imaging*, 26(4), 427–451.

Gillard, JH, AD Waldman, and PB Barker. 2009. *Clinical MR neuroimaging: physiological and functional techniques*, Cambridge University Press.

Gillis, N. 2012. Sparse and Unique Nonnegative Matrix Factorization Through Data Preprocessing, *Journal of Machine Learning Research*, 13, 3349–3386.

Gillis, N and F Glineur. 2012. Accelerated Multiplicative Updates and Hierarchical ALS Algorithms for Nonnegative Matrix Factorization, *Neural Computation*, 24(4), 1085–1105.

Gillis, N and RJ Plemmons. 2012. Sparse Nonnegative Matrix Underapproximation and its Application for Hyperspectral Image Analysis, *Linear Algebra and its Applications*, 438(10), 3991–4007.

Govindaraju, V, K Young, and A Maudsley. 2000. Proton NMR chemical shifts and coupling constants for brain metabolites, *NMR in Biomedicine*, 13, 129–153.

Graveron-Demilly, D, A Diop, A Briguet, and B Fenet. 1993. Product-Operator algebra for strongly coupled spin systems, *Journal of Magnetic Resonance*, 101, 233–239.

Graves, EE, SJ Nelson, DB Vigneron, Cy Chin, L Verhey, M McDermott, D Larson, PK Sneed, S Chang, MD Prados, et al. 2000. A preliminary

study of the prognostic value of proton magnetic resonance spectroscopic imaging in gamma knife radiosurgery of recurrent malignant gliomas, *Neurosurgery*, 46(2), 319.

Guerquin-Kern, M, D Van De Ville, C Vonesch, JC Baritaux, KP Pruessmann, and M Unser. 2009a. Wavelet-regularized reconstruction for rapid MRI, in *Proceedings of the IEEE International Symposium on Biomedical Imaging (ISBI)*, IEEE, 193–196.

Guerquin-Kern, M, D Van De Ville, C Vonesch, JC Baritaux, KP Pruessmann, and M Unser. 2009b. Wavelet regularized reconstruction for rapid MRI, in *Proceedings of the IEEE International Symposium on Biomedical Imaging (ISBI)*, Boston, USA, 193–196.

Guimaraes, MD, A Schuch, B Hochhegger, JL Gross, R Chojniak, and E Marchiori. 2014. Functional magnetic resonance imaging in oncology: state of the art, *Radiologia Brasileira*, 47(2), 101–111.

Güntert, P and K Wüthrich. 1992. FLATT-a new procedure for high-quality baseline correction of multidimensional NMR spectra., *Journal of Magnetic Resonance*, 96(2), 403–407.

Haase, A, J Frahm, W Hanicke, and D Matthaei. 1985. 1H NMR chemical shift selective (CHESS) imaging, *Physics in medicine and biology*, 30(4), 341.

Hernando, CG, L Esteban, T Cañas, E Van den Brule, and M Pastrana. 2010. The role of magnetic resonance imaging in oncology, *Clinical and Translational Oncology*, 12(9), 606–613.

Higgins, LJ and MG Pomper. 2011. The evolution of imaging in cancer: current state and future challenges, *Seminars in Oncology*, 38(1), 3–15.

Histed, SN, ML Lindenberg, E Mena, B Turkbey, PL Choyke, and KA Kurdziel. 2012. Review of functional/anatomic imaging in oncology, *Nuclear Medicine Communications*, 33(4), 349–361.

Hofmann, L, J Slotboom, C Boesch, and R Kreis. 2001. Characterization of the macromolecule baseline in localized 1H-MR spectra of human brain., *Magnetic Resonance in Medicine*, 46(5), 855–863.

Horská, A and PB Barker. 2010. Imaging of brain tumors: MR spectroscopy and metabolic imaging, *Neuroimaging clinics of North America*, 20(3), 293–310.

Hsu, CW, CC Chang, and CJ Lin. 2003. A practical guide to support vector classification, Tech. rep., Department of Computer Science, National Taiwan University. http://www.csie.ntu.edu.tw/∼cjlin/papers/guide/guide.pdf.

Hu, S, M Lustig, AP Chen, J Crane, A Kerr, D Kelley, R Hurd, J Kurhanewicz, SJ Nelson, JM Pauly, and DB Vigneron. 2008. Compressed sensing for resolution enhancement of hyperpolarized 13C flyback 3D-MRSI, *Journal of Magnetic Resonance*, 192(2), 258–264.

Huang, C, CG Graff, EW Clarkson, A Bilgin, and MI Altbach. 2012. T2 mapping from highly undersampled data by reconstruction of principal component coefficient maps using compressed sensing, *Magnetic resonance in medicine*, 67(5), 1355–1366.

Hung-Wen, K, C Shih-Wei, C Hsiao-Wen, YT Fong, , and C Cheng-Yu. 2013. Advanced MR Imaging of Gliomas: An Update, *BioMed Research International*. DOI: 10.1155/2013/970586.

Jaakkola, T, M Diekhans, and D Haussler. 1999. Using the Fisher kernel method to detect remote protein homologies, in *Proceedings of the 7th International Conference on Intelligent Systems for Molecular Biology (ISMB)*, 149–158.

Jansen, J, WH Backes, K Nicolay, and M Kooi. 2006. 1H MR Spectroscopy of the Brain: Absolute Quantification of Metabolites, *Radiology*, 240(2), 318–332.

Kasten, J, A Klauser, F Lazeyras, and D Van De Ville. 2015. Magnetic resonance spectroscopic imaging at superresolution: Overview and perspectives, *Journal of Magnetic Resonance*.

Kasten, J, F Lazeyras, and D Van De Ville. 2013. Data-driven MRSI spectral localization via low-rank component analysis, *IEEE Transactions on Medical Imaging*, 32(10), 1853–1863.

Kelm, BM, FO Kaster, A Henning, MA Weber, P Bachert, P Boesiger, FA Hamprecht, and BH Menze. 2012. Using spatial prior knowledge in the spectral fitting of magnetic resonance spectroscopic images, *NMR in Biomedicine*, 25, 1–13.

Kelm, BM, BH Menze, T Neff, CM Zechmann, and FA Hamprecht. 2006. CLARET: a tool for fully automated evaluation of MRSI with pattern recognition methods, in *Bildverarbeitung für die Medizin*, Springer, 51–55.

Ken, S, L Vieillevigne, X Franceries, L Simon, C Supper, JA Lotterie, T Filleron, V Lubrano, I Berry, E Cassol, M Delannes, P Celsis, E Moyal Cohen-Jonathan, and A Laprie. 2013. Integration method of 3D MR spectroscopy into treatment planning system for glioblastoma IMRT dose painting with integrated simultaneous boost, *Radiation Oncology*, 8, 1.

Khunt, DP and YN Makwana. 2012. Image registration using intensity based technique, *Journal of information, knowledge and research in electronics and communication engineering*, 2(2), 607–609.

Kim, D, W Youngdo, and W Hoshik. 2000. Noise Suppression in NMR Spectrum by Using Wavelet Transform Analysis, *Journal of the Korean Magnetic Resonance Society*, 4(2), 103–115.

Kim, EE, , and EF Jackson. 2012. *Molecular imaging in oncology: PET, MRI, and MRS*, Springer Science & Business Media.

Kim, J and P Haesun. 2008. Sparse nonnegative matrix factorization for clustering.

Knight-Scott, J. 1999. Application of multiple inversion recovery for suppression of macromolecule resonances in short echo time 1H NMR spectroscopy of human brain., *Journal of Magnetic Resonance*, 140(1), 228–234.

Knoll, F, K Bredies, T Pock, and R Stollberger. 2011. Second order total generalized variation (TGV) for MRI, *Magnetic resonance in medicine*, 65(2), 480–491.

Kotyk, JJ, NG Hoffman, WC Hutton, GL Bretthorst, and JJH Ackerman. 1995. Comparison of fourier and bayesian analysis of NMR signals, *Journal of Magnetic Resonance*, 116, 1–9.

Kounelakis, MG, ME Zervakis, GJ Postma, LM Buydens, A Heerschap, and X Kotsiakis. 2009. Revealing the metabolic profile of brain tumors for diagnosis purposes, in *Proceedings of the Annual International Conference of the IEEE Engineering in Medicine and Biology Society (EMBC'09)*, 35–38.

Krabbe, K, P Gideon, P Wagn, U Hansen, C Thomsen, and F Madsen. 1997. MR diffusion imaging of human intracranial tumours, *Neuroradiology*, 39(7), 483–489.

Kreis, R. 2004. Issues of spectral quality in clinical 1H-magnetic resonance spectroscopy and a gallery of artifacts, *NMR in Biomedicine*, 17(6), 361–381.

Kreis, R, T Ernst, and BD Ross. 1993. Absolute quantitation of water and metabolites in the human brain. II. Metabolite concentrations, *Journal of magnetic resonance, Series B*, 102(1), 9–19.

Kristiansen, K, S Hagen, T Kollevold, A Torvik, I Holme, M Stat, R Nesbakken, R Hatlevoll, M Lindgren, A Brun, et al. 1981. Combined modality therapy of operated astrocytomas grade III and IV. Confirmation of the value of postoperative irradiation and lack of potentiation of bleomycin on survival time: a prospective multicenter trial of the Scandinavian Glioblastoma Study Group, *Cancer*, 47(4), 649–652.

Kuesel, AC, GR Sutherland, W Halliday, and I Smith. 1994. 1H MRS of high grade astrocytomas: mobile lipid accumulation in necrotic tissue, *NMR in Biomedicine*, 7(3), 149–155.

Kwock, L, JK Smith, M Castillo, MG Ewend, F Collichio, DE Morris, TW Bouldin, and S Cush. 2006. Clinical role of proton magnetic resonance spectroscopy in oncology: brain, breast, and prostate cancer, *The Lancet Oncology*, 7, 859–868.

Kybic, J and M Unser. 2003. Fast parametric elastic image registration, *IEEE Transactions on Image Processing*, 12(11), 1427–1442.

Lai, PH, JT Ho, WL Chen, SS Hsu, JS Wang, HB Pan, and F Yang Chien. 2002. Brain abscess and necrotic brain tumor: discrimination with proton MR spectroscopy and diffusion-weighted imaging, *American Journal of Neuroradiology*, 23(8), 1369–1377.

Laprie, A, I Catalaa, E Cassol, TR McKnight, D Berchery, D Marre, JM Bachaud, I Berry, and EC Moyal. 2008. Proton magnetic resonance spectroscopic imaging in newly diagnosed glioblastoma: predictive value for the site of postradiotherapy relapse in a prospective longitudinal study, *International Journal of Radiation Oncology Biology Physics*, 70, 773–781.

Laruelo, A, L Chaari, H Batatia, S Ken, B Rowland, A Laprie, and JY Tourneret. 2013a. Hybrid sparse regularization for Magnetic Resonance Spectroscopy, in *Proceedings of the Annual International Conference of the IEEE Engineering in Medicine and Biology Society (EMBC'13)*, Osaka, Japan, 6768–71.

Laruelo, A, L Chaari, S Ken, JY Tourneret, H Batatia, and A Laprie. 2016a. MRSI data unmixing using spatial and spectral priors in transformed domains, in *Proceedings of the IEEE International Symposium on Biomedical Imaging (ISBI)*, Prague, Czech Republic.

Laruelo, A, L Chaari, B Rowland, S Ken, H Batatia, R Ferrand, JY Tourneret, and A Laprie. 2013b. MRSI data denoising to improve metabolite quantification, in *Proceedings of the 30th Annual Scientific Meeting of the European Society for Magnetic Resonance in Medicine and Biology (ESMRMB)*, Toulouse, France, 470–471.

Laruelo, A, L Chaari, JY Tourneret, H Batatia, S Ken, B Rowland, R Ferrand, and A Laprie. 2016b. Spatio-spectral regularization to improve MRSI quantification, *NMR in Biomedicine*. In Press.

Laudadio, T, N Mastronardi, L Vanhamme, P Van Hecke, and S Van Huffel. 2002. Improved Lanczos algorithms for blackbox MRS data quantitation, *Journal of Magnetic Resonance*, 157(2), 292–297.

Lauterbur, PC et al. 1973. Image formation by induced local interactions: examples employing nuclear magnetic resonance, *Nature*, 242(5394), 190–191.

Lee, DD and HS Seung. 1999. Learning the parts of objects by non-negative matrix factorization, *Nature*, 401, 788–791.

Lee, MC and SJ Nelson. 2008. Supervised pattern recognition for the prediction of contrast-enhancement appearance in brain tumors from multivari-

ate magnetic resonance imaging and spectroscopy, *Artificial Intelligence in Medicine*, 43(1), 61–74.

Lee, MH, CD Smyser, and JS Shimony. 2013. Resting-state fMRI: a review of methods and clinical applications, *American Journal of Neuroradiology*, 34(10), 1866–1872.

Li, Y, DM Sima, SV Cauter, AR Croitor Sava, U Himmelreich, Y Pi, and S Van Huffel. 2013. Hierarchical non-negative matrix factorization (hNMF): a tissue pattern differentiation method for glioblastoma multiforme diagnosis using MRSI, *NMR in Biomedicine*, 26(3), 307–319.

Liang, ZP, R Bammer, J Ji, NJ Pelc, and GH Glover. 2002. Making better SENSE: wavelet denoising, Tikhonov regularization, and total least squares., in *Proceedings of the International Society for Magnetic Resonance in Medicine*, Hawaï, USA: IEEE, 2388.

Lin, CJ and RC Weng. 2004. Simple probabilistic predictions for support vector regression, Tech. rep., Department of Computer Science, National Taiwan University. http://www.csie.ntu.edu.tw/∼cjlin/papers/svrprob.pdf.

Lin, FH, KK Kwong, JW Belliveau, and LL Wald. 2004. Parallel Imaging Reconstruction Using Automatic Regularization, *Magnetic Resonance in Medicine*, 51, 559–567.

Liu, B, E Abdelsalam, J Sheng, and L Ying. 2008. Improved spiral SENSE reconstruction using a multiscale wavelet model, in *Proceedings of the IEEE International Symposium on Biomedical Imaging (ISBI)*, IEEE, 1505–1508.

Liu, B, K King, M Steckner, J Xie, J Sheng, and L Ying. 2009. Regularized sensitivity encoding (SENSE) reconstruction using Bregman iterations, *Magnetic Resonance in Medicine*, 61(1), 145–152.

Liu, B, L Ying, M Steckner, J Xie, and J Sheng. 2007. Regularized SENSE reconstruction using iteratively refined total variation method, in *Proceedings of the IEEE International Symposium on Biomedical Imaging (ISBI)*, IEEE, 121–124.

Logothetis, NK, J Pauls, M Augath, T Trinath, and A Oeltermann. 2001. Neurophysiological investigation of the basis of the fMRI signal, *Nature*, 412(6843), 150–157.

Lukas, L, A Devos, JAK Suykens, L Vanhamme, FA Howe, C Majós, A Moreno-Torres, M Van der Graaf, AR Tate, C Arús, et al. 2004. Brain tumor classification based on long echo proton MRS signals, *Artificial Intelligence in Medicine*, 31(1), 73–89.

Lustig, M, D Donoho, and JM Pauly. 2007. Sparse MRI: The application of compressed sensing for rapid MR imaging, *Magnetic Resonance in Medicine*, 58(6), 1182–1195.

Luts, J, A Heerschap, JAK Suykens, and S Van Huffel. 2007. A combined MRI and MRSI based multiclass system for brain tumour recognition using LS-SVMs with class probabilities and feature selection, *Artificial Intelligence in Medicine*, 40(2), 87–102.

Luts, J, T Laudadio, AJ Idema, AW Simonetti, A Heerschap, D Vandermeulen, JAK Suykens, and S Van Huffel. 2009. Nosologic imaging of the brain: segmentation and classification using MRI and MRSI, *NMR in Biomedicine*, 22(4), 374–390.

Ma, D, V Gulani, N Seiberlich, K Liu, JL Sunshine, JL Duerk, and MA Griswold. 2013. Magnetic resonance fingerprinting, *Nature*, 495(7440), 187–192.

Maeda, M, S Itoh, H Kimura, T Iwasaki, N Hayashi, K Yamamoto, Y Ishii, and T Kubota. 1993. Tumor vascularity in the brain: evaluation with dynamic susceptibility-contrast MR imaging, *Radiology*, 189(1), 233–238.

Mahmoodabadi, SZ, J Alireazie, P Babyn, A Kassner, and E Widjaja. 2008. MRS feature extraction: time-frequency and wavelet analysis, in *Proceedings of the 2nd International Conference on Bioinformatics and Biomedical Engineering (ICBBE)*, Shanghai, China: IEEE, 1863–1866.

Martens, K, T Meyners, D Rades, V Tronnier, MM Bonsanto, D Petersen, J Dunst, and K Dellas. 2013. The prognostic value of tumor necrosis in patients undergoing stereotactic radiosurgery of brain metastases, *Radiation Oncology*, 8(1), 162.

McDonald, MW, HK Shu, WJ Curran, and IR Crocker. 2011. Pattern of failure after limited margin radiotherapy and temozolomide for glioblastoma, *International Journal of Radiation Oncology Biology Physics*, 79(1), 130–136.

McKnight, TR, SM Noworolski, DB Vigneron, and SJ Nelson. 2001. An automated technique for the quantitative assessment of 3D-MRSI data from patients with glioma, *Journal of Magnetic Resonance Imaging*, 13(2), 167–177.

McKnight, TR, MH von dem Bussche, DB Vigneron, Y Lu, MS Berger, MW McDermott, WP Dillon, EE Graves, A Pirzkall, and SJ Nelson. 2002. Histopathological validation of a three-dimensional magnetic resonance spectroscopy index as a predictor of tumor presence, *Journal of neurosurgery*, 97(4), 794–802.

McLachlan, G. 2004. *Discriminant analysis and statistical pattern recognition*, John Wiley & Sons.

Menze, BH, MP Lichy, P Bachert, BM Kelm, HP Schlemmer, and FA Hamprecht. 2006. Optimal classification of long echo time in vivo magnetic resonance spectra in the detection of recurrent brain tumors, *NMR in Biomedicine*, 19(5), 599–609.

Mierisová, S, A van den Boogaart, I Tkác, P Van Hecke, L Vanhamme, and T Liptaj. 1998. New approach for quantitation of short echo time in vivo $^{1}$H MR spectra of brain using AMARES, *NMR in Biomedicine*, 1, 32–39.

Minniti, G, D Amelio, M Amichetti, M Salvati, R Muni, A Bozzao, G Lanzetta, S Scarpino, A Arcella, and RM Enrici. 2010. Patterns of failure and comparison of different target volume delineations in patients with glioblastoma treated with conformal radiotherapy plus concomitant and adjuvant temozolomide, *Radiotherapy and Oncology*, 97(3), 377–381.

Monjazeb, AM, Ayala De, C Jensen, LD Case, JD Bourland, TL Ellis, KP McMullen, MD Chan, SB Tatter, GJ Lesser, et al. 2012. A phase I dose escalation study of hypofractionated IMRT field-in-field boost for newly diagnosed glioblastoma multiforme, *International Journal of Radiation Oncology Biology Physics*, 82(2), 743–748.

Moonen, CT, M Von Kienlin, P Van Zijl, J Cohen, J Gillen, P Daly, and G Wolf. 1989. Comparison of single-shot localization methods (steam and press) for In vivo proton NMR spectroscopy, *NMR in Biomedicine*, 2(5-6), 201–208.

Moreau, JJ. 1962. Fonctions convexes duales et points proximaux dans un espace hilbertien, *Comptes Rendus de l'Académie des Sciences*, 255, 2897–2899.

Moreau, JJ. 1965. Proximité et dualité dans un espace hilbertien, *Bulletin de la Société Mathématique de France*, 93, 273–299.

Mosconi, E, DM Sima, MI Osorio Garcia, M Fontanella, S Fiorini, S Van Huffel, and P Marzola. 2014a. Different quantification algorithms may lead to different results: a comparison using proton MRS lipid signals, *NMR in Biomedicine*, 27(4), 431–443.

Mosconi, E, DM Sima, MI Osorio Garcia, M Fontanella, S Fiorini, S Van Huffel, and Marzola P. 2014b. Different quantification algorithms may lead to different results: a comparison using proton MRS lipids signals, *NMR in Biomedicine*, 27(4), 431–443.

Moudden, Y, J Bobin, JL Starck, and J Fadili. 2009. Blind source separation with spatio-spectral sparsity constraints - Application to hyperspectral data analysis, in *Independent Component Analysis and Signal Separation*, Springer, 523–531.

Murphy, PS, IJ Rowland, L Viviers, M Brada, MO Leach, and ASK Dzik-Jurasz. 2003. Could assessment of glioma methylene lipid resonance by in vivo 1H-MRS be of clinical value?, *The British Journal of Radiology*.

Nakajima, T, T Kumabe, M Kanamori, R Saito, M Tashiro, M Watanabe, and T Tominaga. 2009. Differential diagnosis between radiation necrosis and glioma progression using sequential proton magnetic resonance spectroscopy and methionine positron emission tomography, *Neurologia medico-chirurgica*, 49(9), 394–401.

Nascimento, JMP and JM Bioucas Dias. 2005. Vertex component analysis: a fast algorithm to unmix hyperspectral data, *IEEE Transactions on Geoscience and Remote Sensing*, 43(4), 898–910.

Negendank, WG, R Sauter, TR Brown, JL Evelhoch, A Falini, ED Gotsis, A Heerschap, K Kamada, B Lee, MM Mengeot, et al. 1996. Proton magnetic resonance spectroscopy in patients with glial tumors: a multicenter study, *Journal of neurosurgery*, 84(3), 449–458.

Nelson, SJ. 2001. Analysis of volume MRI and MR spectroscopic imaging data for the evaluation of patients with brain tumors, *Magnetic Resonance in Medicine*, 46(2), 228–239.

Nelson, SJ, E Graves, A Pirzkall, X Li, CA Antiniw, DB Vigneron, and TR McKnight. 2002. In vivo molecular imaging for planning radiation therapy of gliomas: an application of 1H MRSI, *Journal of Magnetic Resonance Imaging*, 16(4), 464–476.

Nguyen, HM, JP Haldar, MN Do, and Liang Zhi-Pei. 2010. Denoising of MR spectroscopic imaging data with spatial-spectral regularization, in *Proceedings of the IEEE International Symposium on Biomedical Imaging (ISBI)*, Rotterdam, Netherlands, 720–723.

Nguyen, MH and F De la Torre. 2010. Optimal feature selection for support vector machines, *Pattern recognition*, 43(3), 584–591.

Ogawa, S, TM Lee, AR Kay, and DW Tank. 1990. Brain magnetic resonance imaging with contrast dependent on blood oxygenation, *Proceedings of the National Academy of Sciences of the United States of America*, 87(24), 9868–9872.

Ogg, RJ, PB Kingsley, and JS Taylor. 1994. WET, a T1-and B1-insensitive water-suppression method for in vivo localized 1H NMR spectroscopy, *Journal of Magnetic Resonance, Series B*, 104(1), 1–10.

Organization, World Health. 1979. WHO Handbook for Reporting Results of Cancer Treatment.

Ortega-Martorell, S, PJG Lisboa, A Vellido, RV Simões, M Pumarola, M Julià-Sapé, and C Arús. 2012. Convex Non-Negative Matrix Factorization for Brain Tumor Delimitation from MRSI Data, *PLoS ONE*, 7(10).

Oya, N, J Aoki, T Shinozaki, H Watanabe, K Takagishi, and K Endo. 1999. Preliminary study of proton magnetic resonance spectroscopy in bone and soft tissue tumors: an unassigned signal at 2.0-2.1 ppm may be a possible

indicator of malignant neuroectodermal tumor, *Radiation Medicine*, 18(3), 193–198.

Padhani, AR. 2011. Diffusion magnetic resonance imaging in cancer patient management, *Seminars in Radiation Oncology*, 21(2), 119–140.

Patel, SG, TR McKnight, SJ Nelson, and WP Dillon. 1999. Metabolic characteristics within the T2 abnormality associated with primary brain tumors as determined by 3-D proton MR spectroscopic imaging, *Radiology*, 213, 187–188.

Payne, GS and MO Leach. 2014. Applications of magnetic resonance spectroscopy in radiotherapy treatment planning, *The British Journal of Radiology*.

Pirzkall, A, X Li, J Oh, S Chang, MS Berger, DA Larson, LJ Verhey, WP Dillon, and SJ Nelson. 2004. 3D MRSI for resected high-grade gliomas before RT: tumor extent according to metabolic activity in relation to MRI, *International Journal of Radiation Oncology Biology Physics*, 59(1), 126–137.

Pirzkall, A, TR McKnight, EE Graves, MP Carol, PK Sneed, WW Wara, SJ Nelson, LJ Verhey, and DA Larson. 2001. MR-spectroscopy guided target delineation for high-grade gliomas, *International Journal of Radiation Oncology Biology Physics*, 50(4), 915–928.

Pizurica, A, AM Wink, E Vansteenkiste, W Philips, and J Roerdink. 2006. A review of wavelet denoising in MRI and ultrasound brain imaging, *Current Medical Imaging Reviews*, 2(2), 247–260.

Platt, JC. 2000. Probabilistic outputs for support vector machines and comparison to regularized likelihood methods, *Advances in Large Margin Classifiers*.

Pluim, JPW, JBA Maintz, M Viergever, et al. 2003. Mutual-information-based registration of medical images: a survey, *IEEE Transactions on Medical Imaging*, 22(8), 986–1004.

Posse, S, R Otazo, SR Dager, and J Alger. 2013. MR Spectroscopic Imaging: Principles and Recent Advances, *Journal of Magnetic Resonance Imaging*, 37, 1301–1325.

Poullet, JB, DM Sima, AW Simonetti, B De Neuter, L Vanhamme, P Lemmerling, and S Van Huffel. 2006. An automated quantitation of short echo time MRS spectra in a open source software environment: AQSES, *NMR in Biomedicine*, 20, 493–504.

Provencher, S. 2001. Automatic quantitation of localized in vivo $^{1}$H spectra with LCModel, *NMR in Biomedicine*, 14, 260–264.

Purcell, EM, HC Torrey, and RV Pound. 1946. Resonance absorption by nuclear magnetic moments in a solid, *Physical review*, 69(1-2), 37.

Pustelnik, N, C Chaux, and JC Pesquet. 2011. Parallel proximal algorithm for image restoration using hybrid regularization, *IEEE Transactions on Image Processing*, 20(9), 2450–2462.

Raguet, H, J Fadili, and G Peyré. 2013. A Generalized Forward-Backward Splitting, *SIAM Journal on Imaging Sciences*, 6(3), 1199–1226.

Raschke, F, TL Jones, TR Barrick, and FA Howe. 2014. Delineation of gliomas using radial metabolite indexing, *NMR in Biomedicine*, 27(9), 1053–1062.

Ratiney, H, M Sdika, Y Coenradie, S Cavassila, D van Ordmont, and D Graveron-Demilly. 2005. Time domain semi-parametric estimation based on a metabolite basis set, *NMR in Biomedicine*, 18, 1–13.

Reiser, B. 2000. Measuring the effectiveness of diagnostic markers in the presence of measurement error through the use of ROC curves, *Statistics in medicine*, 19(16), 2115–2129.

Ricci, PE, A Pitt, PJ Keller, SW Coons, and JE Heiserman. 2000. Effect of voxel position on single-voxel MR spectroscopy findings, *American Journal of Neuroradiology*, 21(2), 367–374.

Riccia, R, A Baccia, V Tugnolib, S Battagliaa, M Maffeia, R Agatia, and M Leonardia. 2007. Metabolic Findings on 3T 1H-MR Spectroscopy in Peritumoral Brain Edema, *American Journal of Neuroradiology*, 28, 1287–1291.

Ridgway, JP. 2010. Cardiovascular magnetic resonance physics for clinicians: part I, *Journal of Cardiovascular Magnetic Resonance*, 12(1), 71.

Rowland, B, A Laruelo, S Ken, R Ferrand, and A Laprie. 2013. Water suppression in post-processing of MRSI signals, in *Innovative imaging to improve radiotherapy treatments*, Lulu Enterprises Inc Ed, 63–70.

Safriel, Y, MA Pol-Rodriguez, EJ Novotny, DL Rothman, and RK Fulbright. 2005. Reference Values for Long Echo Time MR Spectroscopy in Healthy Adults, *American Journal of Neuroradiology*, 26, 1439–1445.

Sajda, P, S Du, TR Brown, R Stoyanova, DC Shungu, X Mao, and LC Parra. 2004. Nonnegative matrix factorization for rapid recovery of constituent spectra in magnetic resonance chemical shift imaging of the brain, *IEEE Transactions on Medical Imaging*, 23, 1453–1465.

Samadzadegan, F, H Hasani, and T Partovi. 2010. Sensitivity analysis of support vector machine in classification of hyperspectral imagery, in *Proceedings of the Canadian Geomatics Conference*, Calgary, Canada.

Sava, AC, DM Sima, JB Poullet, AJ Wright, A Heerschap, and S Van Huffel. 2011. Exploiting spatial information to estimate metabolite levels in 2D MRSI of heterogeneous brain lesions, *NMR in Biomedicine*, 24, 824–835.

Schober, O and B Riemann. 2013. *Molecular Imaging in Oncology*, Springer.

Serrai, H, L Nadal-Desbarats, H Poptani, JD Glickson, and L Senhadji. 2000. Lactate editing and lipid suppression by continuous wavelet transform analysis: Application to simulated and 1H MRS brain tumor time-domain data, *Magnetic Resonance in Medicine*, 43(5), 649–656.

Serrai, H, L Senhadji, D Jacques, and JL Coatrieux. 1997. Time-Domain Quantification of Amplitude, Chemical Shift, Apparent Relaxation Time $T^*2$, and Phase by Wavelet-Transform Analysis. Application to Biomedical Magnetic Resonance Spectroscopy, *Journal of Magnetic Resonance*, 124(1), 20–34.

Setzer, S, G Steidl, and T Teuber. 2010. Deblurring Poissonian images by split Bregman techniques, *Journal of Visual Communication and Image Representation*, 21(3), 193–199.

Shankar, RV, S Agarwal, S Geethanath, and VD Kodibagkar. 2015. Rapid MR spectroscopic imaging of lactate using compressed sensing, in *SPIE*

*Medical Imaging*, International Society for Optics and Photonics, 94171J–94171J.

Siemens, AG. 2005. Magnetic Resonance: Operator Manual version syngo MR 2006T.

Simonetti, AW, M Melssen, WJ Van Der Graaf, A Heerschap, and LMC Buydens. 2003. A new chemometric approach for brain tumor classification using magnetic resonance imaging and spectroscopy, *Analytical Chemistry*, 75(20), 5352–5361.

Simonetti, AW, WJ Melssen, F Szabo de Edelenyi, JJ van Asten, A Heerschap, and L Buydens. 2005. Combination of feature-reduced MR spectroscopic and MR imaging data for improved brain tumor classification, *NMR in Biomedicine*, 18(1), 34–43.

Skoch, A, F Jiru, and J Bunke. 2008. Spectroscopic imaging: basic principles, *European Journal of Radiology*, 67(2), 230–239.

Smith, SA, TO Levante, BH Meier, and RR Ernst. 1994. Computer Simulations in Magnetic Resonance. An Object-Oriented Programming Approach, *Journal of Magnetic Resonance*, 106, 75–105.

Soher, BJ, K Young, V Govindaraju, and AA Maudsley. 1998. Automated spectral analysis III: application to in vivo proton MR spectroscopy imaging, *Magnetic Resonance in Medicine*, 40, 822–831.

Stadlbauer, A, C Nimsky, R Buslei, K Pinker, S Gruber, T Hammen, M Buchfelder, and O Ganslandt. 2007. Proton magnetic resonance spectroscopic imaging in the border zone of gliomas: correlation of metabolic and histological changes at low tumor infiltration—initial results, *Investigative radiology*, 42(4), 218–223.

Starck, JL, F Murtagh, and JM Fadili. 2010. *Sparse image and signal processing: wavelets, curvelets, morphological diversity*, Cambridge university press.

Statnikov, A, CF Aliferis, and DP Hardin. 2011. *A Gentle Introduction to Support Vector Machines in Biomedicine: Theory and Methods*, World Scientific.

Stefan, D, F Di Cesare, A Andrasescu, E Popa, A Lazariev, E Vescovo, O Strbak, S Williams, Z Starcuk, M Cabanas, D van Ormondt, and D Graveron-Demilly. 2009. Quantitation of magnetic resonance spectroscopy signals: the jMRUI software package, *Measurement Science and Technology*, 20, 104035–104044. DOI:10.1088/0957-0233/20/10/104035.

Stupp, R, WP Mason, MJ Van Den Bent, M Weller, B Fisher, MJ Taphoorn, K Belanger, AA Brandes, C Marosi, U Bogdahn, et al. 2005. Radiotherapy plus concomitant and adjuvant temozolomide for glioblastoma, *New England Journal of Medicine*, 352(10), 987–996.

Suykens, JAK and J Vandewalle. 1999. Least squares support vector machine classifiers, *Neural processing letters*, 9(3), 293–300.

Swets, JA. 1988. Measuring the accuracy of diagnostic systems, *Science*, 240(4857), 1285–1293.

Swinscow, TDV and MJ Campbell. 2002. *Statistics at square one*, Bmj London.

Therasse, P, SG Arbuck, EA Eisenhauer, J Wanders, RS Kaplan, L Rubinstein, J Verweij, M Van Glabbeke, AT van Oosterom, MC Christian, et al. 2000. New guidelines to evaluate the response to treatment in solid tumors, *Journal of the National Cancer Institute*, 92(3), 205–216.

Thevenaz, P, UE Ruttimann, and M Unser. 1998. A pyramid approach to subpixel registration based on intensity, *IEEE Transactions on Image Processing*, 7(1), 27–41.

Tien, RD, GJ Felsberg, H Friedman, M Brown, and J MacFall. 1994. MR imaging of high-grade cerebral gliomas: value of diffusion-weighted echoplanar pulse sequences, *American Journal of Roentgenology*, 162(3), 671–677.

Tikhonov, A. 1963. Tikhonov regularization of incorrectly posed problems, *Soviet Mathematics Doklady*, 4, 1624–1627.

Tkáć, I and R Gruetter. 2005. Methodology of H NMR spectroscopy of the human brain at very high magnetic fields, *Applied magnetic resonance*, 29(1), 139–157.

Tofts, PS, G Brix, DL Buckley, JL Evelhoch, E Henderson, MV Knopp, HB Larsson, TY Lee, NA Mayr, and GJ et al. Parker. 1999. Estimating kinetic parameters from dynamic contrast-enhanced T(1)-weighted MRI of a diffusable tracer: standardized quantities and symbols, *Journal of Magnetic Resonance Imaging*, 10, 223–232.

Tzika, AA. 2008. Proton magnetic resonance spectroscopic imaging as a cancer biomarker for pediatric brain tumors (Review), *International Journal of Oncology*, 32(3), 517–526.

Van den Boogaart, A, D Van Ormondt, WWF Pijnappel, R De Beer, and M Ala-Korpela. 1994. Removal of the water resonance from 1H magnetic resonance spectra, *Mathematics in signal processing*, 3, 175–195.

Van der Graaf, M. 2010. In vivo magnetic resonance spectroscopy: basic methodology and clinical applications, *European Biophysics Journal*, 39(4), 527–540.

Vanhamme, L, T Sundin, P Van Hecke, and S Van Huffel. 2001. MR spectroscopy quantitation: a review of time-domain methods., *NMR in Biomedicine*, 14, 233–246. DOI: 10.1002/nmb.695.

Vanhamme, L, A Van Den Boogaart, and S Van Huffel. 1997. Improved method for accurate and efficient quantification of MRS data with use of prior knowledge, *Journal of Magnetic Resonance*, 129, 35–43.

Velikina, J, AL Alexander, and AA Samsonov. 2010. A novel approach for T1 relaxometry using constrained reconstruction in parametric dimension, in *Proceedings of the International Society for Magnetic Resonance in Medicine (ISMRM)*, vol. 18, 350.

Vincent, T, L Risser, and P Ciuciu. 2010. Spatially adaptive mixture modeling for analysis of fMRI time series, *IEEE Transactions on Medical Imaging*, 29(4), 1059–1074.

Viola, P and WM Wells. 1997. Alignment by maximization of mutual information, *International Journal of Computer Vision*, 24(2), 137–154.

Vranova, J, J Horak, K Kratka, M Hendrichova, and K Kovarikova. 2009. ROC analysis and the use of cost-benefit analysis for determination of the optimal cut point., *Journal of Czech Physicians*, 148, 410–415.

Wahl, RL, H Jacene, Y Kasamon, and MA Lodge. 2009. From RECIST to PERCIST: evolving considerations for PET response criteria in solid tumors, *Journal of Nuclear Medicine*, 50(Suppl 1), 122S–150S.

Walker, MD, JE Alexander, WE Hunt, CS MacCarty, JMS Mahaley, JJ Mealey, HA Norrell, G Owens, J Ransohoff, CB Wilson, et al. 1978. Evaluation of BCNU and/or radiotherapy in the treatment of anaplastic gliomas: a cooperative clinical trial, *Journal of neurosurgery*, 49(3), 333–343.

Wang, T, S Kang, Q Chu, Y Ren, Y Mu, L Qu, J He, C Jin, and B Xia. 2009. Automics: an integrated platform for NMR-based metabolomics spectra processing and data analysis., *BMC Bioinformatics*, 10. DOI: 10.1186/1471-2105-10-83.

Wang, Z, A Bovik, HR Sheikh, and EP Simoncelli. 2004. Image quality assessment: From error visibility to structural similarity, *IEEE Transactions on Image Processing*, 13, 600–612.

Worthington, LA. 2015. *Investigation of compressed-sensing for acceleration of magnetic resonance spectroscopic imaging*, Ph.D. thesis, University of Birmingham.

Wu, TF, CJ Lin, and RC Weng. 2004. Probability estimates for multi-class classificationby pairwise coupling, *Journal of Machine Learning Research*, 5, 975–1005.

Xi, Y and D Rocke. 2008. Baseline correction for NMR spectroscopic metabolomics data analysis., *BMC Bioinformatics*, 9(1), 324.

Ying, L, D Xu, and ZP Liang. 2004a. On Tikhonov regularization for image reconstruction in parallel MRI, in *Proceedings of the Annual International Conference of the IEEE Engineering in Medicine and Biology Society (EMBC'04)*, IEEE, 1056–1059.

Ying, L, D Xu, and ZP Liang. 2004b. On Tikhonov regularization for image reconstruction in parallel MRI, in *Proceedings of the Annual International Conference of the IEEE Engineering in Medicine and Biology Society (EMBC'04)*, San Francisco, USA, 1056–1059.

Youden, WJ. 1950. Index for rating diagnostic tests, *Cancer*, 3(1), 32–35.

Zarei, S, J Alireazie, P Babyn, A Kassner, and E Widjaja. 2008. MRS feature extraction: time-frequency and wavelet analysis, in *Proceedings of the 2nd International Conference on Bioinformatics and Biomedical Engineering (ICBBE)*, Shanghai, China, 1863–1866.

Zhou, Q, W Chen, S Song, JR Gardner, KQ Weinberger, and Y Chen. 2015. A reduction of the elastic net to support vector machines with an application to GPU computing.

Zhu, J and T Hastie. 2012. Kernel logistic regression and the import vector machine, *Journal of Computational and Graphical Statistics*.

**TITRE et résumé en anglais:**

**Title:**
Integration of magnetic resonance spectroscopic imaging into the radiotherapy treatment planning

**Summary:**
The aim of this thesis is to propose new algorithms to overcome the current limitations and to address the open challenges in the processing of magnetic resonance spectroscopic imaging (MRSI) data. MRSI is a non-invasive modality able to provide the spatial distribution of relevant biochemical compounds (metabolites) commonly used as biomarkers of disease. Information provided by MRSI can be used as a valuable insight for the diagnosis, treatment and follow-up of several diseases such as cancer or neurological disorders. Obtaining accurate and reliable information from in vivo MRSI signals is a crucial requirement for the clinical utility of this technique. Despite the numerous publications on the topic, the interpretation of MRSI data is still a challenging problem due to different factors such as the low signal-to-noise ratio (SNR) of the signals, the overlap of spectral lines or the presence of nuisance components. This thesis addresses the problem of interpreting MRSI data and characterizing recurrence in tumor brain patients. These objectives are addressed through a methodological approach based on novel processing methods that incorporate prior knowledge on the MRSI data using a spatio-spectral regularization.
As an application, the thesis addresses the integration of MRSI into the radiotherapy treatment workflow within the context of the European project SUMMER (Software for the Use of Multi-Modality images in External Radiotherapy) founded by the European Commission (FP7–PEOPLE–ITN framework).

**AUTEUR** : Andrea LARUELO FERNANDEZ

**TITRE** : Intégration des cartes métaboliques d'imagerie spectroscopique à la planification de radiothérapie.

**DIRECTEUR(S) DE THESE** : Dr. Anne LAPRIE et Dr. Lotfi CHAARI.

**LIEU ET DATE DE SOUTENANCE** : TOULOUSE, 24 mai 2016.

---


**RESUME en français**

L'objectif de cette thèse est de proposer de nouveaux algorithmes pour surmonter les limitations actuelles et de relever les défis ouverts dans le traitement de l'imagerie spectroscopique par résonance magnétique (ISRM). L'ISRM est une modalité non invasive capable de fournir la distribution spatiale des composés biochimiques (métabolites) utilisés comme biomarqueurs de la maladie. Les informations fournies par l'ISRM peuvent être utilisées pour le diagnostic, le traitement et le suivi de plusieurs maladies telles que le cancer ou des troubles neurologiques. Cette modalité se montre utile en routine clinique notamment lorsqu'il est possible d'en extraire des informations précises et fiables. Malgré les nombreuses publications sur le sujet, l'interprétation des données d'ISRM est toujours un problème difficile en raison de différents facteurs tels que le faible rapport signal sur bruit des signaux, le chevauchement des raies spectrales ou la présence de signaux de nuisance. Cette thèse aborde le problème de l'interprétation des données d'ISRM et la caractérisation de la rechute des patients souffrant de tumeurs cérébrales. Ces objectifs sont abordés à travers une approche méthodologique intégrant des connaissances a priori sur les données d'ISRM avec une régularisation spatio-spectrale.
Concernant le cadre applicatif, cette thèse contribue à l'intégration de l'ISRM dans le workflow de traitement en radiothérapie dans le cadre du projet européen SUMMER (Software for the Use of Multi-Modality images in External Radiotherapy) financé par la Commission européenne (FP7-PEOPLE-ITN).


---


**MOTS-CLES**

MR Spectroscopic Imaging (MRSI), Quantification, Blind source separation (BSS), Pattern Recognition Denoising, Regularization, Multi-parametric data, Tumor relapse prediction.


---

**DISCIPLINE ADMINISTRATIVE (identique à celle de la page de titre)**

Radio-physique et Imagerie Médicale

---


**INTITULE ET ADRESSE DE L'U.F.R. OU DU LABORATOIRE :**

Laboratoire Imagerie Cérébrale et Handicaps Neurologiques (ICHN), INSERM UMRS 825
Institut de Recherche en Informatique de Toulouse (IRIT) - ENSEEIHT (UMR 5505)